

# SIDE HEATED NATURAL CONVECTION IN COARSE-GRAINED POROUS MEDIA

AN EXPERIMENTAL STUDY

by

**Nima Rounaghi**

in partial fulfillment of the requirements for the degree of

**Master of Science**  
in Applied Physics

at the Delft University of Technology,  
to be defended publicly on Monday the 3<sup>rd</sup> of December 2018 at 09:30 AM.

Supervisors: I. Ataei-Dadavi, MSc.  
Dr. Dipl.- Ing. S. Kenjeres  
Prof. Dr. Ir. C.R. Kleijn

Thesis committee: Dr. Dipl.- Ing. S. Kenjeres, TU Delft  
Prof. Dr. Ir. C. R. Kleijn, TU Delft  
Dr. Ir. M.J. Tummers, TU Delft  
I. Ataei-Dadavi, MSc. TU Delft

*This thesis is confidential and cannot be made public until 03/12/2018*

An electronic version of this thesis is available at <http://repository.tudelft.nl/>.



# ABSTRACT

This MSc thesis reports on an experimental study performed to test the effects of packed beds of relatively large spheres on natural convection inside a cubical enclosure which is heated from the left side and cooled from the right side. With 'relatively large', a ratio of  $L/D=5$  is meant where  $L$  is the length between the hot and cold plate and  $D$  is the diameter of each sphere where the packed bed consists of. To gain a better understanding and enhanced knowledge of the effects of coarse-grained porous media on side-heated natural convection, heat transfer experiments were performed as well as flow and temperature distribution measurements using the optical measurement techniques Particle Imaging Velocimetry (PIV) and Liquid Crystal Thermography (LCT). In the optical measurement experiments, hydrogel balls were used which have the same refractive index as that of water.

In the heat transfer experiments, Nusselt numbers were measured over a wide range of Rayleigh numbers ( $1.6 \times 10^7 < Ra < 1.9 \times 10^9$ ). In the pure-fluid enclosure the heat transfer data points were fitted to the power-law:  $Nu = 0.250 \times Ra^{0.264}$ . The effects of spheres with different materials, different sizes and different packing types were tested. It was found that, in general, at lower Ra-numbers, the heat transfer was reduced significantly more than at high Ra-numbers where the asymptotic pure-fluid cavity result was nearly reached for all tested configurations. Also, a 3D printed structure was tested to study the effect of a distance between the porous medium and the hot and cold walls.

The optical flow experiments were performed at  $Ra = 7.9 \times 10^6$  and  $Ra = 1.5 \times 10^8$  using PIV. It was found that the flow in the side-heated configuration is boundary-driven and that in the pure-fluid enclosure the highest velocities are observed near the heated and cooled walls and are distributed uniformly over the height of the cell. At the higher Ra-number, it was found that the high-velocity layer near the boundary became thinner compared to the low Ra-number. Therefore, the flow can easily pass through the void space near the periphery of the cell and heat transfer gets closer to that of the pure-fluid cavity. It was observed that the presence of the coarse-grained porous media significantly affected the natural convection flow. This effect was observed by the distribution of high velocity spots near the outer-lying spheres near the periphery of the enclosure. In the void space between the spheres, very low to no velocities were observed. Not only high velocity spots were observed near the hot and cold walls, but also near the bottom and top walls. In the presence of the coarse-grained porous media, vertical velocities of 1.75 times larger near the left and right walls and horizontal velocities of nearly 3.5-4 times higher near the top and bottom walls, were observed.

The optical measurement technique used to qualitatively and quantitatively measure the temperature distribution was LCT. The LCT measurements were performed at  $Ra = 8.2 \times 10^7$  and hydrogel balls were used to represent the coarse-grained porous media. It was found that in the pure-fluid enclosure, the temperature is divided into a warmer part at the top of the enclosure while at the bottom of the enclosure the colder fluid was present. The thermal boundary layers were observed near both the hot and cold vertical walls and it was noticed that the warmer fluid was mainly present in the upper half of the cell while the colder fluid was mainly in the lower half of the cell. From this observation it was concluded that in the pure-water enclosure, the temperature gradient is present in the vertical direction. In the hydrogel filled cell however, it was observed that the colder fluid dominated the warmer fluid and that the transition between the different temperatures fluid was much smoother. In the hydrogel spheres filled enclosure a more tilted temperature gradient was observed in the diagonal direction. The main conclusion is that the natural convective flow is indeed affected in the presence of the coarse-grained porous media with respect to the pure-fluid cavity.



# PREFACE

This thesis has been written by me as the final part of the Masters' program in Applied Physics at the Delft University of Technology. For the past 10 months I have been working on this experimental study along with some great people and therefore I would like to thank a few persons for their scientific, practical but also moral help.

First of all I would like to express my sincere gratitude to my daily supervisor MSc. *Iman Ataei-Dadavi* with whom I was dealing with almost every day during the experimental work. Thank you for sharing your extensive knowledge patiently and for constantly monitoring my progression. Also I appreciate the fact that you are a very calm and patient person who was always in for a friendly chatter and a very nice person to work with. I wish you all the best in the rest of your professional career.

Also I would like to sincerely thank Prof. Dr. Ir. *C.R. Kleijn*, Dr. Dipl-Eng. *S. Kenjeres* and Dr. Ir. *M.J. Tummers* for the meaningful and instructive biweekly progress meetings. Thank you very much for sharing your years of experience worth of knowledge with me which helped me a lot during the past few months. Also I would like to thank *Dirk van der Plas* for providing the opportunity to join and present my work during one of the group meetings at Thyssenkrup TATA steel in IJmuiden.

Further I would also like to extensively thank Ing. *Bart Hoek* who is the technician at the Process & Energy department where I spent most of the time during the past months. I cannot thank you enough for the many times helping me when I was facing technical difficulties/problems during the experiments. Also thanks for the fact that you spent a lot of your valuable time providing me with some smart solutions to improve my experimental setup and giving feedback every now and then on the obtained results.

Thank you *Julia van der Geus* and *Manu Chakkingal* for your valuable input and for sharing your thoughts and numerical results with me. Also I would like to thank the rest of the TP group for the daily coffee-breaks and the friendly chatters.

Further I would like to express my sincere gratitude to my close friends and family for the moral support during the past few months. Many thanks to my wonderful roommates and other close friends for the motivating and helpful support during this period. Thanks to my lovely parents *Ourange* and *Manja* and of course to my little sister *Sedi*. Finally I would like to thank the one person who really pushed me through the past 10 months while enduring my constant absence, *Marit*.

*Nima Rounaghi*  
*Delft, October 2018*



# CONTENTS

<b>List of Tables</b>	<b>ix</b>
<b>List of Figures</b>	<b>xi</b>
<b>Nomenclature</b>	<b>xiii</b>
<b>1 Introduction</b>	<b>3</b>
1.1 Natural convection through coarse-grained porous media . . . . .	3
1.2 Blast furnace . . . . .	5
1.3 Aim of the thesis . . . . .	7
<b>2 Theory</b>	<b>9</b>
2.1 Theoretical background. . . . .	9
2.1.1 Governing Equations. . . . .	9
2.1.2 Non-dimensional numbers . . . . .	10
2.1.3 Boussinesq Approximation . . . . .	11
2.2 Boundary layers. . . . .	12
<b>3 Experimental Setup</b>	<b>15</b>
3.1 Heat transfer measurements . . . . .	15
3.1.1 Heated plate . . . . .	17
3.1.2 Cooling plate. . . . .	17
3.1.3 Temperature sensors & Data acquisition . . . . .	18
3.1.4 Working fluids and degassing procedures . . . . .	18
3.1.5 Setup procedure . . . . .	19
3.1.6 Heat losses. . . . .	19
3.1.7 Temperature monitoring procedure . . . . .	19
3.1.8 Uncertainty-analysis. . . . .	21
3.2 Coarse-grained porous media configurations . . . . .	22
3.2.1 Materials with different thermal conductivities . . . . .	22
3.2.2 Different packing types . . . . .	22
3.2.3 Materials with different sizes. . . . .	23
3.2.4 3D printed structure . . . . .	23
3.3 Particle Imaging Velocimetry . . . . .	25
3.3.1 Laser. . . . .	27
3.3.2 CCD Camera . . . . .	27
3.3.3 Hydrogel balls . . . . .	27
3.3.4 Measurement procedure. . . . .	27
3.4 Liquid Crystal Thermography. . . . .	29
3.4.1 Main components . . . . .	30
3.4.2 Liquid Crystal slurry . . . . .	30
3.4.3 Qualitative temperature color definitions . . . . .	30
3.4.4 Quantitative temperature color definitions . . . . .	30
<b>4 Results</b>	<b>33</b>
4.1 Heat transfer measurements . . . . .	33
4.1.1 Effect of sphere conductivity on natural convection heat transfer . . . . .	35
4.1.2 Effect of packing type on natural convection heat transfer . . . . .	36
4.1.3 Effect of spheres size on natural convection . . . . .	37
4.1.4 Non-covered boundary layers . . . . .	38

4.2	Natural convection flow dynamics . . . . .	39
4.2.1	Velocity fields . . . . .	39
4.2.2	Velocity distribution . . . . .	44
4.3	Temperature distributions . . . . .	49
4.3.1	Temperature distribution in the pure-fluid enclosure . . . . .	49
4.3.2	Temperature distribution in the BCT stacked enclosure . . . . .	51
<b>5</b>	<b>Conclusion</b>	<b>53</b>
<b>6</b>	<b>Recommendation</b>	<b>55</b>
6.1	Turbulent flows . . . . .	55
6.2	Extended quantitative liquid crystal experiment . . . . .	55
6.3	Pressure distribution . . . . .	56
6.4	Extended non-covered boundary layer experiment . . . . .	56
	<b>Bibliography</b>	<b>57</b>
<b>A</b>	<b>Heating pad specifications</b>	<b>61</b>
<b>B</b>	<b>Thermostatic bath specifications</b>	<b>63</b>
<b>C</b>	<b>Thermocouples and data acquisition device</b>	<b>67</b>
<b>D</b>	<b>Connex 3D printer</b>	<b>73</b>
<b>E</b>	<b>Errorbars in heat transfer experiments</b>	<b>77</b>
E.1	errorbars in the Nu-Ra calculations . . . . .	77
E.1.1	Different conductive materials . . . . .	77
E.1.2	Different packing configurations . . . . .	78
E.1.3	Different sized spheres . . . . .	78
E.1.4	3D structure . . . . .	79
<b>F</b>	<b>Velocity profiles</b>	<b>81</b>
E1	Vertical velocity profiles . . . . .	81

# LIST OF TABLES

3.1	Thermal properties of water and methanol . . . . .	18
3.2	Materials with different conductivities . . . . .	22
3.3	Properties of the packing configurations . . . . .	23
3.4	Different sized spheres . . . . .	23
3.5	Definition of the observed colors in the LCT experiments . . . . .	30
3.6	Coefficients for the fifth order polynomial T-Hue fit . . . . .	31
4.1	Reference values for the empty cavity Nu-Ra power law . . . . .	34



# LIST OF FIGURES

1.1	Heat transfer in a water filled saucepan . . . . .	3
1.2	Blast furnace . . . . .	6
2.1	Boundary layers at different Pr numbers . . . . .	10
2.2	Heat transfer in a side-heated natural convection configuration . . . . .	12
3.1	Picture of the cubical enclosure as used in the experiments . . . . .	16
3.2	Schematic sketch of the cubical enclosure as used in the experiments . . . . .	16
3.3	Heating pad . . . . .	17
3.4	Cooling plate . . . . .	17
3.5	Temperature time-series . . . . .	20
3.6	Packing configurations . . . . .	22
3.7	3D printed structure . . . . .	24
3.8	3D printed structure in the cubical enclosure . . . . .	24
3.9	Picture of the PIV setup . . . . .	25
3.10	PIV experimental setup . . . . .	26
3.11	Hydrogel ball . . . . .	27
3.12	Example of a PIV result . . . . .	28
3.13	Picture of the LCT setup . . . . .	29
3.14	LCT experimental setup . . . . .	29
3.15	Temperature-Hue data points with the corresponding best fit . . . . .	31
4.1	Convective heat transfer results in the side-heated cubical enclosure . . . . .	34
4.2	Effect of spheres with different conductivities on the convective heat transfer . . . . .	35
4.3	Effect of different packing types on the convective heat transfer . . . . .	36
4.4	Effect of different sizes of spheres on the convective heat transfer . . . . .	37
4.5	Heat transfer result of the SCP packed 3D structure . . . . .	38
4.6	Average normalized velocity fields in an empty cell for both low and high Ra-regimes . . . . .	40
4.7	Velocity fields from PhD dissertation of <i>Lankhorst</i> . . . . .	40
4.8	Average normalized velocity fields in an empty and BCT packed cell at a low Ra-regime . . . . .	41
4.9	Average normalized velocity fields in an empty and BCT packed cell at a high Ra-regime . . . . .	42
4.10	Average normalized velocity fields in a BCT packed cell for both low and high Ra-regimes . . . . .	43
4.11	Definitions of the analyzed horizontal/vertical sections . . . . .	44
4.12	Velocity profile in different $z^*$ -planes at low Ra-number . . . . .	45
4.13	Velocity profile in different $x^*$ -planes at low Ra-number . . . . .	46
4.14	Velocity profile in different $z^*$ -planes for high Ra-number . . . . .	47
4.15	Velocity profile in different $x^*$ -planes for high Ra-number . . . . .	48
4.16	Qualitative and quantitative temperature distribution in the pure-fluid enclosure . . . . .	49
4.17	Qualitative and quantitative temperature distribution in the hydrogel spheres filled enclosure . . . . .	51
E.1	Error-bars for different conductive materials . . . . .	77
E.2	Error-bars for different packing configurations . . . . .	78
E.3	Error-bars for different sized spheres . . . . .	78
E.4	Error-bars for the 3D printed structure . . . . .	79
F.1	Velocity profile in different $z^*$ -planes for low Ra-number . . . . .	81
F.2	Velocity profile in different $z^*$ -planes for high Ra-number . . . . .	82



# NOMENCLATURE

Abbreviation	Description
LCT	Liquid Crystal Thermography
PIV	Particle Imaging Velocimetry
RMS	Root-Mean-Square value
SHNC	Side-heated natural convection (empty cavity fit)

Non-dimensional number	Description
Gr	Grashof number
Nu	Nusselt number
$Nu_{corr}$	Corrected Nusselt number due to heat losses
Pr	Prandtl number
Ra	Rayleigh number

Greek symbol	Description	Units
$\alpha_f$	Thermal diffusivity of the fluid	$\frac{m^2}{s}$
$\beta$	Thermal expansion coefficient	$K^{-1}$
$\delta_M$	Momentum boundary layer thickness	m
$\delta_T$	Thermal boundary layer thickness	m
$\Gamma$	Aspect ratio of the cell L/W	[-]
$\lambda$	Laser wavelength	nm
$\lambda_{fluid}$	Thermal conductivity of the fluid	$\frac{W}{m \cdot K}$
$\lambda_{glass}$	Thermal conductivity of the glass side-walls	$\frac{W}{m \cdot K}$
$\mu$	Dynamic viscosity	Pa · s
$\nu$	Kinematic viscosity	$\frac{m^2}{s}$

<b>Greek Symbol</b>	<b>Description</b>	<b>Unit</b>
$\phi$	Porosity	[-]
$\rho$	Density	$\frac{kg}{m^3}$
$\sigma$	Distance between the side-walls and the 3D structure	m
<b>Roman Symbol</b>	<b>Description</b>	<b>Unit</b>
a	Pre-factor in the Nu-Ra power-law (empty cavity fit)	[-]
$A_{cell}$	Cross-sectional surface area of the cell	$m^2$
$A_{glass}$	Total surface of the glass side-walls	$m^2$
b	Exponent in Nu-Ra power-law (empty cavity fit)	[-]
D	Depth of the cubical enclosure	m
g	Acceleration of gravity on earth	$\frac{m}{s^2}$
h	Convective heat transfer coefficient	$\frac{W}{m^2 \cdot K}$
I	Electrical current through the heating pads	A
L	Length of the cubical enclosure	m
$P_{electrical}$	Dissipated energy from the heating strips to the heating plate	W
$Q''$	Heat flux from the heating plate	$\frac{W}{m^2}$
$T_0$	Reference temperature	$^{\circ}C$
$T_{bulk}$	Average temperature of the heated and cooled plate	$^{\circ}C$
$T_{cold}$	Average temperature of the cooled plate	$^{\circ}C$
$\Delta T$	Temperature difference between the heated and cooled walls	$^{\circ}C$
$T_{hot}$	Average temperature of the warm plate	$^{\circ}C$
$\bar{v}_x^*$	Averaged non-dimensional velocity in the x-direction ( $v_x/v_{norm}$ )	[-]
$\bar{v}_z^*$	Averaged non-dimensional velocity in the z-direction ( $v_z/v_{norm}$ )	[-]
$v_{norm}$	Normalization velocity from literature ( $\frac{\alpha}{L} Ra^{\frac{1}{2}}$ )	$\frac{m}{s}$
V	Applied voltage on the heating pad	V
W	Width of the cubical enclosure	m
$x^*$	Non-dimensional length of the cubical enclosure (x/L)	[-]
$z^*$	Non-dimensional width of the cubicle enclosure (z/L)	[-]





# 1

## INTRODUCTION

### 1.1. NATURAL CONVECTION THROUGH COARSE-GRAINED POROUS MEDIA

Natural convection is the physical phenomenon where fluid motion is generated through heat transfer by the creation of density differences because of imposed temperature gradients. This phenomenon is typically referred to as the phenomenon where warm air rises and cool air falls down and why a hot air balloon goes up. Natural convection occurs in nature, but also in daily household activities such as turning on the electrical heater when it is cold in the environment, letting hot food to cool down by placing it in a relatively cooler environment and boiling water in a saucepan (figure 1.1). Also in industrial applications such as in the steel-making process, natural convection occurs constantly. The effect of this specific phenomenon in the steel industry serves as a base for this research and is further explained and elaborated in section 1.2.

Both numerical and experimental research on side-heated natural convection in enclosures has been the subject of investigation throughout the past decades. *Lankhorst* [1] wrote his dissertation on the numerical modeling of laminar and turbulent natural convection in empty cavities. In his dissertation it was shown that in a side-heated natural convection configuration, the convective heat transfer is boundary driven. *Opstelten* [2] presented his PhD dissertation on the experimental investigation of the transition layer between laminar and turbulent natural convection in a side-heated empty cavity using interferometry and experimentally confirmed the boundary-driven convective heat transfer as numerically obtained by *Lankhorst* [1]. *Fusegi et al.* [3] published a numerical study on a differentially side-heated empty 3D enclosure where it was found that the  $v_z$  velocity was an order of magnitude smaller than the  $v_x$  and  $v_y$  velocity. The mentioned works in the empty enclosure reported a power-law for the Nu-Ra relationship. *Wang et al.* [4] also performed a numerical study on side-heated natural convection using the Lattice-Boltzman method. From their investigation they found that the inhibition of the lateral adiabatic walls on the heat transfer decreases with increasing Ra-number. They also claimed that for the first time they found an exponential scaling law in the Ra-number range between  $10^7 \leq Ra \leq 10^{10}$ .

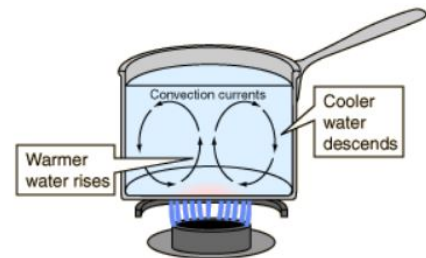


**Figure 1.1:** Convective heat transport in boiling water in a saucepan.

Several especially numerical research has already been conducted in the past decades where the effect of porous media on side-heated natural convection was investigated. In most of the scientific papers, the relative size of the grains was relatively small. Because of the small size, the flow equations through the medium can be described using Darcy's law. Here the assumption is made that inertia can be neglected with respect to viscous effects in a fluid and that the porous length scale of the porous media is small with respect to the thermal length scales. In this model it is also assumed that inertia is negligible compared to viscous forces in a fluid. [5] In the book *Convection in Porous Media* by *Nield and Bejan* [6], a detailed description for Darcian convective heat transfer through porous media is given for both natural and mixed convection. As defined by *Nield and Bejan* in [6], "a porous medium is defined as a material consisting of a solid matrix with an intercon-

*nected void.*" This matrix can be either rigid or it can undergo small deformations. A well known example of a natural porous medium is beach sand which is basically crushed rock [7]. The distribution of the pore-sizes and geometries of the sand grains are highly irregular and unique.

A large number of studies have been performed where convective heat transfer through porous media was studied using the Darcy model. *Hewitt et al.* [8] performed a numerical investigation on the effect of porous media on the heat transfer in a bottom-heated configuration for  $Ra = 2 \times 10^4$  which was a continuation on the numerical work already performed by *Otero et al.* [9]. The definition of the Ra-number in this study was adjusted in such a way that the effects of the porosity and the permeability were also taken into account. The outcome of the study was a linear empirical solution for the Nusselt number as a function of the Rayleigh number in the range of  $1750 \leq Ra \leq 2 \times 10^4$ . Also the Darcy model was used in a differentially side-heated enclosure by *Weber* [10] to develop an analytical solution for the vertical boundary layers in a porous medium. In his work, *Weber* stated that Darcy's law is only valid when the grain diameter of the porous media is smaller than the boundary layer thickness. *Lauriat and Prasad* [11] numerically investigated the effect of inertial and viscous forces on natural convection through porous media in a side-heated enclosure, by presenting the Darcy-Brinkman-Forchheimer solutions. The main observation during the study was that both the inertial and viscous effects have a significant influence on the heat transfer. The main concluding remark of the study was that the presence of a porous medium can enhance the heat transport in the enclosure relative to the pure fluid enclosure if  $\lambda_{solid} > \lambda_{fluid}$  and the porous media has a high permeability. Next to the numerical work, also some experimental studies were performed on the heat transfer through porous media where the Darcy model is included. *Fukusako et al.* [12] experimentally investigated the effect of porous media on the heat transfer in a differentially side-heated enclosure. The effects of different cell aspect ratios ( $5 < \Gamma < 26$ ) and different working fluids ( $1 < Pr < 200$ ) were tested in the porous-medium Rayleigh number range between  $10^2 \leq Ra_m \leq 10^4$ . They concluded with an empirical correlation of Nusselt with respect to  $\Gamma$ ,  $Pr$  and  $Ra$  for the mentioned Ra-number range. In order to validate the outcomes of the numerical reports, conducting experimental studies is necessary. A number of experimental studies regarding the natural convection in porous media has been reported by [13–15]. Again for these experiments, the effects of porous media is studied, where the laws of Darcian flow apply. A more extended literature review on natural convection for larger sized coarse-grained porous media is given, where the flow is considered to be non-darcian.

For larger pore sizes with respect to thermal length scales, which is referred to as coarse-grained porous media, less research is conducted with respect to porous media studies. A number of numerical research has been conducted in the past years where the effects of larger porous media (referred to as coarse-grained porous media) on natural convection was investigated. *Braga and De Lemos* [16] investigated the effect of disconnected square solid blocks on both laminar and turbulent natural convection in a 2D cavity. In their study, two different methodologies were used which are the homogeneous (porous-continuum) and heterogeneous (continuum) approaches. The withdrawn conclusion was that the Nusselt number resulting from the two models were different with respect to each other and that the difference between the two grew bigger as the Darcy number decreased. *Braga and De Lemos* continued their research in [17] where they also investigated whether there was a difference in heat transfer when using cylindrical or square geometries as porous media. The conclusion was that the average Nusselt numbers were slightly lower for the cylindrical rods than those for square rods. *Merrikh and Lage* [18] also performed a numerical investigation on natural convection in a 2D enclosure with disconnected and conducting solid blocks. They found that the strong hindrance of the blocks on the heat transfer to be dependent on a minimum number of blocks for each tested Rayleigh number. *Raji et al.* [19] numerically investigated the effect of different numbers of square solid blocks in a differentially side-heated enclosure. In this study, it was found that the heat transfer was reduced when a relatively big obstacle was subdivided into more equally sized smaller obstacles.

Also a limited number of experimental work has been performed where the effects of coarse-grained porous media have been tested in a Rayleigh-Benard configuration. *Keene and Goldstein* [20] studied heat transfer characteristics for high Ra-numbers in a bottom-heated  $279 \times 279 \times 279 \text{ mm}^3$  cubic cell which was filled with polypropylene spheres ( $D=25.4 \text{ mm}$ ) and compressed argon as the saturated fluid. The pressure of the argon was varied between 5.6 and 77 bars and in the paper it was reported that in a high Ra-regime, the heat transfer asymptotes to the homogeneous fluid layer, unless the solid media has a high conductivity. *Ataei-Dadavi* [21] performed an experimental study on thermal natural convection in coarse-grained porous media in a cavity heated from the bottom and cooled from the top. In this paper, a packed bed of relatively

large spheres was used where the ratio between the length of the cell ( $L$ ) and the diameter of the balls ( $D$ ) was set to be  $L/D=5$ . In this paper the effects of different packing types, different sphere-sizes and different thermal properties of the spherical particles on the heat transfer was investigated for Ra-numbers varying from  $10^7$  to  $10^9$ . The results obtained consisted of heat transfer data in the form of Nu-Ra relationships where it was shown that the heat transfer in the lower Ra-regime was lower with respect to pure Rayleigh-Benard convection, with the difference depending on the different configurations of the present coarse-grained porous media. At higher Ra-numbers however, an asymptotic regime exists where the heat transfer for all sphere sizes, packing types and conductivity's collapse on a single curve which is very near the pure Rayleigh-Benard convection. In his work, *Ataei-Dadavi* also performed optical experiments to visualize the effect of coarse-grained porous media on the fluid motion and temperature distributions in the bottom-heated cell. From these measurements, where hydrogel balls were used as the porous media, it was found that in the asymptotic regime the velocity magnitudes were significantly higher inside the pores in the core region than those in the lower Ra-regime.

From the literature review, it is clear that the heat transfer characteristics for coarse-grained porous media in a side-heated configuration has not been studied thoroughly yet. The experimental study described in this report is a continuation on the work of Iman Ataei Dadavi, who is a PhD-candidate and my daily supervisor at the department of Chemical Engineering, section Transport Phenomena at the Delft University of Technology. In this report, natural convection flow and heat transfer in coarse-grained porous media in a side-heated cell is analyzed and visualized. This is done primarily to get a better understanding of how natural convection occurs through coarse-grained porous media. On its turn, the values found in this experimental study can be used to validate numerical results and can eventually be used to simulate convective heat flows in a specific enclosure where relatively large solid objects are present. In the scope of the present study, the effect of coarse-grained porous media on the convective heat transfer in a side-heated enclosure is experimentally investigated. The coarse-grained porous media, as used in this study, has larger length scales with respect to the thermal and momentum length-scales in the side-heated enclosure. Therefore Darcy's law does not apply in the current experimental study.

## 1.2. BLAST FURNACE

The base of this project stems from a problem which was introduced by TATA steel, which is an Indian based global steel manufacturer with a huge factory in IJmuiden (NH) in the Netherlands. Recently, TATA steel merged with the German steel producer Thyssenkrup and is currently also referred to as Thyssenkrup TATA steel. [22] The combination Thyssenkrup TATA steel produces millions of tons of all grades of steel in their blast furnaces annually and runs for 24 hours each day for 365 days a year. The company prefers to reduce the maintenance time for the furnaces to a minimum to have a maximum possible output of steel everyday. Unfortunately, the blast furnaces are not ideal and have a certain lifetime where maintenance is required every now and then.

The blast furnace has a height of about 25 meters and consists of 3 parts, the stack, bosh and hearth. As visualized in figure 1.2, iron ore along with cokes and limestone are thrown into the stack of the blast furnace. At the bosh of the furnace, extremely hot air is blown in via nozzles causing the cokes catch fire and reaching up to temperatures near  $1300\text{ }^{\circ}\text{C}$ . Here the iron ore liquifies and is now called pig iron which contains a lot of impurities and still needs a lot of post-processing to remove the impurities. The liquefied iron then flows to the bottom of the furnace, the hearth, where it is split into a slag stream and a liquid iron stream which is tapped off. The hearth has a diameter of  $\approx 5\text{m}$ . Since the process of creating steel involves very high temperatures, it is quite a challenge to find proper refractory materials to build the furnace with. Currently a special kind of alumina based concrete is used to build the walls of the furnace which is extremely heat-resistant. [23] The extreme temperatures however still have a significant effect on the furnace wall over time and cooling of the walls is necessary to improve the life-time of the walls.

The cooling is done by spraying cooling water on the outside of the furnace walls in order to prevent refractory materials from burning out. This in combination with the hot liquid metal implies a large temperature difference between the center of the hearth and the cooler wall which results in a natural convective flow in the liquid metal. The tapping-off of the liquid metal at the hearth of the furnace causes a forced convective flow. Since some of the cokes are not burnt up during the heating process in the bosh, some of the coarse-grained porous carbon material are still present in the liquid metal as irregularly shaped chunks with

typical diameters between 10-40 mm. The presence of these chunks and the natural convective flow causes asymmetries in the heat flows and eventually results in complex temperature distributions at the walls. The direct result of these asymmetries are the creation of local hotspots close to the walls which have extreme temperatures. On their turn, these hotspots lead to a shorter lifetime for the furnace walls and have a negative impact on the productivity of the whole process.

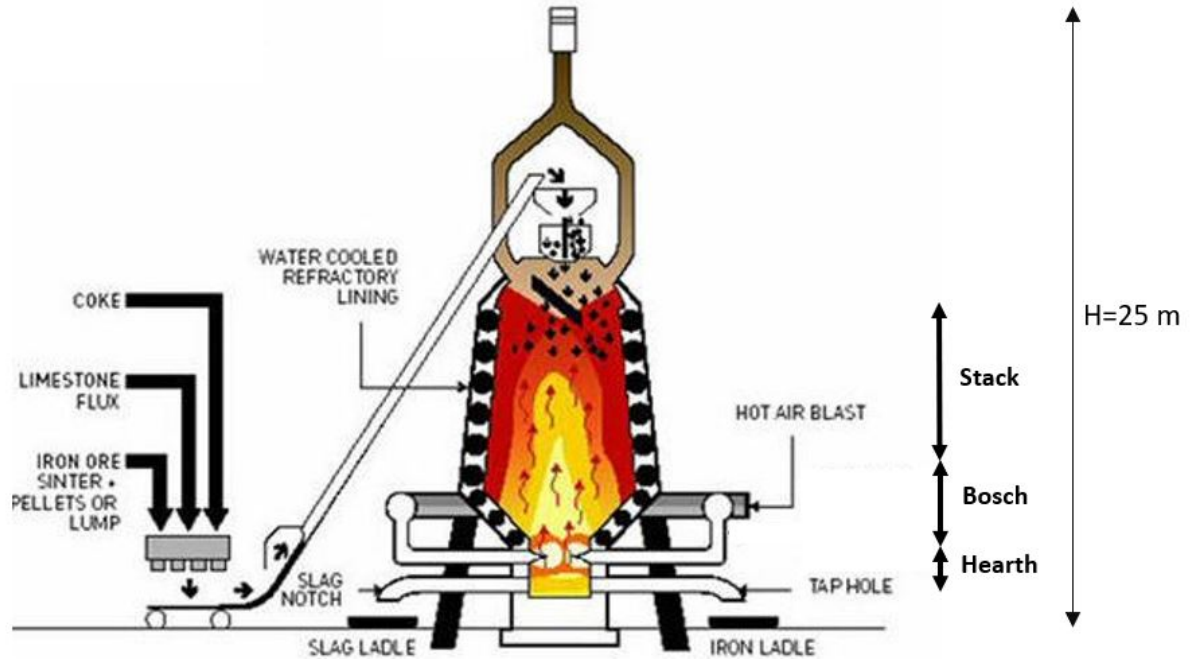


**Figure 1.2:** A schematic overview of the blast furnace, as used to manufacture steel by Thyssenkrup Tata steel in Ijmuiden. The time between when the iron ore enters the stack of the furnace and is tapped off at the hearth of the furnace is between 6 and 8 hours. [24]

Thyssenkrup TATA steel wants to have an as detailed as possible analysis for this problem in order to come up with a possible solution. By means of numerical simulations and validating experiments the problem can be approached scientifically and the fundamental problem is mapped out. Because liquid steel ( $Pr \approx 0.01$ ) has a very high temperature and is opaque, experiments are not practical to do with liquefied steel. Therefore, scaled experiments with non-opaque substances which are liquid at room temperature and non-toxic are proposed to study what the effect of coarse-grained porous media is on the heat transfer.

### 1.3. AIM OF THE THESIS

In this MSc-thesis project, a very similar experimental study will be performed on natural convection in coarse-grained porous media. This project will consist of studying side-heated natural convection through a packed bed of spheres to see how the convective heat transfer will be affected. In addition to finding empirical heat transfer relationships, also optical measurements will be performed to visualize the fluid flow quantitatively in a side-heated enclosure. Finally a qualitative investigation will be performed to observe how the temperature distribution will be in the side-heated configuration and how this is affected in the presence of coarse-grained porous media.

#### RESEARCH (SUB)QUESTION(S)

The core of this experimental investigation is to find an answer to the following research question:

*"What is the effect of coarse-grained porous media on the natural convective heat transfer, flow characteristics and temperature distribution in a side-heated enclosure?"*

In order to give a proper answer to the core research question, a set of four sub-questions are formulated and researched in advance. The coarse-grained porous media is referred to as 'particle'.

1. What is the effect of the sphere materials with different conductivity's on heat transfer in a side-heated natural convection configuration?
2. What is the effect of particle size on a side-heated natural convection configuration?
3. What is the effect of packing type on heat transfer in a side-heated natural convection configuration?
4. What is the effect of coarse-grained porous media on the flow and temperature distribution in a side-heated natural convection configuration?

In this study, a reference data-set is defined as the natural convection in a pure fluid cavity which is not filled with coarse-grained porous media. The effects of the coarse-grained porous media on the heat transfer has been compared to the reference data-set.

#### OUTLINE OF THE REPORT

The present report consists of six chapters. In chapter 2, a brief theoretical overview on natural convection is given where the governing equations as well as all of the non-dimensional numbers are discussed. Afterwards, in chapter 3, the experimental setups are explained which were used to conduct the heat transfer and optical experiments. Later on in chapter 4, the results of the heat transfer experiments are presented and provided with a proper explanation. Also the results of the optical experiments to visualize the flow velocity and temperature distributions are included in this chapter. In chapter 5 a conclusion is formulated and discussed in order to answer the (sub)question(s) in the section on how the convective heat transfer is affected by the coarse-grained porous media. Finally in chapter 6, a recommendation is written to reflect on the performed experiments and to elaborate what scientific studies can be performed in future experiments to understand the effect of the presence of coarse-grained porous media even more.



# 2

## THEORY

In this chapter, a brief theoretical background on natural convection and its corresponding equations and assumptions are given as used in this report. Also the important characterizing non-dimensional numbers which describe heat transfer in natural convection are presented and explained thoroughly. Later on in this chapter, a literature review is given on what is already known in science in the field of natural convection in coarse-grained porous media.

### 2.1. THEORETICAL BACKGROUND

Natural convection, also known as free convection, is the phenomenon where bulk fluid motion in a liquid occurs due to buoyancy forces. The buoyancy induced flow is caused by the presence of gravity and small density differences in the fluid which are on their turn caused by the presence of temperature gradients in the fluid. In this process, thermal expansion of the fluid plays an important role as the more dense components will fall down while the less dense components will rise which eventually will lead to bulk fluid motion in a steady-state situation. [25]

#### 2.1.1. GOVERNING EQUATIONS

The heat transfer due to natural convection can be described by the three coupled equations which are the continuity equation (2.1), the Navier-Stokes momentum equation (2.2) and the thermal energy equation (2.3) as presented in the set of equations below. [26]

$$\underbrace{\frac{\partial \rho}{\partial t}}_{\text{Time-rate of change}} + \underbrace{\frac{\partial}{\partial x_j}(\rho v_j)}_{\text{Velocity divergence}} = 0 \quad (2.1)$$

$$\rho \left( \underbrace{\frac{\partial v_i}{\partial t}}_{\text{Time-rate of change}} + \underbrace{v_j \frac{\partial v_i}{\partial x_j}}_{\text{Convective term}} \right) = \underbrace{-\frac{\partial p}{\partial x_i}}_{\text{Pressure gradient}} + \underbrace{\mu \frac{\partial^2 v_i}{\partial x_j^2}}_{\text{Viscous term}} + \underbrace{\rho g_i}_{\text{Buoyant term}} \quad (2.2)$$

$$\underbrace{\frac{\partial T}{\partial t}}_{\text{Time-rate of change}} + \underbrace{v_j \frac{\partial T}{\partial x_j}}_{\text{Convective heat transfer}} = \underbrace{\alpha \frac{\partial^2 T}{\partial x_j^2}}_{\text{Heat transfer by thermal diffusivity}} \quad (2.3)$$

Under the assumption that the fluid is incompressible and Newtonian, the velocity divergence in the continuity equation 2.1 vanishes, leaving that the density time-rate of the change is zero.

When in a heat transfer problem a steady-state situation is reached, the *Time-rate of change* in both the momentum and energy equations vanishes leaving only the convective term on the left hand side. The pressure gradient is defined as a physical quantity which describes the change of pressure per unit distance. The

negative sign in front of the term is because the fluid always flows from a higher pressure area to a lower pressure area. The viscous term in equation 2.2 represents the force due to the viscosity of the working fluid. The buoyant term is the force due to buoyancy and occurs only when there is a gravitational acceleration present. Finally,  $\alpha$  on the right hand side of equation 2.3 represents the thermal diffusivity of a fluid and is defined by  $\alpha = \frac{\lambda}{\rho C_p}$  where  $\lambda$  is the thermal conductivity,  $\rho$  is the density and  $C_p$  is the specific heat capacity of the working fluid.

### 2.1.2. NON-DIMENSIONAL NUMBERS

Natural convective heat transfer through a fluid can be described using the characterizing non-dimensional numbers which are the Prandtl, Grashof/Rayleigh and Nusselt number.

The Prandtl-number (equation 2.4) of a fluid is defined as the ratio between the kinematic viscosity and thermal diffusivity and is a fluid property where  $\nu$  is the kinematic viscosity of the fluid. It can be seen as the ratio between the momentum boundary layer thickness and the thermal diffusive boundary layer thickness in a fluid. When  $Pr \ll 1$  the thermal diffusion dominates over the momentum diffusion while the momentum diffusion dominates over the thermal diffusion when  $Pr \gg 1$  [27]. In figure 2.1 the thicknesses of the thermal ( $\delta_T$ ) and momentum ( $\delta_M$ ) boundary layers are shown for  $Pr \ll 1$  and  $Pr \gg 1$ .

$$Pr = \frac{\text{Kinematic viscosity}}{\text{Thermal diffusivity}} = \frac{\nu}{\alpha} \quad (2.4)$$

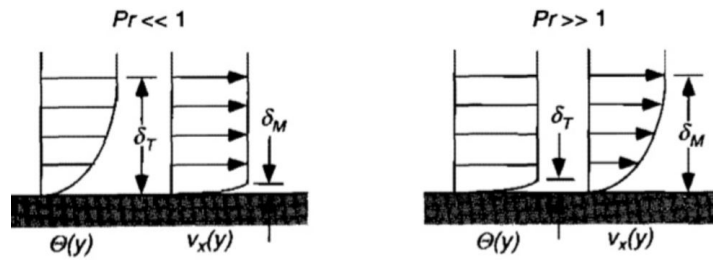


**Figure 2.1:** Thermal and momentum boundary layer behaviour at different Pr-numbers. A typical fluid with  $Pr \ll 1$  is liquid metal while engine oil is a typical fluid with  $Pr \gg 1$ . [28, 29].

The Grashof-number (equation 2.5) is defined as the ratio between the buoyant force because of the present temperature gradient and the viscous force. When  $Gr$  is large, the buoyant force dominates over the viscous force and when  $Gr$  is small, the viscous force dominates over the buoyant force. [30]

$$Gr = \frac{\text{Buoyant force}}{\text{Viscous force}} = \frac{\beta g \Delta T L^3}{\nu^2} \quad (2.5)$$

The Rayleigh-number (equation 2.6) is defined as the the Prandtl corrected Grashof number and equals the product of the Grashoff and Prandtl number. In this non-dimensional number,  $\beta$  is the fluid thermal expansion coefficient,  $g$  is the acceleration due to gravity,  $\Delta T$  is the temperature difference between the heated and cooled side and  $L$  is the distance between the heated and cooled sides. It gives a measure in how much the buoyancy driven force dominates over the dampening effects of viscosity and/or thermal diffusivity.[26]

$$Ra = \frac{\text{Buoyant force}}{\text{Diffusive force}} = Pr \times Gr = \frac{\beta g \Delta T L^3}{\alpha \nu} \quad (2.6)$$

The physical meaning of the Nusselt-number (equation 2.7) is that it is the ratio between the total heat transfer with respect to the conductive heat transfer. The Nusselt-number is a responsive non-dimensional number on the Pr- and Ra-numbers and shows whether a heat transfer process is conductive dominant or convective dominant. In equation 2.7,  $h$  is the convective heat transfer coefficient,  $\lambda_f$  is the thermal conductivity of the fluid and  $Q''$  is the applied heat flux which can be expressed as how much power,  $P_e$ , per unit area,  $A_f$ , is applied  $\left(\frac{P_e}{A_f}\right)$ . [31]

$$Nu = \frac{\text{Total heat transfer}}{\text{Conductive heat transfer}} = \frac{hL}{\lambda_f} = \frac{Q''L}{\lambda_f\Delta T} \quad (2.7)$$

In a heat transfer system, Nu-number has a minimum value of  $Nu=1$  since there will always be conduction through the fluid. When convection starts to play a role in the heat transfer through the fluid, the Nu-number increases and a distinction can be made between a pure conductive or convective regime. [32]

### 2.1.3. BOUSSINESQ APPROXIMATION

The Boussinesq approximation implies that all parameters ( $\mu$ ,  $\rho$ ,  $\alpha$ ,  $g$ ) in the coupled equations 2.1, 2.2 and 2.3 can be taken as constant values associated to a reference temperature,  $T_0$ . Since the density is assumed constant at some reference temperature, the used fluid can be treated as an incompressible fluid. Also the temperature is assumed to be constant with small fluctuations around a reference temperature,  $T_0$ . The same can then be said for the density which is taken as  $\rho = \rho_0 + \Delta\rho$  where the deviation  $\Delta\rho$  can be taken sufficiently small such that  $\Delta\rho \ll \rho_0$ . [26][33]

In a thermodynamic equilibrium, the density state of a general fluid can be described by two variables, namely: pressure,  $p$  and temperature,  $T$ . The relation between the two variables is given underneath in equation 2.8.

$$\begin{aligned} d\rho &= \left.\frac{\partial\rho}{\partial p}\right|_T dp + \left.\frac{\partial\rho}{\partial T}\right|_p dT \\ \frac{d\rho}{\rho} &= \frac{1}{\rho} \left.\frac{\partial\rho}{\partial p}\right|_T dp + \frac{1}{\rho} \left.\frac{\partial\rho}{\partial T}\right|_p dT \\ \frac{d\rho}{\rho} &= k_T dp - \beta dT \end{aligned} \quad (2.8)$$

In the above equation,  $k_T$  represents the isothermal compressibility coefficient and  $\beta$  ( $K^{-1}$ ) represents the thermal expansion coefficient which is defined as  $\beta = -\frac{1}{\rho} \left.\frac{d\rho}{dT}\right|_{T=T_0}$ . Under the assumption that the fluid is incompressible, the first term on the right-hand-side can be neglected and the remaining equation is then reduced to:

$$\frac{d\rho}{\rho} = -\beta dT \quad (2.9)$$

Solving the first order differential equation using  $\rho_0$  as the initial condition at  $T_0$ , then gives:

$$\rho = \rho_0 e^{-\beta(T-T_0)} \quad (2.10)$$

Since  $\rho = \rho_0 + \Delta\rho$  and  $\Delta\rho \ll \rho_0$ , a Taylor expansion is introduced such that:

$$\rho(T) = \rho(T_0) + \left.\frac{d\rho}{dT}\right|_{T=T_0}(T-T_0) + \dots + \text{H.O.T.} = \rho_0[1 - \beta(T-T_0)] \quad (2.11)$$

where the restriction holds that  $\beta|(T-T_0)| \ll 1$ . Now replacing  $\rho$  in equation 2.2 by the expression in 2.11 for  $\rho(T)$ , gives:

$$\rho_0 \left( \frac{\partial v_i}{\partial t} + v_j \frac{\partial v_i}{\partial x_j} \right) = - \frac{\partial p}{\partial x_i} + \mu_0 \frac{\partial^2 v_i}{\partial x_j^2} + \rho_0 g_i [1 - \beta_0 (T - T_0)] \quad (2.12)$$

$$\frac{\partial v_i}{\partial t} + v_j \frac{\partial v_i}{\partial x_j} = - \frac{\partial}{\partial x_i} \left( \frac{p}{\rho_0} + gz \right) + \nu_0 \frac{\partial^2 v_i}{\partial x_j^2} - g \beta_0 (T - T_0)$$

where the last term in equation 2.12 is also referred to as the buoyant term and plays a prominent role in natural convective flows. Together with the incompressible continuity equation 2.13 and the energy equation 2.14, the above equation represent the boussinesq equations which are the governing equations in free natural convection.

$$\frac{\partial v_i}{\partial t} = 0 \quad (2.13)$$

$$\frac{\partial T}{\partial t} + v_j \frac{\partial T}{\partial x_j} = \alpha \frac{\partial^2 T}{\partial x_j^2} \quad (2.14)$$

## 2.2. BOUNDARY LAYERS

In the process of heat transfer due to natural convection in a side-heated cavity, the bulk of the flow takes place near the walls. This near-wall motion behaviour can be described by the momentum and thermal boundary layers and is dependent on the Ra-number. The momentum boundary layer is a thin layer very close the wall where the effect of viscous forces are significant. In this region, the flow changes quite rapidly in the wall normal direction, but very slowly in the direction along with the stream. [26]

The fluid which is very close to the heating (cooling) wall has a lower (higher) density than the fluid which is further away. By means of the buoyancy force, the less dense liquid at the heated plate rises and pulls along the surrounding heavier fluid. At the cooling plate the opposite process happens where the more dense fluid flows down entraining the 'less dense' fluid from the surrounding region. In general, the velocity of the fluid motion is zero at a solid boundary which is referred to as the no-slip condition. [34] In figure 2.2a the thermal and momentum boundary layers are depicted near a wall in a steady-state situation. In a cavity where the left side is heated and the right side is cooled, a circular motion near the boundaries occurs as shown in figure 2.2b.

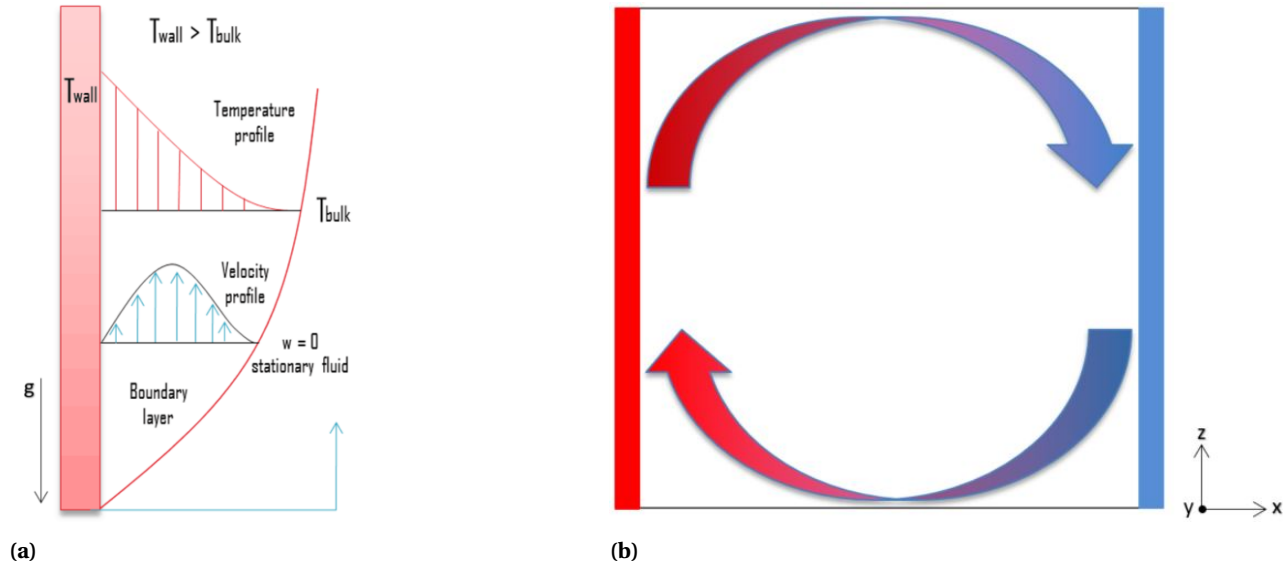


**Figure 2.2:** Global representation of how the heat is transferred by convection in a side-heated natural convection configuration. a) Graphical representation of the momentum and thermal boundary layer near the wall surface [35] b) Convective heat transfer in a side-heated cavity. The left (right) wall is heated (cooled) and the fluid flows in a clock-wise circular direction.<sup>1</sup>

<sup>1</sup>Figure 2.2b created based on the description as given by Hanjalic et al. in [26].

The thickness of the thermal boundary layer also depends on how much bigger the convection is with respect to the conduction. From *Bejan* [36], as cited in [18], the relative thickness of the boundary layer in a side-heated configuration as a function of the Ra-number is given by:

$$\frac{\delta}{L} = Ra^{-\frac{1}{4}} \quad (2.15)$$

where  $\frac{\delta}{L}$  is the non-dimensional ratio between the boundary-layer thickness and the length between the warm and cold wall. The above relationship is only valid for laminar flow regimes.



# 3

## EXPERIMENTAL SETUP

In this research the effects of coarse-grained porous media on the convective heat transfer in a side-heated cell is studied using three different methods. Starting off, heat transfer measurements are performed by varying and monitoring the applied temperatures for both the warm and cool plate and measuring the heat flux at the warm plate. In this way, Nu-Ra data-points can be obtained which are the non-dimensional numbers needed to quantify heat transfer. Secondly, a quantitative analysis of the fluid flow is performed using the Particle Imaging Velocimetry (PIV) technique where eventually the mean velocity field is acquired. Lastly, both a qualitative as well as a quantitative analysis are performed on the temperature distribution inside the cell using Liquid Crystal Thermography (LCT). The same side-heated natural convection cell is used for all three types of experiments, as described in section 3.1. In this chapter all three experimental set-ups and measurement techniques are accurately described.

### 3.1. HEAT TRANSFER MEASUREMENTS

The goal of the heat transfer measurements is to see how the heat flow in a side-heated closed cavity is affected by the presence of coarse-grained, spherical balls. The effect of different materials with different thermal conductivities, different packing types and different sphere sizes were studied. As a reference curve, the heat transfer in a cell filled with only the working fluid was used. In all the experiments a cubical cell was used with equal length, width and depth ( $L = W = D = 77\text{mm}$ ), thus with a cell-aspect ratio of  $\Gamma = L/W = 1$ . As the working fluids, water and methanol were used.

A picture of the cell which was used for this part of the study is given in figure 3.1 and a schematic overview is given in figure 3.2. The isolated left wall was heated, using heating pads while the right wall was cooled, using a thermostatic bath. The surrounding walls of the cell were made of glass and were covered with polystyrene blocks during the heat transfer experiments. The whole setup was placed on a solid piece of strongly-insulating Styrofoam block to reduce the heat leakage from the heating plate to the environment and was then positioned in a cage-construction which enabled to tilt the cell in any desired position. The position used in this study was the side-heated case.

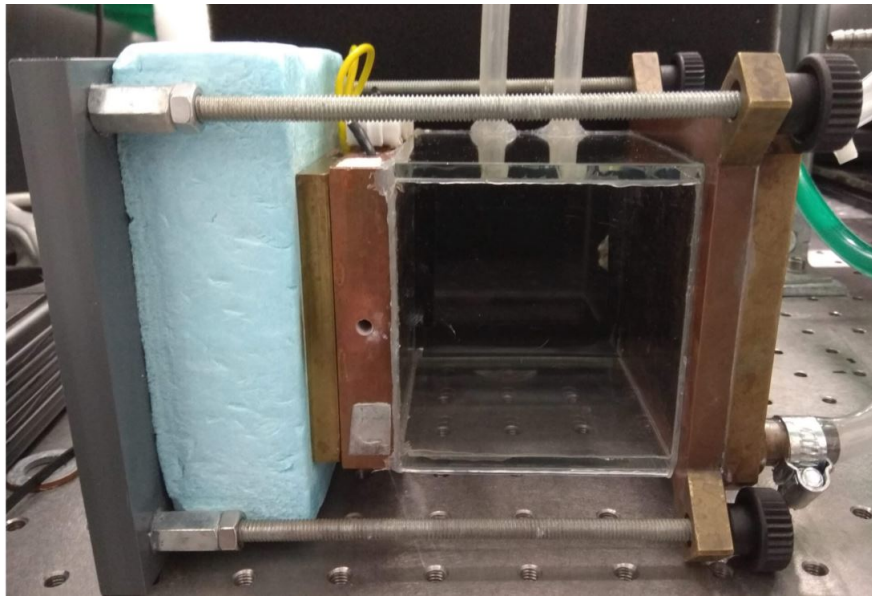


**Figure 3.1:** Picture of the left (right) heated (cooled) cubical enclosure. In this picture, the styrofoam blocks around the glass side-walls are not included. The different parts of the cell are explained in figure 3.2.

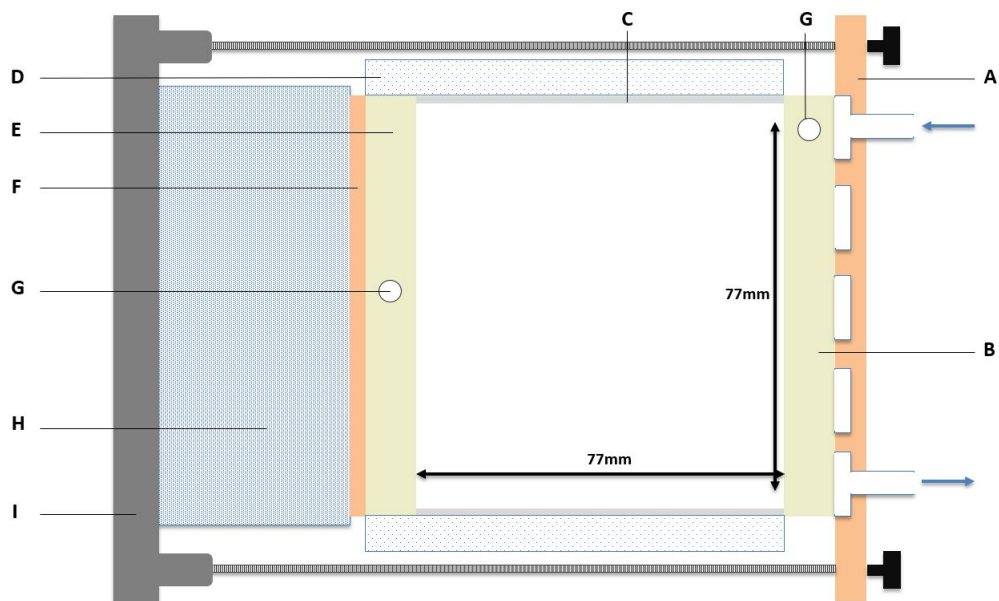


**Figure 3.2:** Schematic front view of the side-heated cell as used for the heat transfer experiments. A) Square copper plate where the channel for the cooling water is milled internally, B) cooled (right) copper plate which is soldered on the cooled channel where cooled water can flow through, C) glass-side walls, D) 30mm styrofoam blocks to minimize heat-leakage to the environment, E) warm (left) copper plate which is soldered to part F) where heating pads are glued on and which are directly connected to a power supply. G) Drilled holes in the copper (left and right) plates where four PT-100 temperature sensors can be inserted, H) insulating block of Styrofoam to minimize heat losses at the warm plate, I) Cage construction where the whole setup is clamped in.

### 3.1.1. HEATED PLATE

The warm plate consists of a copper plate where underneath an electrical heating pad ( $L \times W = 77 \times 77 \text{ mm}^2$ ) is glued on. The heating pad is then included in a simple electrical circuit, as shown in figure 3.3, where the applied power can be varied. The heating pad is a Minco HK5955S heater with a maximum power of  $\approx 180 \text{ W}$  at  $50^\circ \text{C}$ . The maximum value reached in the experiments however, is  $33^\circ \text{C}$ . In appendix A, the specifications of the heating pad are presented and elaborated.

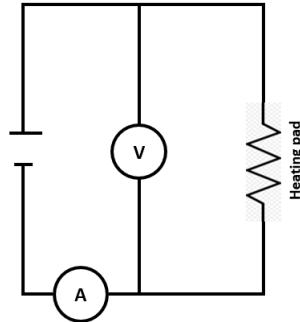


**Figure 3.3:** Electrical circuit including the power supply, Volt-meter, Ampère-meter and the heating pad.

In the above circuit, a voltage ( $V$ ) is applied by the power supply and the associated current ( $I$ ) can be read off. The product of the voltage and current then gives the electrical applied power. The heat flux,  $Q''_{heat}$ , through the heating pad on the warmed plate is then given by:

$$Q''_{heat} = \frac{P_{electrical}}{A_{cell}} \quad (3.1)$$

where  $P_{electrical}$  is the applied electrical power and  $A_{cell}$  is the vertical cross-section of the used cell. To reduce the vertical heat leakage, the warm plate rests on a 50 mm block of Styrofoam, and the cell is covered by polystyrene insulating sheets.

### 3.1.2. COOLING PLATE

The cooling plate consists of two copper plates which are soldered together (part A) and B) of figure 3.2). In the plate of part A) a simple channel pattern is milled where the cooled water can flow through such that the plate is cooled uniformly throughout its surface (figure 3.4). The water is pumped around with a constant flow rate and the maximum temperature gradient between the inlet and outlet is observed to be  $0.04^\circ \text{C}$  at its maximum.

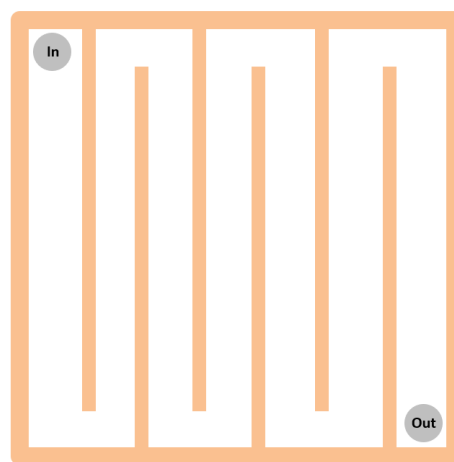


**Figure 3.4:** Horizontal cross-section of the channels in the cooling plate where the cooled water can flow through via the in- and outlet.

The water is cooled and pumped around using a thermostatic bath (Julabo FP51). In appendix B, a more detailed description of the specifications of the cooling device is given.

### 3.1.3. TEMPERATURE SENSORS & DATA ACQUISITION

The temperature sensors used in this study are PT-100 resistance thermometers of the type Omega Engineering RTD-3-1PT100K2528 with an accuracy of  $\pm 0.03^\circ\text{C}$ . These sensors are then connected to an Omega RTD PT-104A data acquisition module which translates the acquired temperatures in a logging software where the accurate temperatures were monitored. In both the warm and cooled plate, two temperature sensors were inserted to get an as accurate as possible temperature measurement. Because the temperature is not distributed perfectly uniformly in the heating plate (measured non uniformity of  $\pm 0.04^\circ\text{C}$  at its maximum), the average of both monitored temperature was taken. In appendix C a more detailed explanation of the specs of both the temperature sensor and data acquisition device are given.

### 3.1.4. WORKING FLUIDS AND DEGASSING PROCEDURES

The working fluids used in this study are Demi-water and methanol. Demi-Water is used for the lower range of Ra-numbers ( $1.6 \times 10^7 < Ra < 2.4 \times 10^8$ ) while methanol is used for the higher range of Ra-numbers ( $1.5 \times 10^8 < Ra < 1.9 \times 10^9$ ). This is because methanol has higher thermal expansion coefficient and therefore a higher Ra-numbers can be reached. Martin Steunebrink [37] collected the temperature dependent thermophysical properties of the working fluids for a temperature range of  $20^\circ\text{C} \leq T_{bulk} \leq 25^\circ\text{C}$ . In table 3.1 an overview of the fitted coefficients for the thermophysical properties of water and methanol are given as reported by [37]. The coefficients a, b and c from table 3.1 (except  $\beta$  and  $\nu$  for water) can be used in equation 3.2 where  $\phi$  denotes the temperature dependent property interested in. The coefficients for  $\beta$  and  $\nu$  for water can be used in equation 3.3.

$$\phi\{T(K)\} = a + b \times T(K) \quad (3.2)$$

$$\phi\{T(^{\circ}\text{C})\} = a \times e^{\frac{-T(^{\circ}\text{C})}{b}} + c \quad (3.3)$$

**Table 3.1** List of the coefficients needed to calculate the thermophysical properties of both water and methanol as reported by Steunebrink [37] who got the experimental data from the Dortmund databank [38]. The reported coefficients are valid for a temperature range of  $20.0^\circ\text{C} \leq T_{bulk} \leq 25.0^\circ\text{C}$ . Also for each property, the value is given for  $T_{bulk} = 22.0^\circ\text{C}$ , which was held as the bulk temperature in the cell during the experiments.

Property	Symbol	Unit	Coefficients	Water	Methanol
Kinematic viscosity	$\nu$	$\left[\frac{\text{m}^2}{\text{s}}\right]$	a	$1.439 \times 10^{-6}$	$3.400 \times 10^{-6}$
			b	31.332	$-9.033 \times 10^{-9}$
			c	$2.548 \times 10^{-7}$	-
			22.0 °C	$9.679 \times 10^{-7}$	$7.339 \times 10^{-7}$
Volumetric expansion coefficient	$\beta$	$[K^{-1}]$	a <sup>1</sup>	$-1.130 \times 10^{-3}$	$-1.832 \times 10^{-5}$
			b	88.671	$4.360 \times 10^{-6}$
			c	$1.100 \times 10^{-3}$	-
			22.0 °C	$2.183 \times 10^{-4}$	$1.269 \times 10^{-3}$
Thermal conductivity	$\lambda$	$\left[\frac{\text{W}}{\text{m} \times \text{K}}\right]$	a	$-3.573 \times 10^{-1}$	$3.123 \times 10^{-1}$
			b	$3.250 \times 10^{-3}$	$-4.108 \times 10^{-4}$
			22.0 °C	0.602	0.191
Thermal diffusivity	$\alpha$	$\left[\frac{\text{m}^2}{\text{s}}\right]$	a	$1.340 \times 10^{-7}$	$1.937 \times 10^{-7}$
			b	$4.300 \times 10^{-10}$	$-3.303 \times 10^{-10}$
			22.0 °C	$1.435 \times 10^{-7}$	$9.621 \times 10^{-8}$
Heat capacity	$C_p$	$\left[\frac{\text{J}}{\text{kg} \times \text{K}}\right]$	a	-	$5.694 \times 10^2$
			b	-	6.619
			22.0 °C	$4.182 \times 10^3$	$2.523 \times 10^3$
Density	$\rho$	$\left[\frac{\text{kg}}{\text{m}^3}\right]$	a	-	$1.073 \times 10^3$
			b	-	-0.962
			22.0 °C	$0.998 \times 10^3$	$0.789 \times 10^3$
Prandtl number	Pr	[-]	22.0 °C	6.747	7.628

<sup>1</sup>This value was reported incorrectly in the report of Steunebrink. The value reported was  $1.130 \times 10^{-3}$  while the correct value should be  $-1.130 \times 10^{-3}$

Since there is always some air dissolved in the working fluids, as mentioned above, a degassing procedure must be followed to remove these gas-bubbles. Especially the gas-bubbles which form at the warm and cold copper plate can hinder the heat transfer in the cell because of their very low thermal conductivity with respect to the working fluid in the cell. The demi-water was degassed using a kettle where the water was cooked for 3-4 minutes and all of the gas-bubbles were removed. It then took about 45 minutes for the water to cool down and to be able to use it for a heat transfer experiment. Since methanol is a more flammable kind of fluid, it was cooked in its bottle with its cap half-open for 2 hours in an oven. The oven was heated until  $50\text{--}53^\circ\text{C}$  which is well below the boiling point of methanol ( $65^\circ\text{C}$  [39]). In this way all of the gas-bubbles in the methanol were removed and a heat transfer experiment for the higher Ra-numbers could be started.

### 3.1.5. SETUP PROCEDURE

The procedure of testing the effects of coarse-grained porous media started off with de-gassing the interested working fluid. While the de-gassed fluid was cooling down, the desired balls were placed in the natural convection cell in the desired stacking type. Once the working fluid was cooled down, it was poured down with a slow flow-rate to prevent air bubbles being trapped in between the balls and remaining gas-bubbles were removed. Finally the cooling plate was clamped on top of the cell and the temperature sensors were inserted in both the heating and cooling plate. The cell was then turned on its side to achieve a side-heated configuration and the tilt-angle was adjusted in such a way that the cell was completely leveled and the measurement started off.

### 3.1.6. HEAT LOSSES

In order to obtain an accurate temperature measurement, the heat leakage from the inside of the cell to the environment should be reduced to a minimum. The four side-walls are made from glass which was done on purpose to ensure optical accessibility and are attached to the cooling and heating plate using silicon glue. To achieve the minimum heat leakage, 30 mm thick polystyrene blocks were placed on all four walls to reduce the heat losses to the environment and the average temperature of the cell was kept equal to the ambient temperature. However there are some heat losses due to conduction through the side-walls which should be taken into account.

The heat losses in the cell for both water and methanol were determined by performing a pre-experiment before starting the real heat transfer experiments. In this experiment, the same setup procedure was followed as described in subsection 3.1.5, but the cell was only filled with the working fluid (water and methanol). The cell was heated from the top and cooled from the bottom such that in theory only conduction should take place, thus  $Nu=1$ . However, the acquired Nu-number appeared to be bigger than 1 which means that also a small amount of heat was dissipated through the side walls as heat losses. This value was then used as the correction term and was simply subtracted from the measured Nusselt number, as described in equation 3.4.

$$Nu_{final} = Nu_{measured} - \chi_i \quad i = \text{water, methanol} \quad (3.4)$$

In the above equation (eq. 3.4),  $\chi$  represents the entire heat loss of the system and is subtracted from the measured Nu-number to obtain the final Nu-number. From the pre-experiment it was found that  $\chi_{water} = 1.1$  and  $\chi_{methanol} = 3.5$ .

### 3.1.7. TEMPERATURE MONITORING PROCEDURE

The monitoring of the temperature was done using the data acquisition device and its associated logging software. During each experiment, a total of 6 different temperature differences were applied and measured which took approximately 45-90 minutes per measurement. The temperature difference ( $\Delta T$ ) was varied between  $2^\circ\text{C}$  and  $21^\circ\text{C}$  in six consequent steps. In each step, the power to the heating pad and the temperature of the cold plate was adjusted in agreement with the corresponding temperature difference. The temperatures of the hot and cold wall were set in such a way that the bulk temperature ( $T_{bulk} = \frac{T_h + T_c}{2}$ ) was set to  $22.0 \pm 0.2^\circ\text{C}$  to be in accordance with the room temperature to minimize the differences in temperature between the fluid and the environment. Also a constant Prantl-number is ensured using this specific bulk temperature.

In figure 3.5 on the next page, a time-series of the temperature measurement for two temperature differences is shown. The time on the x-axis is in seconds. At the end of each measurement, the exact temperature

difference  $\Delta T$  and the power was read-off and used in equations 2.6 and 2.7 to calculate the Rayleigh and Nusselt number respectively.

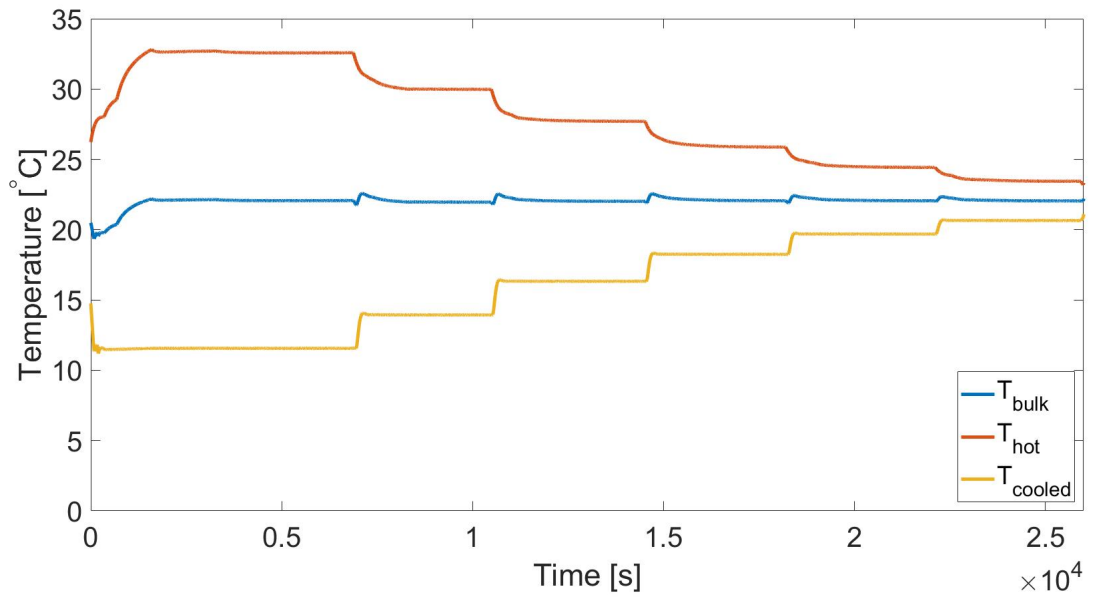


**Figure 3.5:** Time-series of a temperature measurement including six temperature differences. It took 45-90 minutes per measurement to reach a steady-state. Red line: hot wall temperature, yellow line: cold wall temperature, blue line: bulk temperature and the blue line: temperature difference between hot and cold wall.

### 3.1.8. UNCERTAINTY-ANALYSIS

The experimental results as obtained in the heat transfer measurements are affected due to instrumentation errors and uncertainties in physical parameter values as reported in literature. The relative total uncertainties in the calculation of the two most important non-dimensional numbers in heat transfer (Nu and Ra) are reported in equations 3.5 and 3.6.

$$\frac{dNu}{Nu} = \sqrt{\left(\frac{dq''}{q''}\right)^2 + \left(\frac{dL}{L}\right)^2 + \left(\frac{d\lambda}{\lambda}\right)^2 + \left(\frac{d\Delta T}{\Delta T}\right)^2} \quad (3.5)$$

$$\frac{dRa}{Ra} = \sqrt{\left(\frac{d\beta}{\beta}\right)^2 + \left(\frac{dg}{g}\right)^2 + \left(\frac{d\alpha}{\alpha}\right)^2 + \left(\frac{dv}{v}\right)^2 + \left(\frac{d\Delta T}{\Delta T}\right)^2 + \left(3\frac{dL}{L}\right)^2} \quad (3.6)$$

In this uncertainty analysis, the assumption is made that the errors in the thermophysical parameters of the working fluids ( $\alpha, \beta, \nu, \lambda$ ) are all in a 1% range within the reported values by *Steunebrink* [37]. Thus  $\frac{d\alpha}{\alpha} = \frac{d\beta}{\beta} = \frac{d\lambda}{\lambda} = \frac{d\nu}{\nu} = 1\%$ . The error in the acceleration constant due to gravity is also set to be  $\frac{dg}{g} = 1\%$  [40].

The errors in the actual measured variables could be determined more accurately because the producer of the measuring devices already reported the corresponding errors. The relative uncertainty in the length of the cell,  $L$ , equals  $dL = 1 \times 10^{-4}$  m and is based on the given measurement error in the caliper package leaflet. The relative error in the temperature measurements in the warm and cooled plate was observed during the experiments to be about  $d\Delta T_{hot} = 0.07^\circ C$  for the hot plate and  $d\Delta T_{cold} = 0.1^\circ C$  for the cold plate. This error was observed when the temperatures of both plates were monitored using two temperature sensors on a different position. By also taking into account the error of the thermal sensor, the total measurement error for the difference in temperature between the heated and cooled wall is then calculated to be  $d\Delta T_{total} \approx 0.1^\circ C$ . Also an error in the heat flux,  $q''$ , was observed during the measurements which equals  $0.03 W/m^2$ . [37]

The measured Nu-number still has to be corrected with the correction term,  $\chi$ , because of the heat losses as presented in equation 3.4.

Since the pre-experiments performed to acquire the heat losses through conduction were performed in the same way as the heat transfer experiments were performed, the relative uncertainty in the correction term was calculated in the same way as shown in equation 3.5. The definition for the total errorbar in the heat transfer is then defined in equation 3.7 below:

$$\frac{dNu_{final}}{Nu_{final}} = \sqrt{2} \sqrt{\left(\frac{dq''}{q''}\right)^2 + \left(\frac{dL}{L}\right)^2 + \left(\frac{d\lambda}{\lambda}\right)^2 + \left(\frac{d\Delta T}{\Delta T}\right)^2} \quad (3.7)$$

## 3.2. COARSE-GRAINED POROUS MEDIA CONFIGURATIONS

In this sub-chapter, an overview is given of the different types of coarse-grained porous media which were tested in this study. The coarse-grained porous media as used for this study consists of spherical particles ranging from 5-15.4 mm diameter. The effect of the presence of the media was tested on the heat transfer in the side-heated natural convection cell. The different configurations included different material types, different stacking types, and different sphere sizes.

### 3.2.1. MATERIALS WITH DIFFERENT THERMAL CONDUCTIVITIES

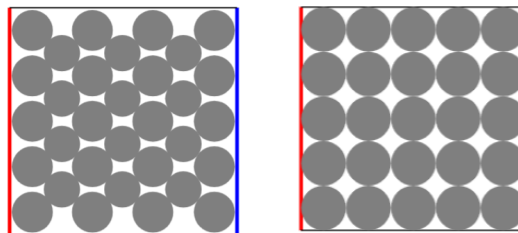
The effects of 4 different spherical materials on the heat transfer were tested in this study. The materials used were brass, steel, glass and polypropylene balls with diameters of 15.3 mm and were stacked in a BCT packing. In table 3.2 the used materials are listed with their conductivity ratios with respect to water and methanol. What can already be observed from table 3.2 is that there are roughly four orders of magnitudes of conductivity ratios, ranging from 0.32 to 618. Also it may be noted that the relative thermal conductivity in methanol is about 3 times higher for all four solid materials.

**Table 3.2** Materials with 4 different orders of magnitude thermal conductivities. Sphere size used:  $d=15.3$  mm arranged in a BCT stacking.

Sphere material	Conductivity ratio water $\frac{\lambda_{solid}}{\lambda_{water}}$	Conductivity ratio methanol $\frac{\lambda_{solid}}{\lambda_{methanol}}$
<b>Brass</b>	196	618
<b>Steel</b>	70.4	22.02
<b>Glass</b>	1.33	4.19
<b>Polypropylene</b>	0.32	1.00

### 3.2.2. DIFFERENT PACKING TYPES

In the second part of the heat transfer study, the effect of different packing types on the heat transfer were tested. The arrangements as tested in the heat transfer experiments were the Body Centered Tetragonal (BCT) packing, Simple Cubic Packing (SCP) and random packing (RP). A schematic side-view sketch of the BCT and SCP stacking in the cell is shown in figure 3.6.



**(a)** The BCT packing consists of 4 layers of a  $5 \times 5$  stacking and 3 layers of a  $4 \times 4$  stacking on top of each other.

**(b)** The SCP packing consists of 5 layers of  $5 \times 5$  stacking, giving a total of 125 stacked balls.

**Figure 3.6:** Side-view of the different packing types which were studied to see what the effect is on the heat transfer. The red wall represents the hot wall ( $T_H$ ), and the blue wall represents the cold wall ( $T_C$ ). Also the effect of a random packing on the heat transfer was studied in this part of the experiments. In the BCT configuration a total of 148 balls were used while in the SCP configuration 125 balls were used. In the random packing (which is not included in the figure) 122 balls were used.

The above listed packing types have different porosity's,  $\phi$ , which is defined as the total volume of the void space divided by the total volume of the cubical enclosure, (equation 3.8).

$$\begin{aligned}\phi &= \frac{\Delta V_{void}}{\Delta V_{cell}} \\ &= 1 - \frac{V_{spheres}}{V_{cell}}\end{aligned}\quad (3.8)$$

where  $V_{spheres}$  is the total volume occupied by the coarse-grained porous media and  $V_{cell}$  is the volume of the natural convection cell. The porosity thus defines the percentage of free space in the cell where the fluid can travel through. The used packing types and their corresponding porosity's are summarized below in table 3.3.

**Table 3.3** Summary of the number of balls and the corresponding porosities for the tested packing arrangements.

Packing type	Ball diameter [mm]	Number of balls	Porosity with respect to the cell dimensions
BCT	15.3	148	0.420
SCP	15.3	125	0.478
Random	15.3	122	0.489

### 3.2.3. MATERIALS WITH DIFFERENT SIZES

Also the effects of different sphere sizes on the heat transfer were studied in the side-heated natural convection cell. Two different sizes of solid glass spheres were tested which are summarized in table 3.4

**Table 3.4** Summary of the different sizes glass spheres including their diameter, number of balls and the corresponding porosity.

Size number	Ball diameter [mm]	Number of balls	Porosity
Size 1	5.00	4060	0.420
Size 2	15.3	122	0.487

For the 15.3 mm spheres, the balls were counted individually. For the 5.00 mm balls, the number of balls was estimated by comparing the total weight of the balls with the weight of one ball.

### 3.2.4. 3D PRINTED STRUCTURE

As an additional part of this study, also an experiment was conducted with coarse-grained porous media which did not cover the two vertical boundary layers but did cover the middle of the cell. This coarse-grained porous structure consisted of 100 balls ( $4 \times 5 \times 5$ ) and was stacked in a SCP geometry, as shown in figure 3.7. The structure was specially fabricated using a Seido Connex3 3D printer which printed the structure using a technique called stereolithography [41]. This technology is able to create 3D structures by laying down a UV-sensitive liquid epoxy-resin on a support material, called VeroBlack [42]. A UV laser beam then scans the surface of the layer of resin and selectively hardens the material corresponding to the sketch which was fed to the 3D printer. In this way, the structure can be built up layer by layer with a high accuracy. When the structure was printed, the leftover resin and support material was removed manually. In appendix D, the specifications of the 3D printer are given as well as the material properties of the stereo-lithographic ink.

The 3D printed structure consists of 4 layers of  $5 \times 5$  balls which are printed on top of each other. The distance between the hot (cooled) wall and the outer edge of the structure is  $\sigma \approx 7.9 \pm 0.5$ mm, as shown in figure 3.8.

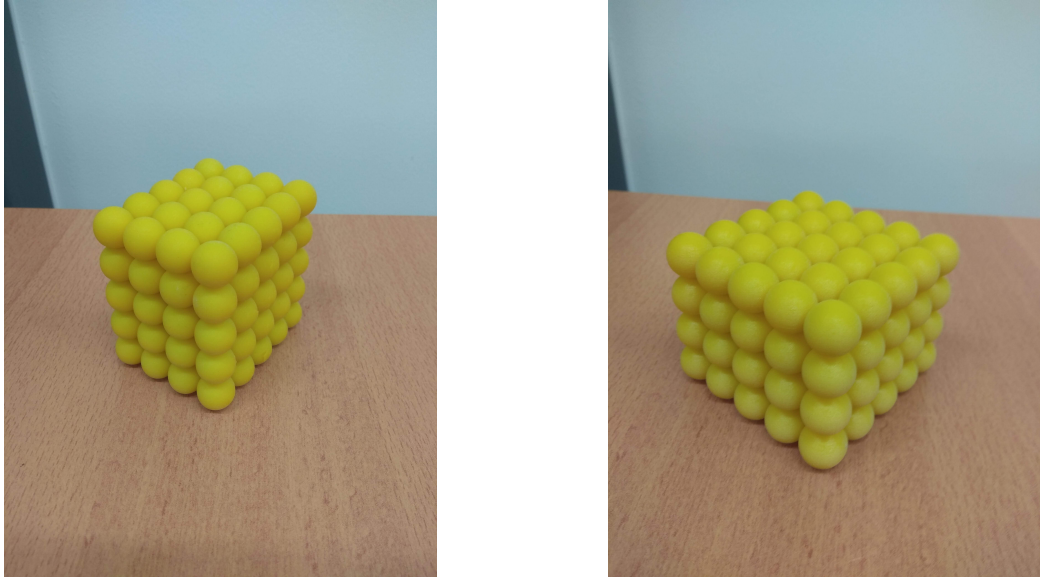


**Figure 3.7:** 3D-printed coarse-grained porous media structure in a SCP configuration. The material used to print this structure is a stereolithographic liquid which hardens in the presence of UV light.

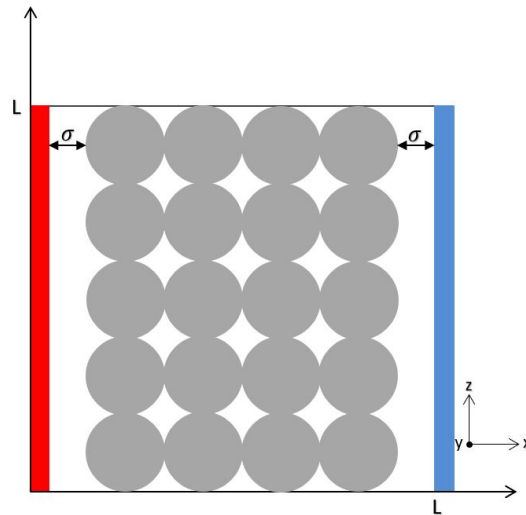


**Figure 3.8:** Front view of the 3D printed structure which is positioned inside the cubical enclosure. The red (blue) wall represents the heated (cooled) wall.

### 3.3. PARTICLE IMAGING VELOCIMETRY

The experimental setup for the PIV measurements includes the same cell as used for the heat transfer experiments (figure 3.2) but without polystyrene blocks on the side-walls in order to enable optical accessibility. A photo and a schematic overview (side- and top-view) of the PIV setup are given in figures 3.9 and 3.10 respectively. In this setup, a parallel green laser beam is diverged using a cylindrical lens. This diverged light sheet is then reflected by a single-reflecting mirror which is placed 74 cm from the cylindrical lens under an angle of approximately  $45^\circ$ . The light-sheet is then reflected on the cell which is placed underneath the mirror and in this way a planar cross-section of the flow is illuminated. The fluid flow was seeded using Polyamide tracer particles (Dantec Dynamics) with an approximate diameter of  $5\mu m$  which follow the flow. The illuminated tracer particles, which scatter the laser light, were then observed by a black/white CCD camera to visualize the flow in the cell and obtain 2D velocity fields.

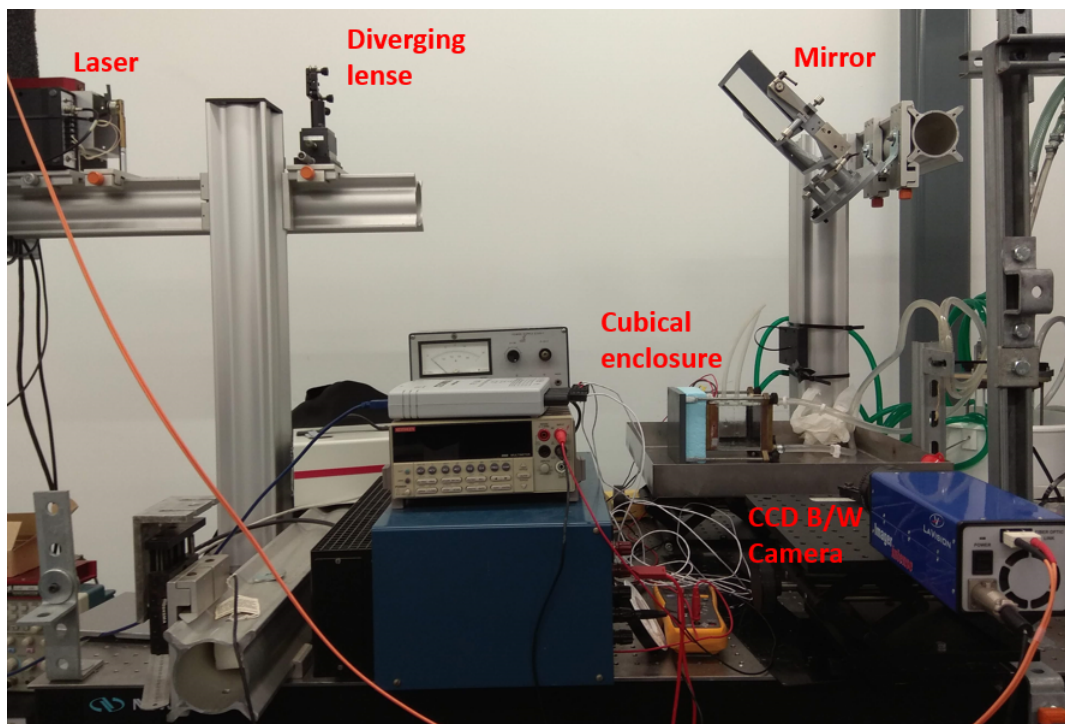
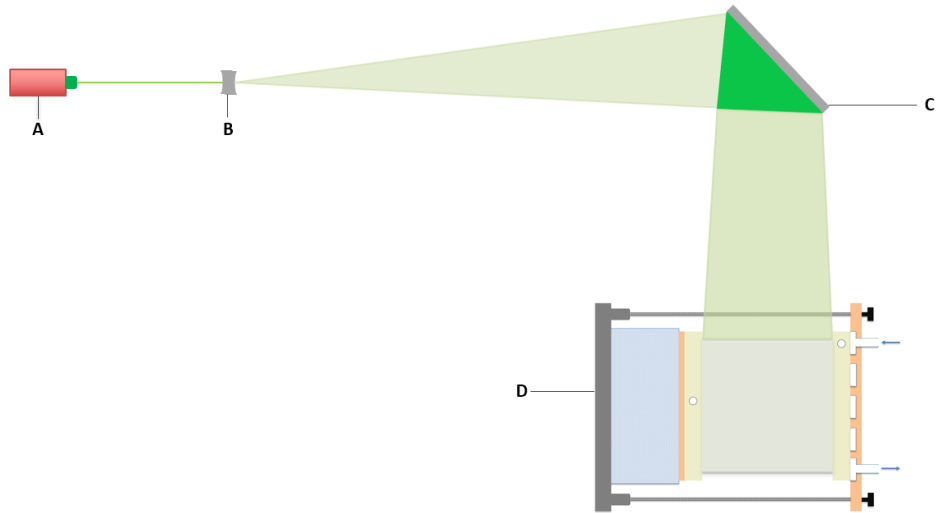
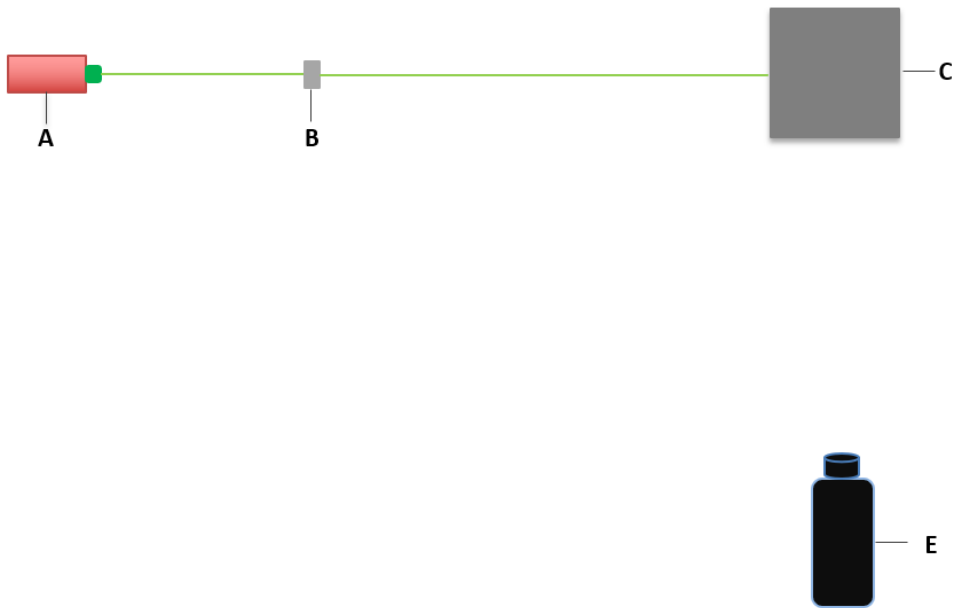


**Figure 3.9:** Photo of the experimental setup which was used to perform PIV measurements. The different parts of the cell are explained in figure 3.10.



(a) Side view of the PIV setup.



(b) Top view of the PIV setup.

**Figure 3.10:** a) and b) represent the side and top view of the PIV setup. A) Laser, B) cylindrical lens, C) mirror, D) side-heated convection cell, E) CCD black/white camera.

### 3.3.1. LASER

The laser which is used in the PIV experiments to illuminate a planar cross-section, is a diode-pumped solid state green laser (Pegasus) with a wavelength of  $\lambda = 532$  nm. The intensity is Gaussian distributed and the laser light-sheet thickness is approximately 2 mm. The laser is connected to a pulser and was set on a pulse separation time of 50 ms and a time difference of 1 second between each pair of images. The width of the laser pulses were set on 30 ms. A diverging light sheet is created by letting the laser beam pass through a cylindrical lens with a focal length of -3.9 mm.

### 3.3.2. CCD CAMERA

The CCD camera used for the PIV measurements, is a high-resolution double-frame black/white camera (LaVision Imager Intense) with a resolution of  $1376 \times 1040$  pixels. A 28 mm Nikon lens with an f-number of 2.8 was installed on the camera. The recordings have a magnification factor of  $M = 0.083$  and a resulting spatial resolution of about  $80 \mu\text{m}$  per pixel for the used convection cell. The raw PIV recordings, which were stored as images, were post-processed in Davis 7.2 (LaVision commercial software) where velocity vectors were calculated using a multi-pass cross-correlation with an interrogation window of  $48 \times 48$  and  $16 \times 16$  pixels, an overlap of 50% and a corresponding vector resolution of 0.64 mm.

### 3.3.3. HYDROGEL BALLS

Because PIV is an optical measurement technique where a light-source is used to visualize the flow in the cell, a different type of porous media is used. This is because the solid porous material as used in the heat transfer experiments, blocks the necessary laser light and only a small fraction of the flow can be visualized. Therefore, a material should be used that has almost the same refractive index as that of the fluid used, which is water in this study. The material used for these experiments as the coarse-grained porous media is hydrogel which is a hydrophilic polymer that is able to absorb more than 200 times of its own weight in water. These hydrogel balls have a diameter of  $\approx 15$  mm and a refractive index very close to that of surrounding demi-water ( $\approx 0.1\%$ ). [21] This refractive index matching property of the hydrogel balls make the material suitable to be used as a porous media for the PIV experiments.[43] In figure 3.11, a photo is presented of how the hydrogel ball looks like.

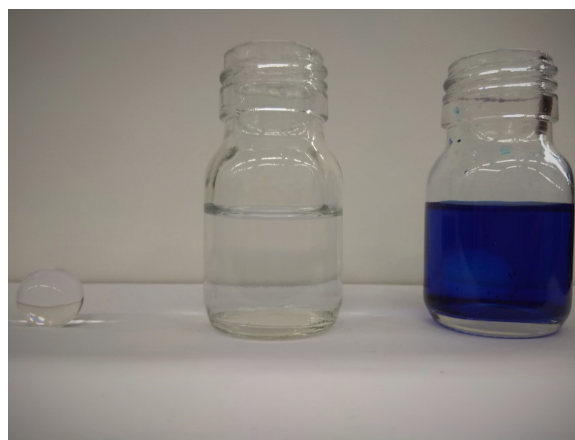
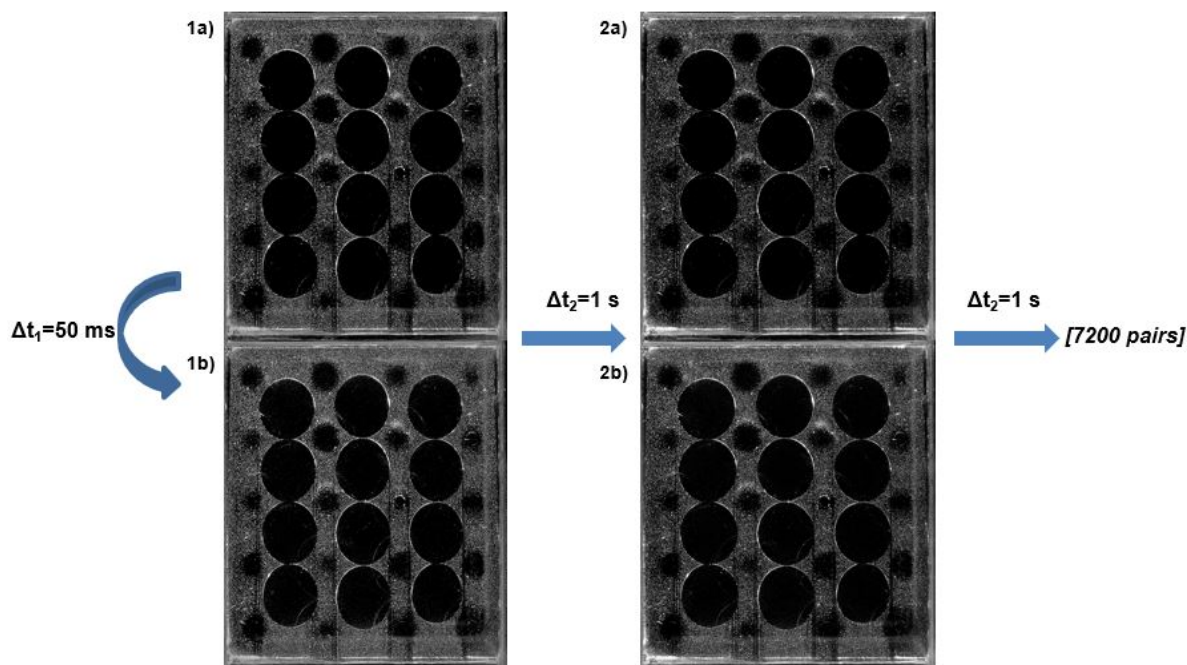


**Figure 3.11:** Hydrogel balls with refractive index matching with demi-water. From left to right: hydrogel ball, hydrogel ball immersed in water and hydrogel ball immersed in blue-dyed water.

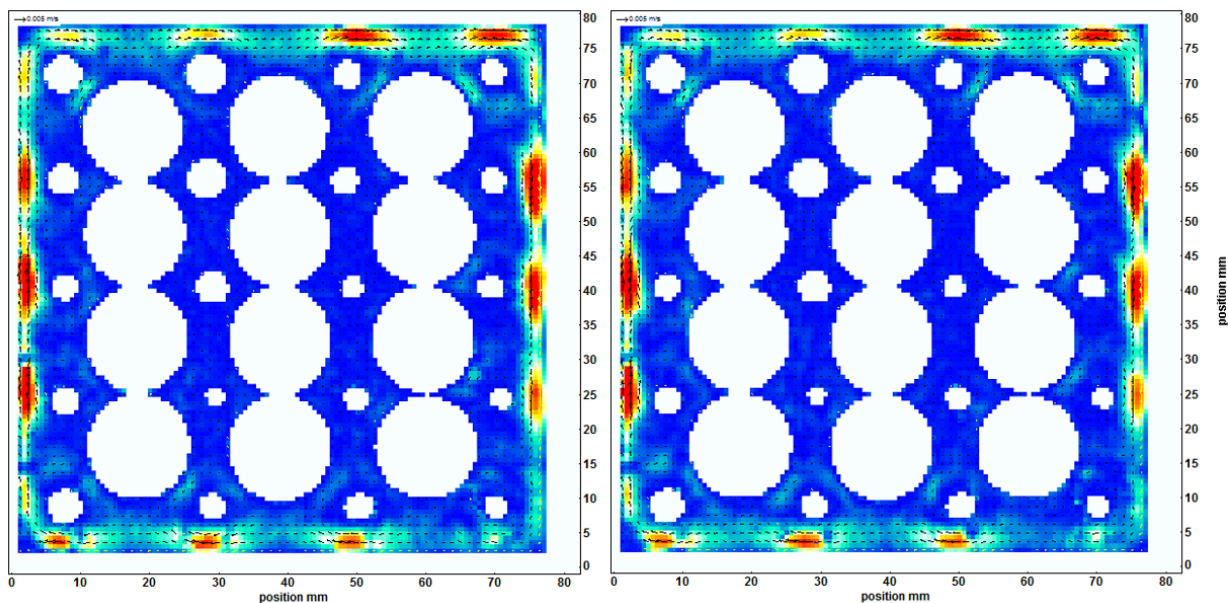
### 3.3.4. MEASUREMENT PROCEDURE

The measurement procedure for the PIV experiments consisted of preparing the cell, positioning the cell, performing the measurement and post-processing the images in Davis 7.2 to obtain the velocity vectors. The cell was filled with hydrogel balls in the desired stacking (BCT or random) and degassed demi-water together with some seeding tracer particles were added. Following, the heating plate was warmed and the cooling plate was cooled to let the heat transfer take place at the desired temperatures. The cell was positioned under the mirror in such a way that the laser light-sheet was located at  $y/L = 0.4$ . When a steady-state was reached, the laser was turned on to illuminate the cell and the camera was focused on the cell and a measurement was started.

In figure 3.12 an overview of the PIV vector calculation is given. A pair of images, 1a) and 1b), was taken by firing two consequent laser pulses on the cell with a time-difference,  $\Delta t_1 = 50$  ms. A time-span,  $\Delta t_2 = 1$  s later, another pair of images were taken. This process continued for a total time of 2 hours which means a total of 7200 pairs of images were taken for each PIV-experiment. A 2D velocity field was calculated by each pair of images using the DAVIS software and the average of all of the velocity fields was finally taken, as will be further discussed in the results section 4.2.



(a)



(b)

**Figure 3.12:** Example of a PIV measurement where the hydrogel balls are stacked in a BCT packing in the side-heated cell. (a) Represents the raw PIV images, while (b) represents the post-processed velocity fields obtained from each pairs of images in DAVIS.

### 3.4. LIQUID CRYSTAL THERMOGRAPHY

The Liquid Crystal Thermography experiments are qualitative measurements to visualize the instantaneous temperature profiles inside a heat transfer system. Later the qualitative results were quantified using the same measurement technique. A photo of the experimental setup is shown in figure 3.13 and a schematic sketch with all the different parts is shown in figure 3.14 where the main components consist of a (white) line-light, a cylindrical lens and a color camera. The procedure for the LCT experiments was very similar as that for the PIV experiments. The convection cell was filled with hydrogel spheres and de-gassed water was added. The heating and cooling plate were then turned on and it took about one hour for the flow to obtain a steady-state. A suspension of liquid crystals in water was then added to the steady-state convection cell. By illuminating a plane in the cell using the white line-light, different colors were made visible which gave a qualitative measure for the temperature distribution in the cell.

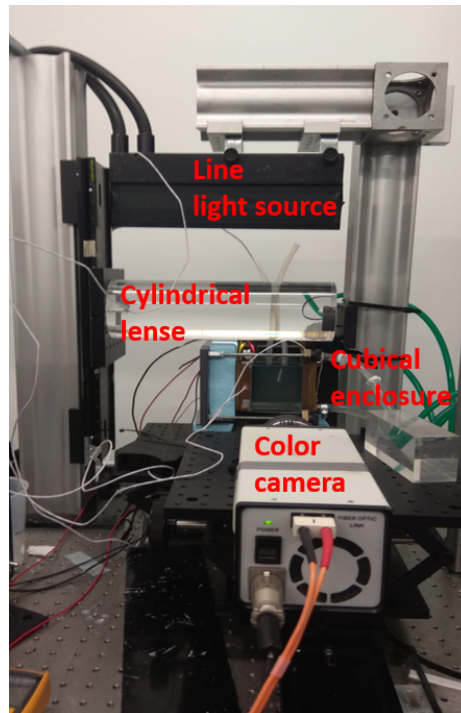
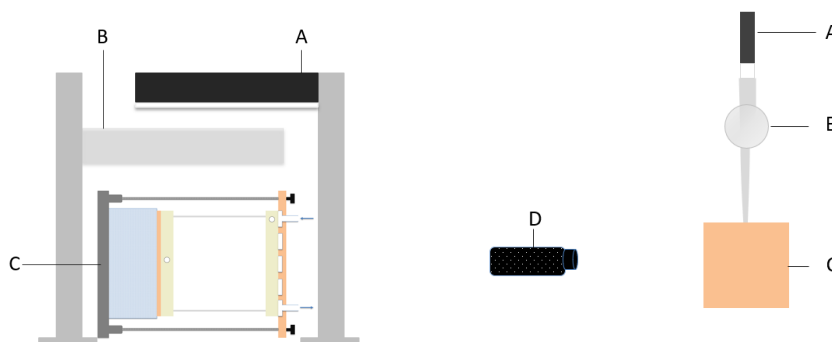


**Figure 3.13:** Photo of the LCT setup which was used to perform the LCT experiments. The different parts of the cell are explained in figure 3.14.



(a) Side view of the experimental LCT setup

(b) Side view of the experimental setup (perpendicular view with respect to figure (a))

**Figure 3.14:** Different viewing angles of the LCT setup. The main components as shown in the figure are: A) white line-light, B) cylindrical lens ( $\varnothing$  90 mm), C) side-heated natural convection cell, D) color camera.

### 3.4.1. MAIN COMPONENTS

To create the white line-light, two different light-sources were used. The light of a halogen lamp (type: Schott-Fostec, LLC [44]) and a LED lamp (type: Waldmann MCXFL3S [45]) were transferred through fiber optic cables to the line-light (type: Schott-Fostec A08912). The resulting diverging white line-sheet then passed through a cylindrical lens ( $\varnothing$  90mm) which created a uniform parallel light-sheet with a thickness of approximately 2mm inside the natural convection cell. A PCO Sensicam color camera with a resolution of  $1280 \times 1024$  was placed in front of the convection cell and was used to record images of the colorized temperature distribution.

### 3.4.2. LIQUID CRYSTAL SLURRY

Micro-encapsulated liquid crystals with an average diameter of 10-15  $\mu m$  (Hallcrest R25C60W) were used as tracer particles in the LCT experiments. 0.5 ml of the liquid crystal slurry was added to 400 ml water and was stirred constantly using a magnetic stirrer. When a steady-state heat transfer was obtained in the convection cell, 30 ml of the liquid crystal suspension was added to the cell and the recording was started.

### 3.4.3. QUALITATIVE TEMPERATURE COLOR DEFINITIONS

In the LCT-technique, the different colors give an indication on where the warm and cold fluid are and how they are distributed in the cell. The temperature of the heated (cooled) wall were set to  $T_h = 30.2^\circ C$  ( $T_c = 21.0^\circ C$ ). From the LCT experiments it was found that the colder region fluid was divided into the color green, yellow and red while the warmer region fluid was colored blue.

The different colors which were visible by shining the white line light on the cell containing the liquid crystals, give an indication on how the temperature is distributed throughout the cell. In table 3.5 the definitions of the different observed colors are given as used in the LCT measurements in this report.

**Table 3.5** Definition of the observed colors in the LCT experiments

Color	Definition
Blue	Warm fluid
Green	Transition region between warm/cold fluid
Yellow	Cold fluid
Red	Coldest fluid

### 3.4.4. QUANTITATIVE TEMPERATURE COLOR DEFINITIONS

Besides a qualitative LCT experiment, also a quantitative LCT experiment was performed as part of this thesis to quantify each temperature with its observed colors. In order to achieve a quantitative result based on the qualitative images, a so-called *temperature-Hue* calibration had to be performed. The choice was made to do the T-Hue calibration in the same way as described by *Ataei-Dadavi* [21] where the Rayleigh-Bénard configuration was under investigation.

The quantification experiment was performed by putting de-gassed water along with liquid crystals in the side-heated cubical enclosure and imposing the same constant temperature on both the left and right walls. A stirrer was then used to maintain a constant temperature throughout the pure-fluid cavity and the local temperature was then monitored with a PT-100 thermometer which was placed inside the cubical enclosure. The temperatures where the calibration was carried out with ranged from  $19.5^\circ C$  up to  $30.2^\circ C$ . At each temperature run, a set of images were taken and the Hue-values were calculated using the algorithm as proposed by *Smith* [46]. This algorithm is able to convert the recorded RGB (Red-Green-Blue) images to the HSV (Hue-Saturation-Value) color space. The Hue-values were then extracted and a temperature-Hue plot was created, as presented in figure 3.15, where it was found that a fifth order polynomial equation (equation 3.9) fits the experimental data points the best with 95% confidence bounds, where the coefficients are presented in table 3.6. The obtained polynomial fit is in agreement with the review on liquid crystal calibration methods which was presented by *Dabiri* [47]. In his work, it is mentioned that for the useful temperature range, best fit polynomials have been used in an extensive range of publications to curve-fit the experimental calibration data.

From the LCT calibration experiment it was found that the effective temperature range for the LCT experiments used in the side-heated configuration to range from  $21.0^\circ C$  to  $30.2^\circ C$ , resulting in a temperature difference,  $\Delta T = 9.2^\circ C$ . The corresponding Rayleigh number (using equation 2.6) is then  $Ra = 8.2 \times 10^7$ . The uncertainty of the used liquid crystals was calculated to be  $\pm 0.5^\circ C$ .

$$T(Hue) = p_1 \times Hue^5 + p_2 \times Hue^4 + p_3 \times Hue^3 + p_4 \times Hue^2 + p_5 \times Hue + p_6 \quad (3.9)$$

**Table 3.6** Coefficients for the fifth order polynomial fit which was found to be the best fit for the experimental data points in the temperature-Hue plot. The values of the coefficients can be filled in into equation 3.9 and lie within a confidence bounded-region of 95%.

Coefficient	Value
p <sub>1</sub>	3744
p <sub>2</sub>	-6832
p <sub>3</sub>	4698
p <sub>4</sub>	-1515
p <sub>5</sub>	232.8
p <sub>6</sub>	9.897

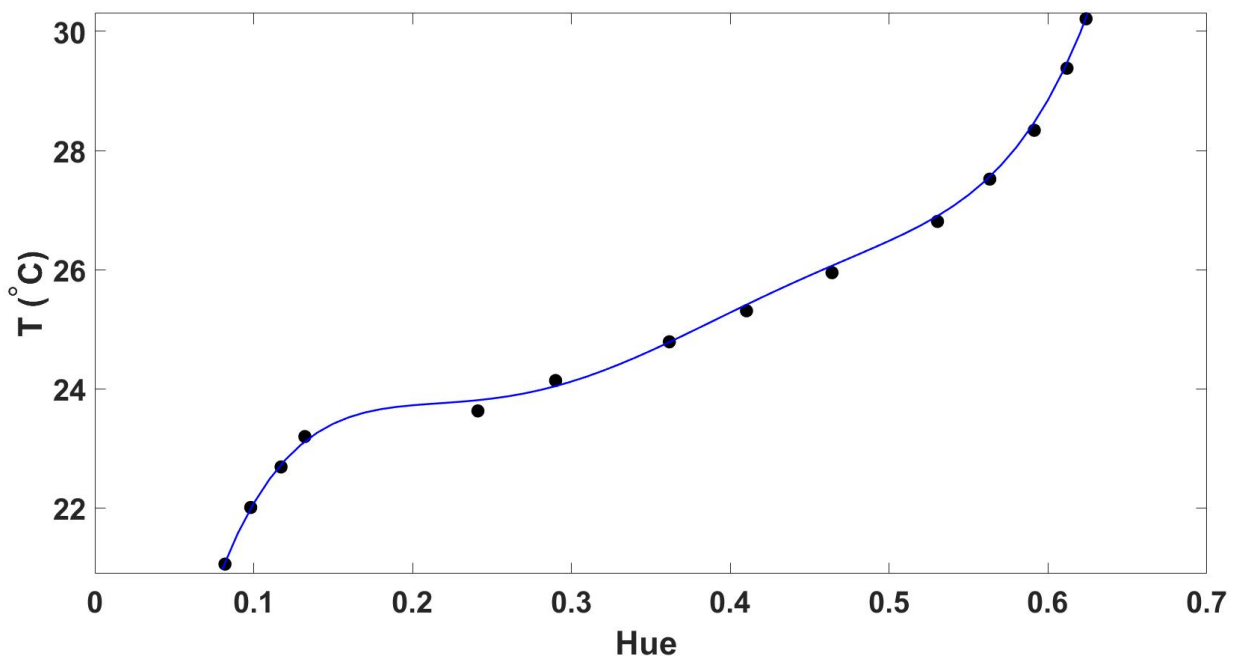


**Figure 3.15:** Temperature-Hue plot for the temperature calibration experiment in a side-heated cubical enclosure for the used liquid crystals. The experimental data-points are shown as circles and the black line is the corresponding fifth order polynomial fit, where the coefficient values are specified in table 3.6 and can be filled in into equation 3.9.



# 4

## RESULTS

In this chapter the results are shown as measured in all three types of experiments. In the first subsection, the results of the heat transfer experiments are presented in the form of Nu–Ra graphs and are discussed properly. In the second subsection, the results of the PIV experiments are shown graphically in the form of 2D velocity fields for both the empty enclosure and the hydrogel filled enclosure at two different Ra-numbers. These plots are included to make decent comparisons between the filled cell and the non-filled cell. Finally, at the end of this chapter the qualitative results of the effect of coarse-grained porous media on the temperature distribution inside the side-heated cubical enclosure are given.

### 4.1. HEAT TRANSFER MEASUREMENTS

The effects of different conductivity of the spheres, different packing types and different size of spheres are investigated in this part of the study. The heat transfer results of the different configurations of coarse-grained porous media, are compared to the heat transfer in the empty cavity which serves as a reference curve. By empty cavity we mean the cavity filled with only the working fluid, but without coarse-grained porous media.

In figure 4.1 on the next page, the heat transfer results of the pure-fluid enclosure and the enclosure filled with polypropylene balls in a BCT stacking with their corresponding error-bars are presented. In the graph, the closed and open markers represent the experiments performed in water and methanol, respectively. In this section, the experiments performed in water are referred to as the lower Ra-regime ( $1.6 \times 10^7 < Ra < 2.4 \times 10^8$ ) while the experiments performed in methanol are referred to as the higher Ra-regime ( $1.5 \times 10^8 < Ra < 1.9 \times 10^9$ ).

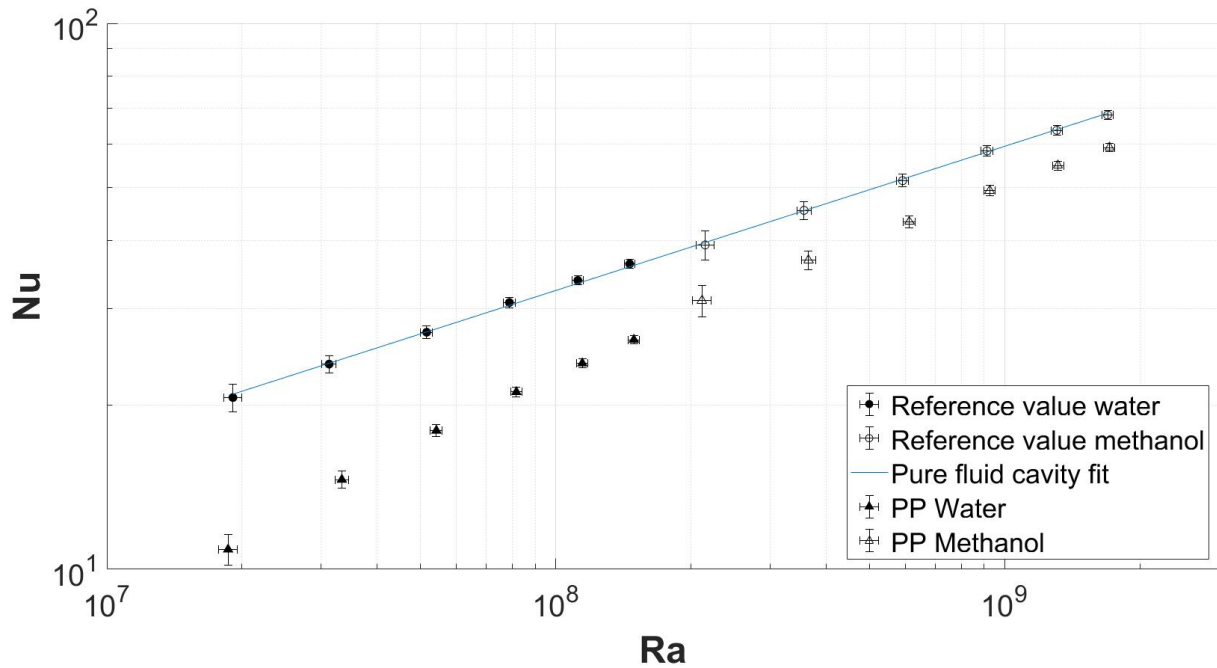


**Figure 4.1:** Nu-Ra graph of the heat transfer in the cavity filled with only water or methanol (no spheres present) and in the cavity filled with BCT packing of polypropylene spheres. The corresponding error-bars in both vertical and horizontal directions are included for both heat transfer data. The empty cavity fit is shown in the legend as the 'SHNC fit' which stands for 'Side-Heated Natural Convection fit'.

From the experiments performed in the pure fluid cell, it was found that the best fit to the data is the power-law relation:  $Nu = 0.250 \times Ra^{0.264}$  which is in good agreement with the numerical simulations as presented by the articles which are summarized in table 4.1. The obtained exponent from this experimental study lies within a range of  $\pm 1.1\%$  with respect to the literature values. The obtained power-law relation is presented as a solid, blue line in figure 4.1 and serves as a reference in the remainder of this study.

**Table 4.1** Reference values found in literature for the Nu-Ra relationship in a side-heated empty cavity. The coefficients can be filled in, in the power-relation between Nu and Ra:  $Nu = a \times Ra^b$ .

Reference	Coefficient	Values	Method
<i>Lankhorst</i> [1]	a	0.236	Finite Difference Method (SIMPLE algorithm)
	b	0.265	
<i>de Geus</i> [48]	a	0.241	DNS simulation
	b	0.266	
<i>Tric et al.</i> [49]	a	0.221	Simulation in air (Ch. p-d model) <sup>1</sup>
	b	0.267	

From the experimental data points for the polypropylene (PP) balls, it can be observed that the heat transfer is indeed reduced. The main observation is that in the lower Ra-regime ( $1.9 \times 10^7 < Ra < 1.5 \times 10^8$ ), the heat transfer is reduced more than in the higher Ra-regime ( $2.1 \times 10^8 < Ra < 1.7 \times 10^9$ ). A possible explanation for this observation might be that at higher Ra-numbers, thinner boundary layers are present and that the convective flow can move more freely near the periphery of the enclosure. The direct result of this is that natural convection occurs at a higher rate and that the porous media data points approach the asymptotic value.

<sup>1</sup>Ch. p-d model stands for: Chebyshev projection-diffusion model and is explained thoroughly by *Tric* in [49]

#### 4.1.1. EFFECT OF SPHERE CONDUCTIVITY ON NATURAL CONVECTION HEAT TRANSFER

Experiments were carried out to explore the effects of spheres with different conductivity on natural convection heat transfer in the side-heated enclosure. Four different materials were tested, as presented in section 3.2.1, to gain insight into the effects of the different conductivity's on the overall heat transfer. The spheres were stacked in a BCT packing in the enclosure and each sphere has a diameter of  $\varnothing = 15.3\text{mm}$ .

In figure 4.2, the results are presented and compared to the empty cavity convective heat transfer. What immediately draws the attention, is the increase in the heat transfer for the steel and brass sphere results with respect to the empty enclosure fit. This increase can be attributed to the fact that both materials have a high conductive behaviour which can be characterized by the ratio between the thermal conductivity of the different materials and the thermal conductivity of the working fluid. This is also referred to as the conductivity ratio between the solid spheres and the working fluids. This high conductivity ratio for the brass and steel spheres is the reason that the heat transfer is higher than the heat transfer inside the pure-fluid enclosure.

A small jump is observed between the last point of the water experiment and the first point of the methanol experiment. This is due to the fact that the conductivity ratio of steel and brass in methanol is much higher than those in water. Therefore, the heat transfer is higher for both materials in methanol than in water.

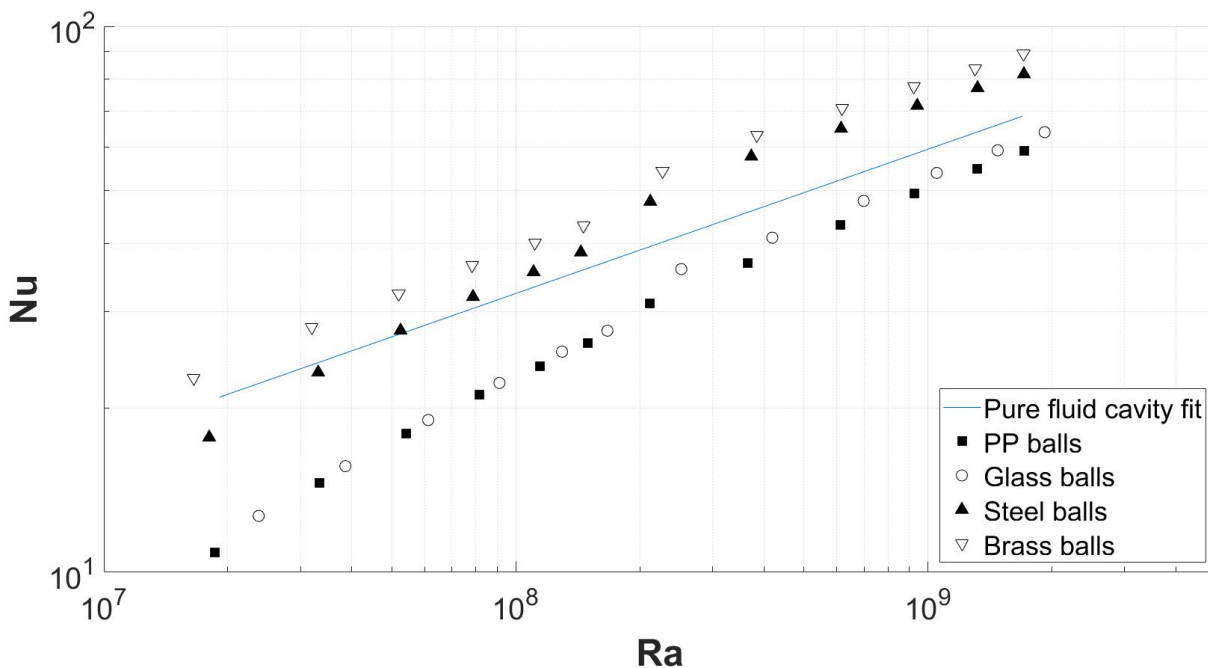


**Figure 4.2:** Effect of conductivity: Heat transfer data for different material of spheres. The spheres ( $\varnothing = 15.3\text{mm}$ ) are stacked in a BCT configuration.<sup>2</sup>

In the case of glass and polypropylene spheres, the heat transfer is reduced significantly in the low Ra-regime ( $1.8 \times 10^7 < Ra < 1.7 \times 10^8$ ), while in the higher Ra-regime ( $2.0 \times 10^8 < Ra < 1.9 \times 10^9$ ) the heat transfer comes very near the asymptotic pure-fluid cavity fit when the Ra-number increases. Also for the glass spheres a small jump can be observed between the last point of the water experiment and the first point of the methanol experiment which can also be assigned to the difference in conductivity ratios. This jump for polypropylene spheres is much smaller with respect to the other three materials, since the conductivity ratio in methanol is again higher than in water but both conductivity ratios are still very low.

<sup>2</sup>In this and the four upcoming figures, the experimental data points obtained from both water and methanol experiments have the same open or closed marker for visualization purposes.

#### 4.1.2. EFFECT OF PACKING TYPE ON NATURAL CONVECTION HEAT TRANSFER

In this part of the study, experiments were carried out to examine the effects of different packing types on natural convection heat transfer in the side-heated enclosure. Three different packing types are tested, as discussed in section 3.2.1, to gain insight into the effects of the different packing configurations on the overall heat transfer. The packing types considered are BCT, SCP and random packing and are tested using  $\varnothing = 15.3\text{mm}$  glass balls.

In the figure below (figure 4.3) the results are presented for the different packing types. The figure shows that, again in the lower Ra-regime ( $1.9 \times 10^7 < Ra < 1.7 \times 10^8$ ) the heat transfer is reduced substantially and the heat transfer results of the different packing types are observed to come closer to each other at higher Ra-numbers. In the high Ra-regime ( $2.0 \times 10^8 < Ra < 1.9 \times 10^9$ ) the heat transfer results of all three packing types are converging and are relatively very close to the empty cavity fit.

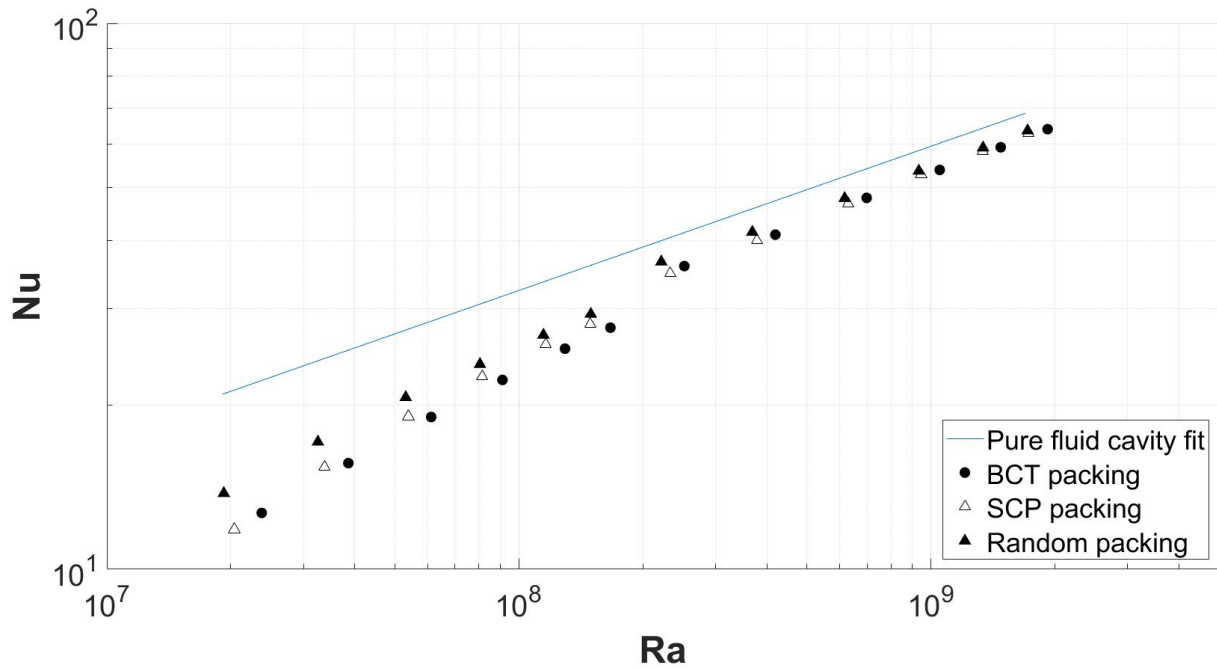


**Figure 4.3:** Effect of different packing type: Heat transfer data for different packing types. The glass balls ( $\varnothing = 15.3\text{mm}$ ) are stacked in a BCT, SCP and random configuration.

It can be observed from the above figure that in especially the lower Ra-regime, the heat transfer is reduced more in the BCT and SCP packing with respect to the random packing. This phenomenon may be assigned to the fact that in the BCT and SCP packing both heated and cooled walls are covered by a dense layer of  $5 \times 5$  glass spheres. However, in the random packing, the spheres are thrown in randomly and during the experiments it was observed that the solid boundaries were not covered fully by a  $5 \times 5$  layer of glass balls. The heated and cooled walls are thus more densely covered in the BCT and SCP configuration than in the random packing.

### 4.1.3. EFFECT OF SPHERES SIZE ON NATURAL CONVECTION

The effect of two different sized spheres on the heat transfer has also been studied. Glass spheres with two different sizes were randomly packed in the enclosure to see how the heat transfer in the cell was affected. In figure 4.4 the heat transfer results are plotted. The diameters of the two different types of glass spheres used were 5.00 mm and 15.3 mm.

From the graph it is clear that when the size of the spheres is smaller, the heat transfer is reduced more significantly. In the lower Ra-regime ( $1.9 \times 10^7 < Ra < 1.5 \times 10^8$ ), the 15.3 mm spheres have a substantial effect on the heat transfer, but in the high Ra-regime ( $2.1 \times 10^8 < Ra < 1.8 \times 10^9$ ) the heat transfer almost lines up with the empty enclosure fit. The 5.00 mm spheres however, start approaching the empty cavity fit at much higher Ra-numbers. This difference for all two sized balls shows that the heat transfer is related to the size of the spheres.

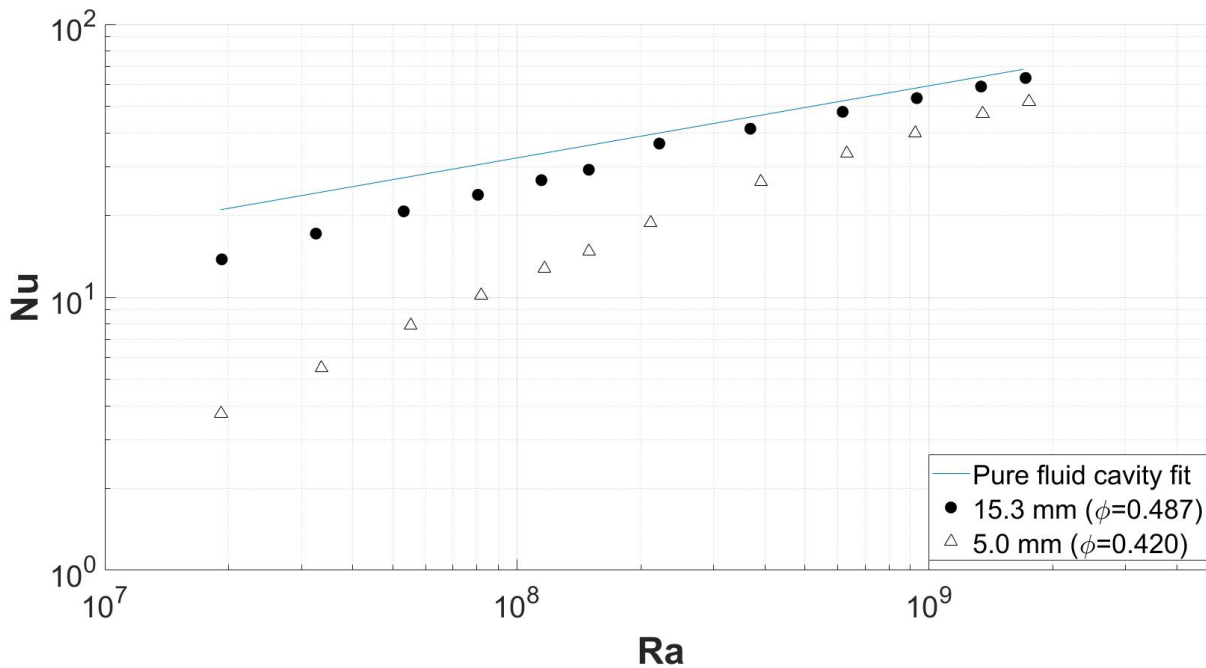


**Figure 4.4:** Effect of sphere size: Heat transfer data for two different sizes of spheres. The glass balls ( $\varnothing \approx 5.0\text{mm}$  and  $\varnothing = 15.3\text{mm}$ ) are stacked in a random configuration.

The reason for the reduced heat transfer when the sphere size is smaller but the porosity is not merely different, is that the smaller sized spheres cover the heating and cooling plate more densely. Since natural convection in a side-heated enclosure is boundary-driven (as explained in section 1.1), the heat transfer is mainly determined by the void space near the solid boundaries. In the cavity filled with the 5.00 mm sized spheres for instance, the left and right walls are much more densely covered than in the 15.3 mm case.

#### 4.1.4. NON-COVERED BOUNDARY LAYERS

In figure 4.5, the heat transfer results are presented for the 3D-printed structure, as introduced in subsection 3.2.4. The configuration of this structure is a SCP type of packing and was positioned in the middle of the enclosure such that the four glass walls were covered but the heated and cooled walls were not covered. The conductivity ratio for the material of which the 3D-structure is composed of, can be compared to the conductivity ratio of polypropylene in both water and methanol.

From the graph it can be observed that in the lower Ra-regime ( $1.0 \times 10^7 < Ra < 1.5 \times 10^8$ ), the heat transfer is reduced slightly but becomes more aligned with the empty cavity fit when Ra increases. Especially in the higher Ra-regime ( $2.1 \times 10^8 < Ra < 1.7 \times 10^9$ ), the experimentally obtained data-points for this configuration are perfectly aligned with the empty cavity fit and show a smooth overlap. In this high Ra-regime, the present coarse-grained porous media does not affect the heat transfer very much.

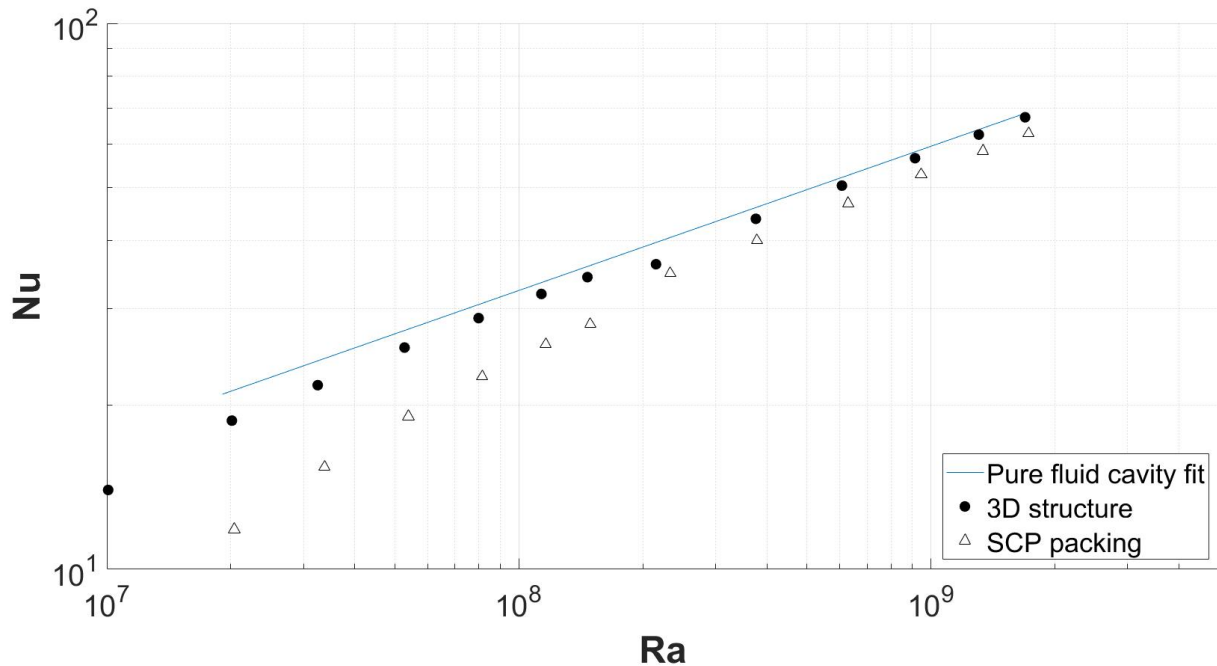


**Figure 4.5:** Result of the heat transfer experiments performed with the 3D structure which was placed in the middle of the cell. In the graph also the SCP ( $5 \times 5 \times 5$ ) packing is included. The configuration of the balls is  $4 \times 5 \times 5$  and the distance,  $\sigma$ , between the structure and the heated and cooled walls is  $\sigma \approx 7.9$ mm.

The figure shows that in the presence of the 3D-structure, the heat transfer is reduced slightly in the lower Ra-regime. In the higher Ra-regime, the heat transfer is reduced even less and an asymptotic value onset is observed at  $Ra = 1.3 \times 10^9$ . When compared to the SCP ( $5 \times 5 \times 5$ ) packing, it is clear that the heat transfer is enhanced in the presence of the 3D-structure and natural convective heat transfer actually reaches the asymptotic value of the empty cavity fit. From this study it is unclear what the heat transfer of the  $5 \times 5 \times 5$  packing will behave at higher Ra-numbers and if it also will reach the asymptotic value. This can be a suggestion for further research and will be discussed more briefly in the recommendations section 6.

What can further be noticed from figure 4.5 is a small jump downward between the last data point in water and the first data point in methanol. When including the error-bars, as presented and discussed in appendix E.1, the cause of the small jump can be assigned to the measurement error of the heat transfer measurement.

## 4.2. NATURAL CONVECTION FLOW DYNAMICS

In order to understand the physics of natural convective flows in coarse-grained porous media and to gain more knowledge on the mechanisms which influence the convective heat transfer, planar velocity fields were measured at two different Ra-numbers. In this section the results of the PIV measurements are presented and discussed. The mean velocity values were determined by taking 7200 double-snapshots which were obtained at a rate of 1 Hz. Details on the experimental setup and measurement procedure are given in section 3.3. The output of the results are normalized 2D velocity vectors and are based on the averaged values  $\bar{v}_x$  and  $\bar{v}_z$ , as defined by:

$$\bar{v}_x = \frac{1}{N} \sum_{i=1}^N v_{x,i} \quad (4.1)$$

$$\bar{v}_z = \frac{1}{N} \sum_{i=1}^N v_{z,i} \quad (4.2)$$

The experiments were performed at  $Ra = 7.9 \times 10^6$  (low Ra) and at  $Ra = 1.5 \times 10^8$  (high Ra). Initially, the flow pattern inside the water-filled cubic enclosure was obtained for both Ra-numbers to serve as a reference. Next to that a packed bed of hydrogel balls were ordered in a BCT configuration in the cubic enclosure which served as the coarse-grained porous medium. The combination of water and hydrogel spheres form a completely transparent solid-liquid couple and enables the use of PIV to study the natural convection flow around the coarse-grained porous media. Finally, the results of the filled and the non-filled enclosures were then compared to each other.

To be able to compare the flow patterns for the low and the high Rayleigh numbers cases, a scaling normalization factor is introduced. In this way, the fluid motion can be visualized and studied independently of the maximum velocities,  $v_{max}$ . The scaling factor used in this study to normalize both  $v_x$  and  $v_z$  is given by:

$$v_{norm} = \frac{\alpha}{L} Ra^{\frac{1}{2}} \quad (4.3)$$

This normalization factor was firstly introduced by *Patterson et al.* [50] in their numerical study of natural convection in a differentially heated cubic enclosure. The above mentioned normalization factor was also used in the experimental work as performed by *Ivey* [51], where transient natural convection was studied in a side-heated configuration.

In the contour-plots in the section below, the planar velocity fields are presented as black arrows which represent the velocity vectors and are overlaid on a coloured map which shows the magnitude of the local velocity. The normalized scalar velocity magnitudes are calculated by:  $|\bar{v}| = \sqrt{(\bar{v}_x^*)^2 + (\bar{v}_y^*)^2}$ .

### 4.2.1. VELOCITY FIELDS

In figure 4.6 on the next page, a plot of the normalized velocity field due to natural convection flow inside the empty cubic enclosure is given for both the low and the high Ra-numbers. As shown in the figure, the flow at both Ra-numbers is clearly boundary driven where the bulk of the fluid motion is occurring near the periphery of the cubic enclosure. Near the bottom and top boundaries the flow is confined to a wider distribution which is observed by the contrasts in the blue color. In the middle of the cell however, there is a relatively small fluid flow and the magnitude of the velocity components are almost negligible with respect to the flow near the boundaries of the cavity. The overall velocity fields for both the low and the high Ra-numbers show good agreement with the streamlines as presented by *Lankhorst et al.* [1] in his PhD-dissertation, as shown in figure 4.7 on the next page.

It can also be observed from the flow at both Ra-numbers that the layer where the bulk of the fluid motion is occurring near the hot and cold wall gets thinner when the Ra-number grows, which is in line with previous studies. The reason that the boundary layer at the high Ra-number is thinner is that the buoyant force dominates over the viscous force which results into a less suppressed flow by viscous forces. The other interesting feature is that the normalized planar velocities at the low Ra-number are higher at the cold wall than at the warm wall, while the velocities are more uniformly distributed between the heated and cooled wall at the high Ra-number.

As described in the literature, the present findings confirm that the flow in a side-heated configuration is mainly boundary driven in a circular motion, as discussed in section 2.2. The highest velocity magnitudes are observed near the heated and cooled walls, while a relatively smaller velocity magnitude is observed near the top and bottom wall.

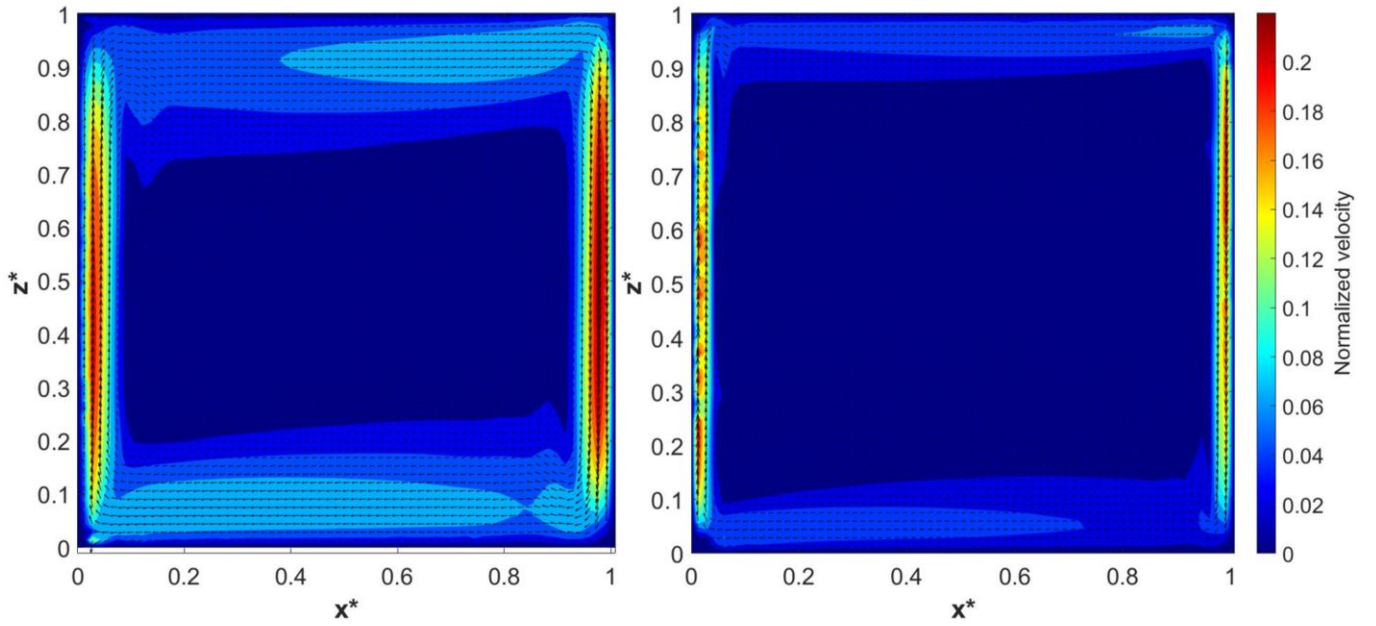


**Figure 4.6:** Normalized velocity fields of natural convective flow in the empty cell at  $Ra = 7.9 \times 10^6$  (left) and  $Ra = 1.5 \times 10^8$  (right). The left wall is heated while the right wall is cooled. Measurements performed at  $y/L = 0.4$ .<sup>3</sup>

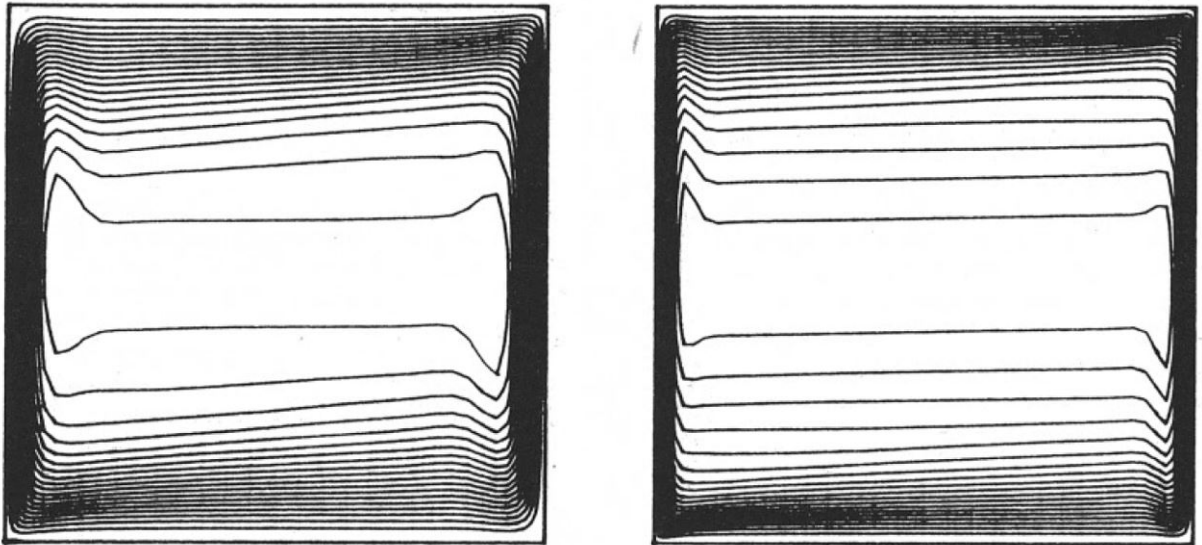


**Figure 4.7:** Streamlines as presented in the PhD-dissertation of *Lankhorst* [1] on side-heated laminar and turbulent natural convection in water. The left figure is at  $Ra = 10^7$  and the right figure is at  $Ra = 10^8$ . Both figures are copied with from page 104. Figures 5.19 a) and b) from the PhD dissertation of *Lankhorst*. Permission to use these figures were granted from the author.

<sup>3</sup>In this and upcoming velocity plots,  $x^*$  and  $z^*$  are respectively the normalized length and width of the cubical enclosure

In figure 4.8, the effect of the packed bed of hydrogel balls on the natural convection flow inside the cubic enclosure at low Ra-number is compared to the pure fluid cell. The bulk of the flow is still near the side-walls but in the presence of the media, the flow is more evenly distributed between the four solid boundaries. Near the top and bottom solid boundaries higher flow velocities are observed than in the pure fluid cell. In these regions, the highest velocity magnitudes are divided into local spots between the balls near the boundaries. In the void spaces between the hydrogel balls, almost no flow occurs except for a few spots near the utmost left and right balls.

What can also be observed similar to the pure fluid cell, is that the flow moves down more rapidly near the cold (right) wall than rises at the heated (left) wall. This makes the flow not symmetrical in the z-plane. In the x-plane however, the visualized heat flow is observed to be nearly symmetrical.

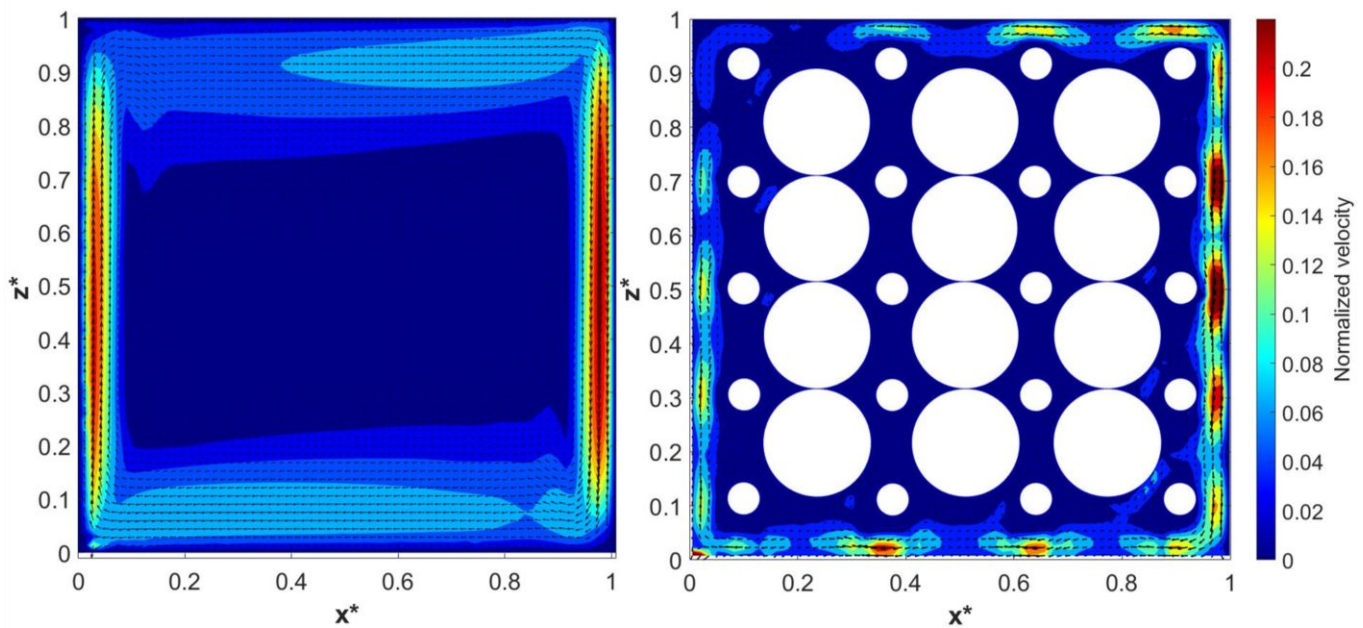


**Figure 4.8:** Normalized velocity fields of natural convection flow at  $Ra = 7.9 \times 10^6$  in the pure fluid cell (left) and in the BCT stacked cell (right). Measurements performed at  $y/L = 0.4$ .

In figure 4.9, the effect of the packed bed of hydrogel balls on the natural convection flow inside the cubic enclosure at high Ra-number is presented. While in the pure fluid cell the bulk of the fluid motion, as well as the highest normalized velocity magnitudes occur in a very thin region near the heated and cooled walls, in the hydrogel packed configuration the fluid flows with high velocities near all four solid boundaries. It is again divided into local spots where the flow velocity is higher with respect to its surroundings. Unlike the obtained result at the low Ra-number, at the high Ra-number the visualized flow is almost perfectly symmetrical in all directions. The high velocity spots near the heated and cooled wall are almost identical.

Identical to low Ra-number, there is hardly any flow in the void space between the hydrogel spheres. Again, some flow is observed at the utmost left and right vertical row of the present balls, but their velocity magnitudes remain relatively small.

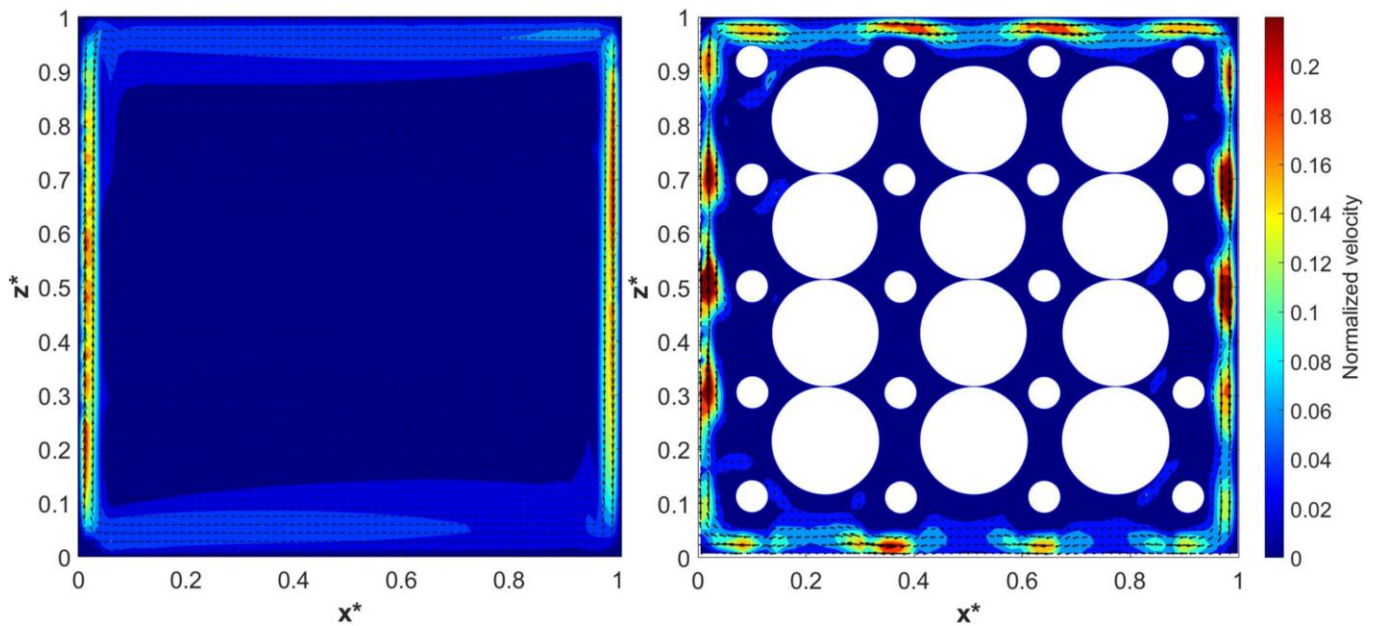


**Figure 4.9:** Normalized velocity fields of natural convection flow at  $Ra= 1.5 \times 10^8$  in the pure fluid cell (left) and in the cell filled with hydrogel balls in a BCT packing (right). Measurements performed at  $y/L = 0.4$ .

Finally, in figure 4.10 the results for both Ra-numbers in the presence of hydrogel balls are presented. At the low Ra-number, less high velocity spots are present than at the high Ra-number. From both figures it is also clear that at the high Ra-number, the flow is more symmetrical in both x- and z-direction than at the low Ra-number. A possible explanation for this may be that at a higher Ra-number, convection is more dominant than at lower Ra-number. Therefore, the convective flow is more uniformly distributed than at the low Ra-number. Also the fact that at high Ra-number, more relatively large velocity magnitudes are observed near the top- and bottom solid boundaries may strengthen the proposed claim.

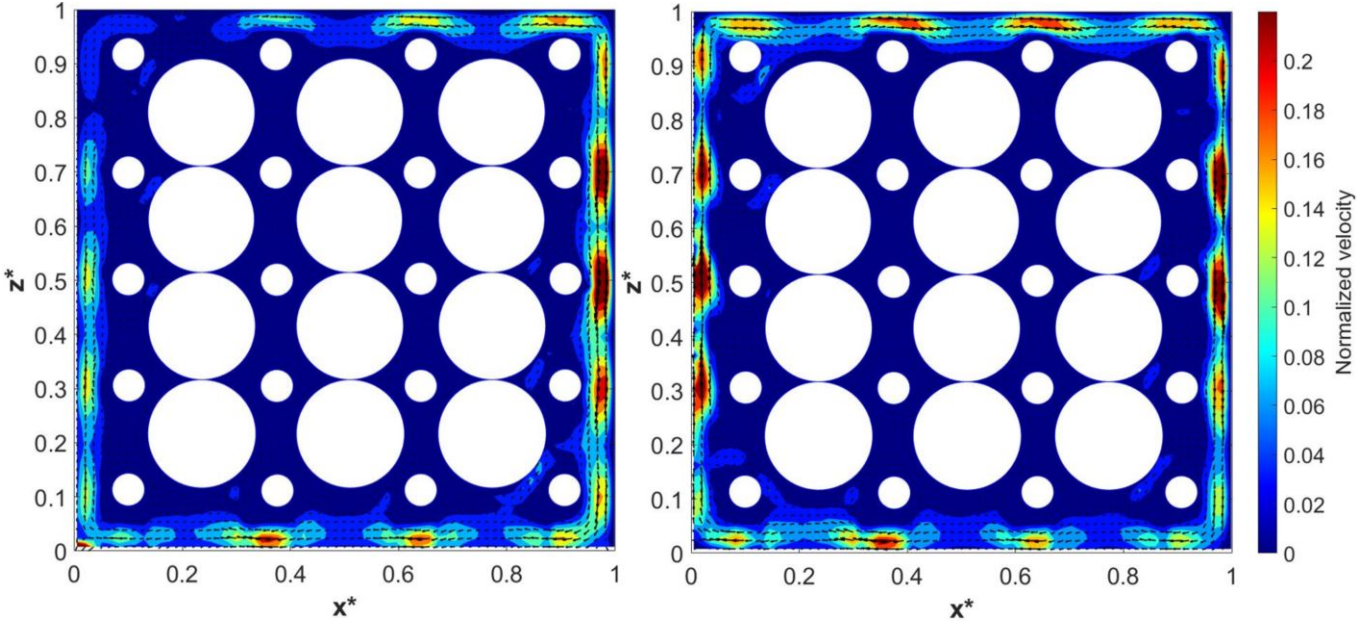


**Figure 4.10:** Normalized velocity fields of natural convection flow in the cubic enclosure filled with hydrogel balls in a BCT packing at  $Ra = 7.9 \times 10^6$  (left) and  $Ra = 1.5 \times 10^8$  (right). Measurement performed at  $y/L = 0.4$ .

#### SUMMARY OF VELOCITY FIELDS

In this section the effect of coarse-grained porous media on natural convection was presented for low and high Ra-regimes. It was shown that the flow in the empty cavity at both Ra-regimes are boundary driven and that the viscous boundary layer at the high Ra-number is thinner than at the low Ra-number, which is in accordance with literature. This behaviour also explains the fact that the heat transfer enhances when the Ra-number becomes higher, as presented in the heat transfer section 4.1. In the presence of the hydrogel balls, at both Ra-numbers there is hardly any flow in the middle of the cell since the media blocks the cubic enclosure. Also the highest velocity magnitudes are observed near the left and right walls of the cubic enclosure. The flow field at the high Ra-number shows a more uniform distribution of the flow field than at the low Ra-number. This may be due to the fact that at the higher Ra-number a more steady natural convection flow is reached since the buoyant force is much bigger than the viscous force. Also the Nusselt number at the high Ra-number is much more stable than at the low Ra-number since the measuring error is significantly lower.

The effects of the coarse-grained porous media on the flow at both Ra-numbers is significant. The high velocity regions are now present as spots near the outer region of the spheres instead of in a continuous plane near the left and right solid boundaries. Also in both cases, relatively high velocity spots are observed near the top and bottom walls. Since in the hydrogel-spheres filled enclosure at the high Ra-number higher velocities are observed near the periphery of the cell, this means that the flow experiences less resistance from the presence of the medium and can carry the heat more easily from the heated to the cooled plate.

### 4.2.2. VELOCITY DISTRIBUTION

In order to properly analyze the effects of the coarse-grained porous media on the flow inside the cubic enclosure, normalized velocity profiles at constant widths ( $x^*$ ) and heights ( $z^*$ ) are plotted. In the plots, the  $x$ - and  $z$ -axes are normalized by the width or height of the cell which are equal since the aspect ratio is  $\Gamma = 1$ . In the velocity plots, the blue-dashed lines represent the flow inside the cubic enclosure without the coarse-grained porous medium, while the black lines represent the flow inside the same cavity but filled with the coarse-grained porous medium. The hydrogel balls serve as the coarse-grained porous medium and are in the figures in the form of black small circles and big half-circles.

The locations of the lines where the normalized velocity profiles are plotted, are indicated in figure 4.11. The horizontal velocity profiles ( $x^*$ ) are plotted and analyzed at four different locations ( $x^* = 0.10, 0.37, 0.63$  and  $0.91$ ). The vertical velocity profiles ( $z^*$ ) are plotted at five different locations ( $z^* = 0.12, 0.32, 0.52, 0.72$  and  $0.92$ ).

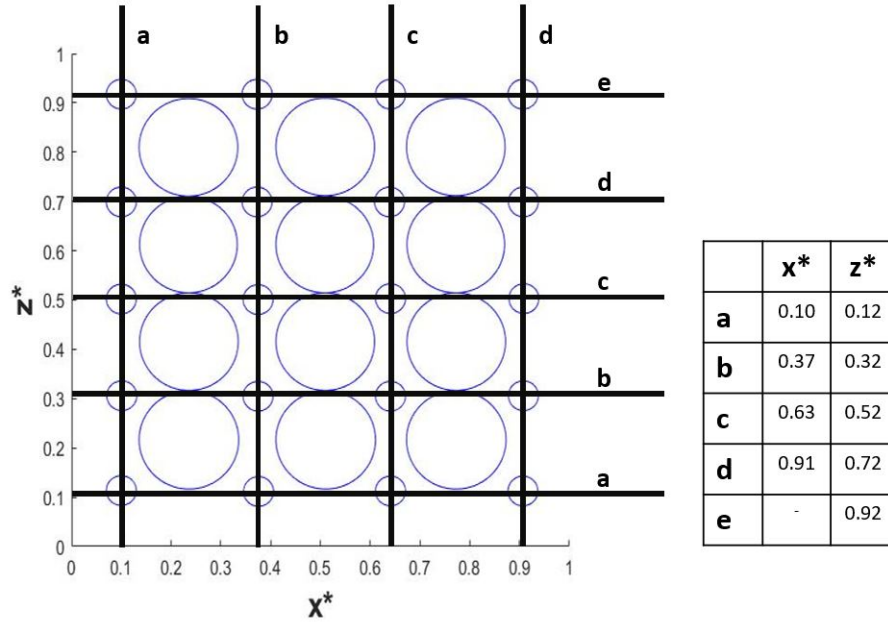


**Figure 4.11:** Different horizontal and vertical lines where the velocity profiles are studied. The table at the right side of the figure indicates the different  $x^*$  and  $z^*$ .

For visualization purposes, the vertical velocity plots for both Ra-numbers are only shown for the vertical cross-sections **a**), **c**) and **e**). The remaining two velocity profiles, **b**) and **d**) are included in appendix F.

## LOW RA NUMBER

In figure 4.12, vertical velocity component profiles ( $\bar{v}_z^*$ ) at the low Ra-number are plotted along three different horizontal lines. From all three graphs it is again confirmed that the velocities are distributed mainly near the left and right wall and that there is hardly any flow in the middle of the cell in the z-direction in both the pure fluid cell and in the porous media filled cell. This can be explained by the fact that the vertical flow in the enclosure occurs near the periphery of the cell.

At the right side, higher velocity magnitudes are reached in the presence of the hydrogel balls than without. However, near the left wall, lower velocity magnitudes can be observed in the presence of the medium than without. The main difference between the filled and non-filled results is that in the non-filled enclosure, the velocity is more widely distributed near the right wall. Near the left wall, the distribution in the filled cell shows similarities to that of the non-filled cell except for the magnitude.

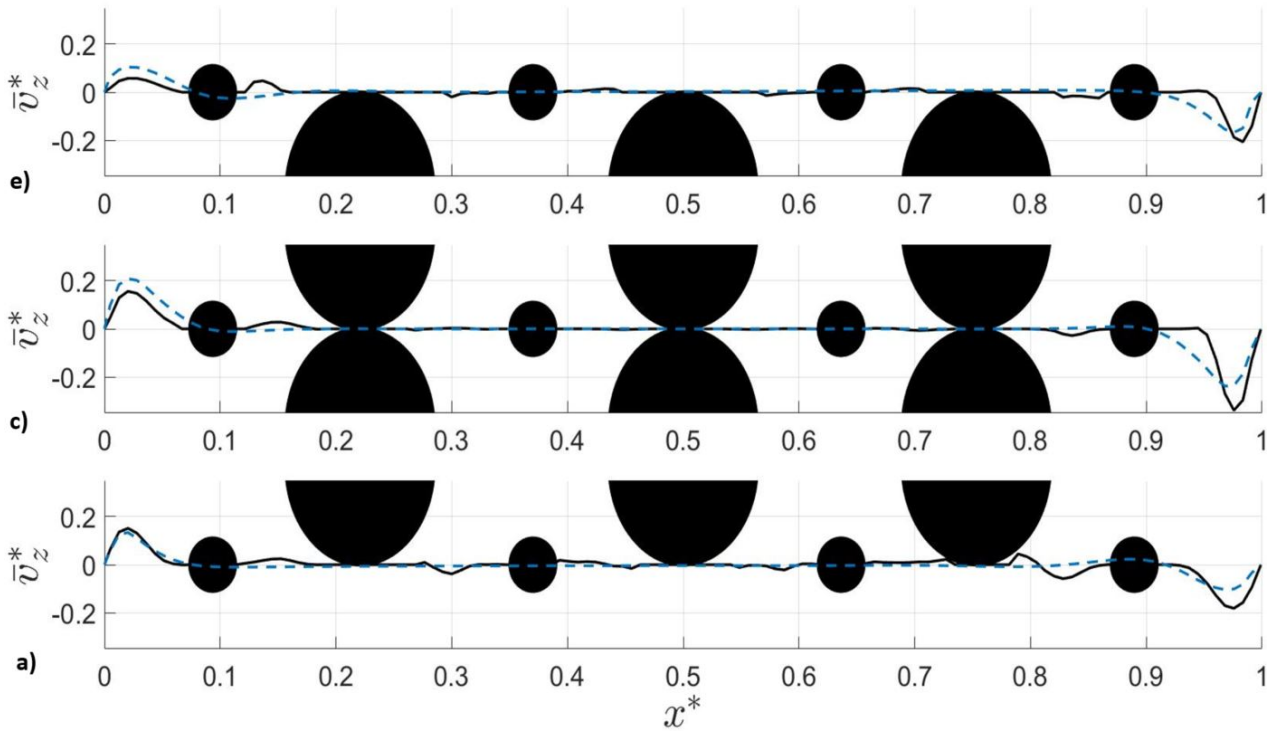


**Figure 4.12:** Effect of coarse-grained porous media on the mean vertical velocity component  $\bar{v}_z^*$  profiles at three different horizontal lines a), c) and e) (as defined in subsection 4.2.2) inside the cubic enclosure at  $Ra = 7.9 \times 10^6$ . The blue dashed lines represent the normalized velocity profiles in the pure fluid enclosure while the black lines represent the normalized velocity profiles in the BCT packed enclosure.

In figure 4.13, the horizontal velocity component profiles are presented at four different vertical lines. This result is somehow more interesting than the velocity in the  $z$ -direction, since the flow inside the water-filled enclosure is more widely distributed and anti-symmetrical at  $z^* \approx 0.5$  in all four cross-sections. From all four plots it is clear that in the middle of the cell the flow is reduced significantly in the presence of the coarse-grained porous media. In plots a) and b), there still is some flow in the  $x$ -direction, but these velocity magnitudes are still very small with respect to the velocity magnitudes at the top and bottom walls. A possible explanation for this behaviour may be that the flow is blocked heavily in the middle of the cell, and that the total observed velocity in the water-filled cell is distributed more locally near the top and bottom walls. In the presence of the spheres, higher velocity 'peaks' are observed near the top and bottom walls. In figures b), c) and d) the maximum velocity  $\bar{v}_x^*$  in the filled enclosure is roughly 2 times as high as in the empty enclosure.

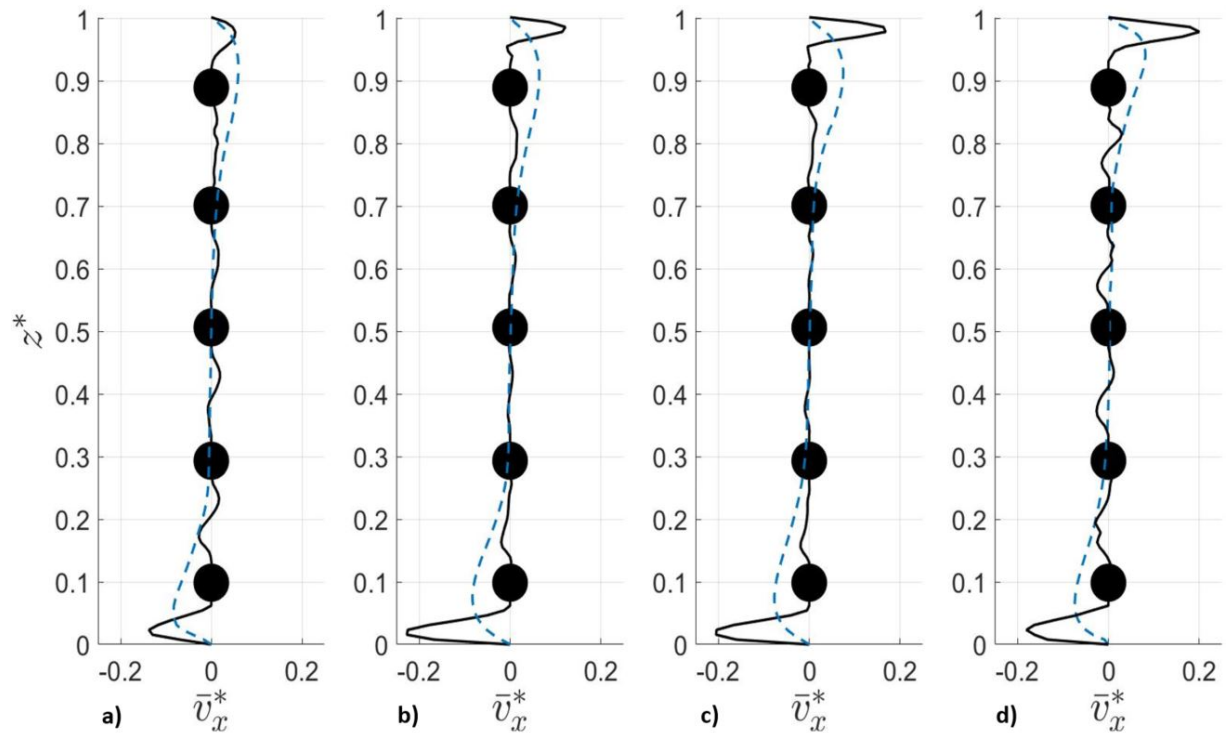


**Figure 4.13:** Effect of coarse-grained porous media on the mean horizontal velocity component  $\bar{v}_x^*$  profiles at four different vertical lines (as defined in subsection 4.2.2) inside the cubic enclosure at  $Ra = 7.9 \times 10^6$ . The blue dashed lines represent the normalized velocity profiles in the pure fluid enclosure while the black lines represent the normalized velocity profiles in the BCT packed enclosure.

## HIGH RA NUMBER

From all three plots in figure 4.14 it is clear that the  $v_z^*$ -component at the high Ra-number is also distributed primarily near the left and right walls. The width of the peaks at the left and right walls are thinner than at the low Ra-number, which was also observed from the contour-plots in the previous section. In contrast to the low Ra-regime, where the larger normalized velocities were spotted in the empty cell near the left wall, at the high Ra-number the velocity magnitudes are slightly higher in the hydrogel filled cell than in the pure-fluid cell. At the horizontal line **c)** it can be observed that near the left and right wall the velocity peak in the hydrogel filled cell is about 1.75 times larger than in the pure-fluid cell. Near the top and bottom plate (horizontal lines **a)** and **e)**) the difference between hydrogel filled cell and the pure-fluid cell is present but is not significant.

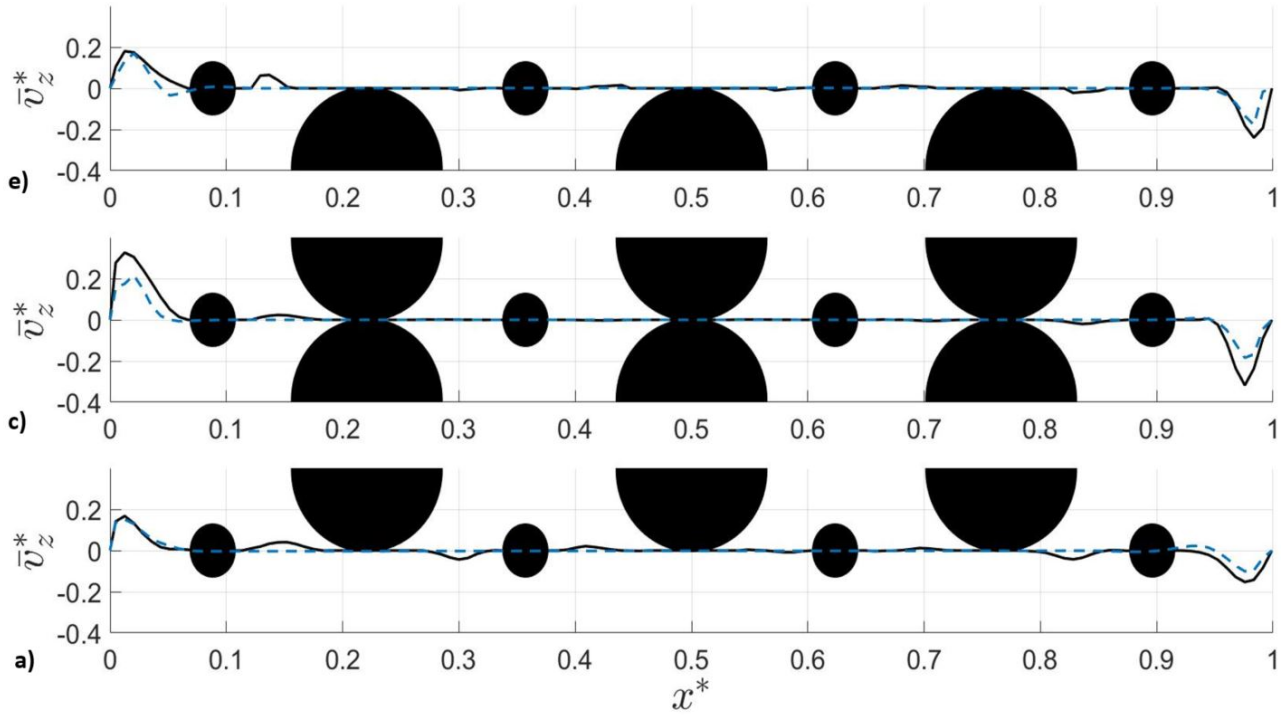


**Figure 4.14:** Effect of coarse-grained porous media on the mean vertical velocity component  $\bar{v}_z^*$  profiles at three different horizontal lines **a)**, **c)** and **e)** (as defined in subsection 4.2.2) inside the cubic enclosure at  $Ra = 1.5 \times 10^8$ . The blue dashed lines represent the normalized velocity profiles in the pure fluid cubic enclosure while the black lines represent the normalized velocity profiles in the BCT packed enclosure.

In figure 4.15, the averaged horizontal velocity component profiles,  $\bar{v}_x^*$  are given for both the pure water and hydrogel spheres filled enclosure. What immediately can be observed from the figure is that the normalized horizontal velocities in the hydrogel spheres filled cell have a significantly higher magnitude near the top and bottom plates than in the pure-fluid cell. In all 4 subplots the maximum velocity,  $\bar{v}_x^*$  is approximately 3.5-4 times larger in the hydrogel sphere filled enclosure than in the pure-fluid enclosure. The widths of the peaks are also significantly smaller in the hydrogel sphere filled cavity than in the pure-fluid cavity. What can also be observed from the plot is that the horizontal velocity profile near the bottom and the top are much more anti-symmetrically distributed for both the filled and non-filled cell. This is not the case in the low Ra-regime where the  $v_x^*$  peaks near the bottom wall have a higher magnitude in the filled case than near the top wall.

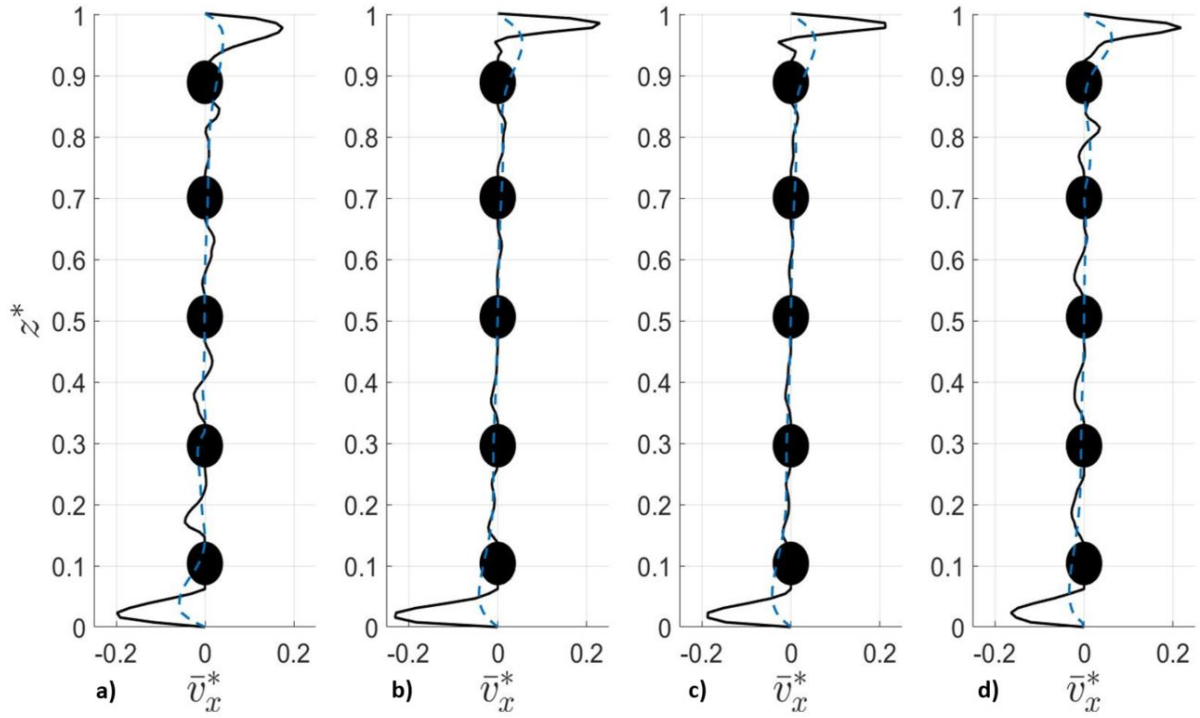


**Figure 4.15:** Effect of coarse-grained porous media on the mean horizontal velocity component profiles  $\bar{v}_x^*$  at four different vertical lines (as defined in subsection 4.2.2) inside the cubic enclosure at  $Ra = 1.5 \times 10^8$ . The blue dashed lines represent the normalized velocity profiles in the pure-fluid enclosure while the black lines represent the normalized velocity profiles in the BCT packed enclosure.

#### SUMMARY OF VELOCITY PROFILES

From the analysis of the average velocity profiles,  $\bar{v}_x^*$  and  $\bar{v}_z^*$ , it is clear that for both Ra-numbers the flow is more concentrated near the periphery of the cell in the hydrogel sphere filled enclosure while in the pure-fluid enclosure there still is some fluid motion in the middle of the cell in the horizontal lines ( $v_x$ -profiles).

At the low Ra-number, the normalized vertical velocity component  $\bar{v}_z^*$  at the boundaries is not much affected by the presence of the coarse-grained porous media and has locally almost the same velocity magnitude as in the empty enclosure. At the high Ra-number however, an increased vertical velocity of nearly 75% is observed in the presence of the hydrogel spheres with respect to the pure-fluid cell.

What is very clear from the normalized velocity component in the  $\bar{v}_x^*$  direction at both Ra-numbers, is that in the presence of the coarse-grained porous medium the flow solely occurs near the top and bottom walls, while in the empty enclosure there is also a substantial velocity in the middle of the cell. As soon as the flow meets the spherical balls near the periphery of the cell, the velocity component remains zero in this direction. A possible explanation for this behaviour in the hydrogel sphere filled enclosure can be that the spheres block the enclosure and since the flow is observed to be boundary-driven with no pore-penetration, the velocities are only distributed near the top (bottom).

### 4.3. TEMPERATURE DISTRIBUTIONS

In this section the results of the qualitative and quantitative temperature distributions are presented. With 'qualitative', it is meant that the results of the LCT measurements only give a temperature distribution by showing different colors. The 'quantitative' results are the results where each color is correlated to its corresponding temperature by means of a temperature-Hue calibration. In figures 4.16 and 4.17 the results for both the pure fluid as well as the hydrogel sphere filled enclosures are presented. Firstly, both of the enclosures are briefly discussed separately and at the end of this section a brief summary is presented where the main differences and comparisons between the pure-fluid and hydrogel sphere filled enclosures are discussed.

From the quantitative LCT experiments (subsection 3.4.4), it was found that the color distribution was at its optimum when  $T_c = 21.0^\circ\text{C}$  and  $T_h = 30.2^\circ\text{C}$  in both the pure-fluid enclosure and the hydrogel sphere filled enclosure. The corresponding Rayleigh number, at which both measurements were performed then equals  $\text{Ra} = 8.2 \times 10^7$ . Something that should be noted from the qualitative experimental results, is that the blue color represents the warmer part of the fluid while the gradually fading colors green, yellow and red represent the colder parts of the fluid.

#### 4.3.1. TEMPERATURE DISTRIBUTION IN THE PURE-FLUID ENCLOSURE

The temperature distribution in the pure-fluid enclosure shows multiple features. The liquid crystal particles are clearly visible in the qualitative figure, which is because each individual particle has a size in the order of  $\mathcal{O}(10\mu\text{m})$  and has a density very close to that of the fluid inside the enclosure. Therefore, the particles move along with the flow induced by natural convection as was also reviewed by *Dabiri* [47]. What also can be observed is that along each horizontal line the temperature is uniformly distributed. In the plane range between  $0 < z^* < 0.5$  the region is divided into the three cooler regions, of the fluid in the cubic enclosure. In the range between  $0.5 < z^* < 1.0$  the dominant color is blue which represents the solely the warm fluid.

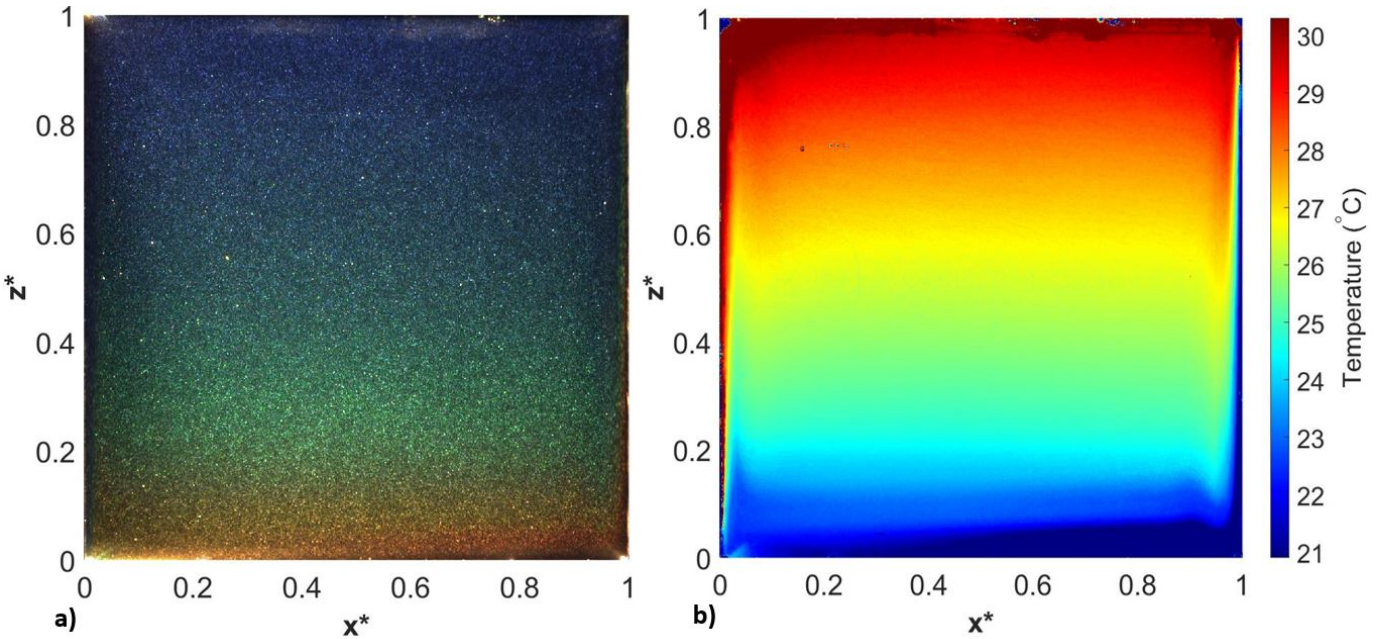


**Figure 4.16:** a) Qualitative and b) quantitative LCT result of the pure-fluid enclosure. The hot wall was kept at  $T_h = 30.2^\circ\text{C}$  and the cool wall was kept at  $T_c = 21.0^\circ\text{C}$  resulting in a Rayleigh number of  $\text{Ra} = 8.2 \times 10^7$ .<sup>4</sup>

Based on the quantitative figure, a very thin region near the right (cooled) wall at  $x^* \approx 0.99$  is observed to contain three temperature regions which have an almost equal width. The thickness of the thermal boundary layer is observed to be in the order of  $\delta/L \approx 0.01$  which is in close agreement with the theoretical value for the thermal boundary layer at this Ra-number as proposed by literature in equation 2.15 in section 2.2 of this report. In the range between  $0 < z^* < 0.5$  it can be observed that the thickness of the three colder fluid layers is not the same and increases when moving towards the middle of the cell. The total relative thickness of these temperature regions together is much thicker when compared to the region near the right boundary.

The transition between the different temperature regions seems to be quite abruptly since it is clear where the transition of the warm to the cold fluid occurs.

Near the left (heated) side of the empty enclosure, it can be observed that there is also a very thin boundary layer but is less visible than at the right (cooled) wall. Near the left wall when moving towards the middle of the cell, the warm fluid dominates the region. In the middle plane of the enclosure, at  $z^* \approx 0.5$ , it seems that the transition between the warmer fluid to a less warmer fluid is clearly visible. In the pure-fluid enclosure it can also be observed that relatively cold fluid is present near the heated wall and also the warmer fluid can be observed adjacent to the cooling wall.

Based on the distribution of the warm and cold fluid, it can be concluded that there is a vertical temperature gradient present in the pure-fluid enclosure. This is the case since the warmer fluid gradually fades into the colder fluid at  $z^* \approx 0.5$  when observing the enclosure from the top to the bottom plate.

### 4.3.2. TEMPERATURE DISTRIBUTION IN THE BCT STACKED ENCLOSURE

In figure 4.17, the temperature distribution in the hydrogel filled enclosure is presented. In this experimental result, the isotherms are also present but in a much more tenuous way. At the lower wall, at  $x^* \approx 0.9$  in the right corner it can be observed that in the presence of the coarse-grained porous medium the cold fluid region is distributed more widely than in the empty enclosure. Also it seems that the relative boundary layer near this region is much thicker than in the empty enclosure. The relative thicknesses of the three colder regions are more similarly equal to each other than in the empty enclosure where the thickness of the three colors grows when moving towards the middle of the cell. What can also be noticed in the range between  $0 < z^* < 0.5$ , is that cold temperature fluid fades into the colder temperature fluid quite smoothly and that the transition is not as abrupt as was the case in the pure-fluid enclosure. In the hydrogel filled enclosure it can also be observed that cold fluid can be observed near the heated wall (lower left corner) and also the warmer fluid can be observed adjacent to the cooling wall (upper right corner). This means that both the hot and the cold fluid can penetrate deeply from both sides.

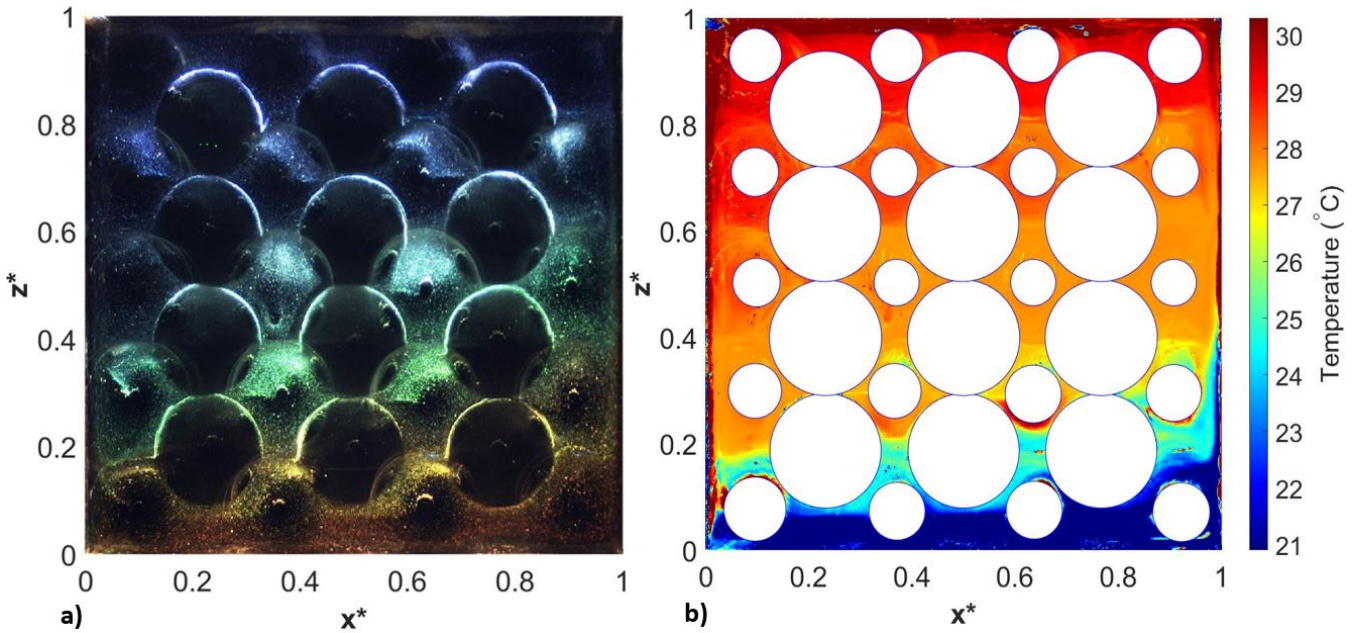


**Figure 4.17:** a) Qualitative and b) quantitative LCT result in the hydrogel spheres filled enclosure. The hot wall was kept at  $T_h = 30.2^\circ\text{C}$  and the cool wall was kept at  $T_c = 21.0^\circ\text{C}$  resulting in a Rayleigh number of  $Ra = 8.2 \times 10^7$ .

Near the left wall, in the  $x^* = 0.1$  plane, it can be observed that the temperature distribution is dominated by the warm fluid from  $0.4 < z^* < 1.0$ , whereas in the pure-fluid enclosure the different temperature regions are more equally distributed between the cool part and the warm part of the fluid. In the plane between  $0.3 < x^* < 0.7$ , it can be recognized that the cool temperature dominates the defined domain from  $0 < z^* < 0.6$  and that the rest of this domain is filled with the warm fluid. In the plane between  $0.7 < x^* < 1.0$  it can be observed that the cooled fluid dominates almost 80% of the whole plane, while just a relative small part is dominated by the warmer fluid.

Based on the distribution of the warm and cold fluid in the hydrogel sphere filled enclosure, it can be explained that there is a merely diagonal temperature gradient present in the enclosure between the left upper corner and the right lower corner. This is the case since the warmer fluid gradually fades into the colder fluid when observing the enclosure from the top to the bottom plate.

#### SUMMARY OF LCT MEASUREMENTS

As discussed for the pure-fluid cell and the hydrogel sphere filled enclosure, it can be shown that there are clear differences in temperature distribution between a pure-fluid enclosure and an enclosure which is filled with coarse-grained porous media.

The main observation from the pure-fluid enclosure is that the fluid temperature gradually increases from the bottom to the top which indicates that there is a vertical temperature gradient present. The two parts are distributed quite uniformly throughout the enclosure and the approximated thermal boundary layer thickness is in close agreement with the values as reported by literature. As an extra observation, the streamlines which follow the fluid flow and are also in close agreement with the reported streamline-figure in the literature.

From the hydrogel spheres filled enclosure, the main observation is that the distribution of the temperature in the enclosure is not as uniform as in the empty enclosure and that there exists a diagonal temperature gradient instead of a vertical gradient. Between  $0 < x^* < 0.2$ , the vertical distribution is dominated for 60% by the warmer fluid while between  $0.3 < x^* < 0.7$  the vertical distribution is dominated by the colder fluid. Near both sides of the left and right walls it can also be noticed that the color distribution fades into each other quite smoothly while in the empty cell the transition of the colors near the cold wall is near abruptly.

# 5

## CONCLUSION

An experimental investigation was conducted to study the effect of coarse-grained porous media on natural convection inside a side-heated cubic enclosure. In this experimental study, the porous length scales are large compared to the flow and thermal length scales. Heat transfer measurements were performed for  $1.9 \times 10^7 \leq Ra \leq 1.5 \times 10^9$  where the Nusselt number was calculated for different coarse-grained porous media. The effects of spherical balls with different conductivities, different sizes, and different packing types on natural convection were tested and compared to the pure-fluid cubic enclosure where no coarse-grained porous media were present. Also optical measurement techniques, Particle Imaging Velocimetry and Liquid Crystal Thermography were used to study the planar velocity and temperature distributions inside the enclosure. For these experiments, water was used as the working fluid and hydrogel balls were used as the coarse-grained porous media to allow optical accessibility. Darcy's law is not relevant for this study since the porous length scales of the present media are much larger than the thermal length scales. The ratio between the length of the enclosure and the diameter of the spheres in most cases was:  $L/D=5.0$ .

From the heat transfer measurements it was found that the Nu-number, and thus the heat transfer, increased for every increase in Ra-number. This was the case for both the pure-fluid heat transfer experiments and the porous media experiments. A power relation was found for side-heated natural convection in the pure-fluid enclosure:

$$Nu = 0.250 \times Ra^{0.264} \quad 1.9 \times 10^7 \leq Ra \leq 1.5 \times 10^9 \quad (5.1)$$

For all heat transfer experiments in the cavity with porous medium it was found that in the lower Ra regime the heat transfer was reduced heavily than in the higher Ra-regime with respect to the pure-fluid cavity. Also, when testing the effects of materials with different conductivities, the heat transfer was observed to be higher for high conductive porous media compared to lower conductive media. In the experiments performed to test the different packing types, it was observed that the BCT and SCP packing reduced the overall heat transfer more than the random packing. The reason given for this behaviour is that in the random packing configuration, the hot and cold vertical walls are not covered as densely as in the case for the BCT and SCP configurations. From the heat transfer experiments performed to test the effects of different sized spheres, it was observed that the heat transfer was reduced heavily in the presence of the lower sized balls than the bigger sized balls in the lower Ra-regime. In the higher Ra-regime however, the heat transfer was observed to move in the direction of the pure-fluid-cavity fit, although it never reached the asymptotic value in this specific Ra-range as used in this study. Although, the porosity of both the small and big sized spheres are very close to each other, a significant difference was observed between their heat transfer results. A possible reason for this behaviour may be that the smaller sized balls are more densely packed near the hot and cold vertical wall where the bulk of the fluid flow occurs.

The Particle Imaging Velocimetry (PIV) experiments show that the flow in a side-heated cubic enclosure is boundary driven and that the flow in the middle of the cell is negligible with respect to the velocities near the periphery of the enclosure. It was also found that the thickness of the high velocity regions near the warm and cool plates were significantly smaller for the higher Ra-number ( $Ra = 1.5 \times 10^8$ ) than for the lower Ra-number ( $Ra = 7.9 \times 10^6$ ). The velocities at the high Ra-number were significantly larger than the velocities at the low Ra-number. From the velocity distribution it was found that for both low and high Ra-numbers for the pure-fluid cavity there is a more uniformly distributed flow throughout the cell (periphery and middle of the cell) than when the coarse-grained porous medium was present.

From both the qualitative and the quantitative Liquid Crystal Thermography (LCT) experiments, which were performed at  $Ra = 8.2 \times 10^7$ , it was found that the temperature in the pure-fluid cell is uniformly distributed along each horizontal line and a vertical temperature gradient can be observed. The upper part of the cubic enclosure ( $0.5 < z^* < 1.0$ ) is dominated by the warm fluid while the lower part ( $0 < z^* < 0.5$ ) is dominated by the colder fluid. In the hydrogel spheres filled enclosure, the distribution of the warm and cold fluid was found to be different and a diagonal temperature gradient was observed.

# 6

## RECOMMENDATION

In the current study, three experimental methods have been used to study the effects of coarse-grained porous media on natural convective flows where  $L/D=5.0$ . Further research is necessary to obtain an even better understanding of the physical mechanisms influencing natural convection in coarse-grained porous media. In this chapter, several recommendations are proposed for further research.

### 6.1. TURBULENT FLOWS

The natural convection flow in the current study at the defined Ra-numbers was observed to be laminar. *Am-pofo et al.* [52] reported in their highly accurate experimental study that in a side-heated enclosure, low-level turbulent behaviour was observed for  $Ra = 1.58 \times 10^9$ . It may be an interesting experiment to see what the effect of the coarse-grained porous media is when a turbulent flow is considered. A similar experimental study as reported in this report, is therefore proposed for higher Ra-numbers to study the effects of coarse-grained porous media on the natural convective flow. To reach  $Ra > 10^9$ , cubical enclosures with larger dimensions are proposed since the Ra-number is proportional to  $Ra \propto L^3$ . In these experiments, also optical measurement techniques like PIV and LCT should be used to especially study the behaviour of the flow and the temperature distribution at high Ra-numbers. At higher Ra-numbers, the heat transfer experiments can also determine where the lower conductive spherical materials reach the asymptotic value of the empty cavity.

A quick calculation learns that when a cubical enclosure is considered with dimensions  $H \times L \times W = 0.155m \times 0.155m \times 0.155m$  (and is available), where the left wall is heated and the right wall is cooled, a maximum Ra-number can be reached of nearly  $1.5 \times 10^9$  which is already one order of magnitude higher than can be achieved in the present study. In this Ra-region the flow is softly turbulent and can also be studied using hydrogel balls. To maintain the same  $L/D$  ratio, hydrogel balls with a diameter of 3 cm should be used which is an available material in commercial markets. The reason that no PIV or LCT experiments were performed in the available large cell is that of time-constraints.

### 6.2. EXTENDED QUANTITATIVE LIQUID CRYSTAL EXPERIMENT

The temperature distributions in the side-heated cubical enclosure which were reported in this report, are based on both a qualitative and a quantitative experiment. The cubical enclosure was lit from above with a sheet of white line-light. Based on the observations of the quality of the colored LCT images, the light in the pure-fluid enclosure was distributed uniformly. In the hydrogel sphere filled enclosure however, the light was not uniformly distributed (light was brighter in the upper part of the cell). Also some shadowy effects of the balls caused some noise, especially near the left and right (heated and cooled) walls.

A possible recommendation for future research purposes to overcome this problem may be to test what the effect will be in the same configuration but now lit from the bottom instead from the top. When it turns out that from the bottom-lit configuration, the problem is just flipped as one would expect, a more challenging scenario can also be tested by shining the line-sheet of white light from both the top and the bottom at the same time.

### 6.3. PRESSURE DISTRIBUTION

Another proposal for an additional experimental investigation to give a more complete overview of the physical mechanisms of what actually affects the natural convection in a filled cell, is to study the pressure distribution. The pressure distribution in the enclosure which is filled with coarse-grained porous media can then be compared to the pressure distribution in the empty enclosures.

*Lankhorst et al.* [1] showed in his PhD dissertation that the pressure is distributed quite uniformly in a side-heated water-filled cubic enclosure and that the pressure gradient,  $\frac{\partial p}{\partial x}$  is zero almost everywhere. However, in the upper left and lower right corner, near the top and bottom walls, a locally higher pressure region was observed. This observation was explained by reasoning that the vertical velocities near the left and right boundary touch the horizontal walls in these corners and cause the pressure to be locally higher.

In the current study, higher velocity 'spots' are observed near all four walls in the presence of the coarse-grained porous media. It may be interesting to experimentally obtain the pressure distribution in the enclosure and to see how the presence of the media affects this pressure distribution. The same cubical enclosure can be used for these experiments, only a reference pressure needs to be measured and defined. This can be done using a pressure transducer, which are commercially available. For instance, OMEGA offers accurate pressure transducers [53]. The pressure difference in the above mentioned spots is very small, but it may be interesting to see what the effect is of the coarse-grained porous media on the pressure distribution to enhance knowledge on momentum transfer in the enclosure filled with a coarse-grained porous medium.

### 6.4. EXTENDED NON-COVERED BOUNDARY LAYER EXPERIMENT

As an additional part of this experimental study, a 3D-structure was printed with the intention to have a packed bed in the middle of the enclosure where the left and right wall were not touched. The material used for this structure is a special type of resin with near similar thermal properties as polypropylene. The thermal conductivity of the material is therefore very low. It would be interesting to also test the exact same structure but now constructed from a high conductive material, such as steel or brass.

A possible material which can be used for this proposed experiment are magnetic Buckyballs. These balls are Neodymium magnets [54] and are usually used as toys or stress-relief products. The pleasant property of these balls are that they can be stacked on top of each other, forming an SCP packing and has a thermal conductivity of  $10 \text{ W}/(\text{m}\cdot\text{K})$  which is roughly 50 times higher than the thermal conductivity of the 3D-printed material. The balls are commercially available in different sizes from the *BuckyballsStore* [55].

## BIBLIOGRAPHY

- [1] A. M. Lankhorst, *Laminar and turbulent natural convection in cavities: numerical modeling and experimental validation*, Ph.D. thesis, TU Delft, Delft University of Technology (1991).
- [2] I. J. Opstelten, *Experimental study on transition characteristics of natural-convection flow*, (1994).
- [3] T. Fusegi, J. M. Hyun, K. Kuwahara, and B. Farouk, *A numerical study of three-dimensional natural convection in a differentially heated cubical enclosure*, *International Journal of Heat and Mass Transfer* **34**, 1543 (1991).
- [4] P. Wang, Y. Zhang, and Z. Guo, *Numerical study of three-dimensional natural convection in a cubical cavity at high rayleigh numbers*, *International Journal of Heat and Mass Transfer* **113**, 217 (2017).
- [5] I. Ataei-Dadavi, S. Kenjeres, M. Tummers, and C. Kleijn, *Natural convection heat transfer measurements in coarse-grained porous media*, 9th World Conference on experimental Heat Transfer, Fluid mechanics and Thermodynamics - Submitted to the *International Journal of Heat and Mass Transfer* (2017).
- [6] D. A. Nield and Bejan, *Convection in porous media*, Vol. 3 (Springer, 2006).
- [7] J. Williams, *Science of summer: Where does beach sand come from?* <https://www.livescience.com/38163-where-beach-sand-comes-from.html> (2013).
- [8] D. Hewitt, J. Neufeld, and J. Lister, *High rayleigh number convection in a three-dimensional porous medium*, *Journal of Fluid Mechanics* **748**, 879–895 (2014).
- [9] J. Otero, L. A. Dontcheva, H. Johnston, R. A. Worthing, A. Kurganov, G. Petrova, and C. R. Doering, *High-rayleigh-number convection in a fluid-saturated porous layer*, *Journal of Fluid Mechanics* **500**, 263–281 (2004).
- [10] J. E. Weber, *The boundary-layer regime for convection in a vertical porous layer*, *International Journal of Heat and Mass Transfer* **18**, 569 (1975).
- [11] G. Lauriat and V. Prasad, *Non-darcian effects on natural convection in a vertical porous enclosure*, *International Journal of Heat and Mass Transfer* **32**, 2135 (1989).
- [12] N. Seki, S. Fukusako, and H. Inaba, *Heat transfer in a confined rectangular cavity packed with porous media*, *International Journal of Heat and Mass Transfer* **21**, 985 (1978).
- [13] V. Prasad, F. Kulacki, and M. Keyhani, *Natural convection in porous media*, *Journal of Fluid Mechanics* **150**, 89 (1985).
- [14] K. Aziz, P. Holt, P. Karra, *et al.*, *Natural convection in porous media*, in *Annual Technical Meeting* (Petroleum Society of Canada, 1968).
- [15] S. Bories, *Natural convection in porous media*, in *Advances in transport phenomena in porous media* (Springer, 1987) pp. 77–141.
- [16] E. J. Braga and M. J. De Lemos, *Heat transfer in enclosures having a fixed amount of solid material simulated with heterogeneous and homogeneous models*, *International Journal of Heat and Mass Transfer* **48**, 4748 (2005).
- [17] E. J. Braga and M. J. de Lemos, *Laminar natural convection in cavities filled with circular and square rods*, *International communications in heat and mass transfer* **32**, 1289 (2005).
- [18] A. A. Merrikh and J. L. Lage, *Natural convection in an enclosure with disconnected and conducting solid blocks*, *International Journal of Heat and Mass Transfer* **48**, 1361 (2005).

- [19] A. Raji, M. Hasnaoui, M. Naimi, K. Slimani, and M. Ouazzani, *Effect of the subdivision of an obstacle on the natural convection heat transfer in a square cavity*, *Computers & Fluids* **68**, 1 (2012).
- [20] D. J. Keene and R. Goldstein, *Thermal convection in porous media at high rayleigh numbers*, *Journal of Heat Transfer* **137**, 034503 (2015).
- [21] I. Ataei-Dadavi, M. Chakkingal, S. Kenjeres, C. R. Kleijn, and M. J. Tummers, *Flow and heat transfer measurements in natural convection in coarse-grained porous media*, *International Journal of Heat and Mass Transfer* **130**, 575 (2019).
- [22] CNBC, *Thyssenkrupp, tata steel seal landmark steel joint venture deal*, (30-07-2018).
- [23] K. Andreev, S. Sinnema, and M. Hogenboom, *Investigation of refractory concrete failure in furnaces of metals industry*, *Ceramics Research Centre, Corus RD&T, The Netherlands*, 1 (2009).
- [24] Indiamart, *Blast furnace*, (2016).
- [25] N. C. Markatos and K. Pericleous, *Laminar and turbulent natural convection in an enclosed cavity*, *International Journal of Heat and Mass Transfer* **27**, 755 (1984).
- [26] K. Hanjalić, S. Kenjeres, M. J. Tummers, and H. J. J. Jonker, *Analysis and modelling of physical transport phenomena* (VSSD, 2007).
- [27] M. Kapitz, C. Teigeler, R. Wagner, C. Helcig, and S. aus der Wiesche, *Experimental study of the influence of the prandtl number on the convective heat transfer from a square cylinder*, *International Journal of Heat and Mass Transfer* **120**, 471 (2018).
- [28] W. M. Deen, *Analysis of Transport Phenomena, Topics in Chemical Engineering*, Vol. 3 (Oxford University Press, New York, 1998).
- [29] R. Stieglitz, *Low prandtl number thermal-hydraulics*, *Handbook on lead-bismuth eutectic alloy and lead properties, material compatibility, thermal-hydraulics and technologies*, OECD (2007).
- [30] J. Holman, *Heat transfer, 1986*, Mc Gran–Hill Book Company, Soythern Methodist University (1986).
- [31] L.P.B.M Janssen; M.M.C.G Warmoeskerken, *Transport phenomena data companion*, (2013), online; accessed 29 January 2014.
- [32] H. Herwig, *What exactly is the nusselt number in convective heat transfer problems and are there alternatives?* *Entropy* **18**, 198 (2016).
- [33] S. Kenjeres, *Special topics: Thermal convection*, *Continuum Physics Lectures Series* (2017-2018).
- [34] H. Brinkman, *A calculation of the viscous force exerted by a flowing fluid on a dense swarm of particles*, *Flow, Turbulence and Combustion* **1**, 27 (1949).
- [35] *Natural convection - free convection*, <https://www.nuclear-power.net/nuclear-engineering/heat-transfer/convection-convective-heat-transfer/natural-convection-free-convection/> (2017).
- [36] A. Bejan, *Convection heat transfer* (John wiley & sons, 2013).
- [37] M. Steunebrink, *Effect of surface roughness on flow and heat transfer in Rayleigh-Bénard convection*, Master's thesis, Delft University of Technology, Mekelweg 1 (2013).
- [38] D. Database, *Thermophysical data for process design*, (12-09-2013).
- [39] *Methanol*, <http://www.thermopedia.com/content/952/>, accessed: 2018-08-08.
- [40] J. D. Anderson, G. Schubert, V. Trimble, and M. R. Feldman, *Measurements of newton's gravitational constant and the length of day*, *EPL (Europhysics Letters)* **110**, 10002 (2015).
- [41] P. J. Bártolo, *Stereolithography: materials, processes and applications* (Springer Science & Business Media, 2011).

- [42] Artcorp, *Polyjet materials data sheet*, (2017).
- [43] E. M. Ahmed, *Hydrogel: Preparation, characterization, and applications: A review*, Journal of advanced research **6**, 105 (2015).
- [44] Ace lightsource, <https://www.us.schott.com/lightingimaging/english/microscopy/products/coldvision/acelightsource.html> (2018).
- [45] Waldmann mcxfl3s - light source, <https://nl.farnell.com/waldmann/mcxfl-3-s/lamp-head-led-spotlight-24v/dp/1360454> (2017).
- [46] A. R. Smith, *Color gamut transform pairs*, ACM Siggraph Computer Graphics **12**, 12 (1978).
- [47] D. Dabiri, *Digital particle image thermometry/velocimetry: a review*, Experiments in Fluids **46**, 191 (2009).
- [48] J. de Geus, *Mixed convection: A CFD study in a side heated cavity filled with coarse grained porous media.*, Master's thesis, Delft University of Technology, Mekelweg 1 (2018).
- [49] E. Tric, G. Labrosse, and M. Betrouni, *A first incursion into the 3d structure of natural convection of air in a differentially heated cubic cavity, from accurate numerical solutions*, International Journal of Heat and Mass Transfer **43**, 4043 (2000).
- [50] J. Patterson and J. Imberger, *Unsteady natural convection in a rectangular cavity*, Journal of Fluid Mechanics **100**, 65–86 (1980).
- [51] G. Ivey, *Experiments on transient natural convection in a cavity*, Journal of Fluid Mechanics **144**, 389 (1984).
- [52] F. Ampofo and T. Karayiannis, *Experimental benchmark data for turbulent natural convection in an air filled square cavity*, International Journal of Heat and Mass Transfer **46**, 3551 (2003).
- [53] *Pressure transducers and transmitters*, <https://www.omega.nl/prodinfo/pressure-transducers.html>, omega - A Spectris Company. Accessed: 04-10-2018.
- [54] *Goodfellow*, <http://www.goodfellow.com/A/Neodymium-Iron-Boron.html>, neodymium/iron/boron - Accessed: 04-10-2018.
- [55] *Buckyballs*, <https://www.buckyballsstore.com/>, buckyballsStore. Accessed: 04-10-2018.



**A**

## **HEATING PAD SPECIFICATIONS**

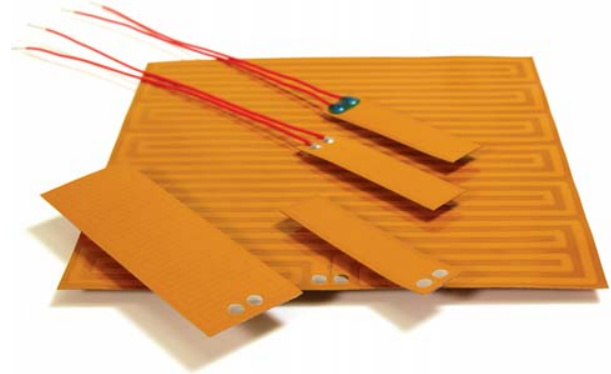
# Commercial Grade Polyimide Heaters

## Reliable heating options at an affordable price

### Overview

Minco's commercial grade polyimide heaters provide the performance and reliability you expect at a lower cost than our standard polyimide/FEP models. Sizes are available for 12 and 24 volt operation, or connect multiple heaters in a series/parallel system for consistent power over larger areas.

- Solder pad option provides you the lowest price possible for Minco polyimide heaters
- All models include acrylic pressure sensitive mounting adhesive (PSA) for simple installation
- Ideal for prototyping, short production series or high volume/low cost applications
- Typical lead time is 3-5 days ARO



Commercial grade polyimide heaters

Polyimide Heaters

### Specifications

**Temperature range:** -32 to 100°C .

**Material:** Polyimide film/acrylic (Kapton™ or equivalent).

**Resistance tolerance:** ±10%.

**Minimum bend radius:** 0.030" (0.8 mm).

**Electrical connection options:** Exposed solder pads. Options include two AWG 26 PTFE insulated leadwires 4" (100 mm) long with insulated or bare connection points.

### Insulated connection wire for end-user attachment

Order loose insulated connection wires with stripped ends for fast, easy connection of heaters to your power source. These AWG 26 wires have high temperature PTFE insulation resistant to wear and abrasion. The insulation color is red and the standard length is 4" (100 mm). Wires are sold in pairs, order one pair for each heater. Order part number AC102371.

### Specification options

HK5950	Base model from table
L	Termination options:*
	S = Solder pads
	L = 4" (100 mm) PTFE insulated leadwires - lead attachment area not insulated
	P = 4" (100 mm) PTFE insulated leadwires with insulated connection points
HK5950L = Sample part	

\*Due to solder junctions parts are not RoHS compliant

### Base model table

Model numbers	Size (inches)	Size (mm)	Resistance in ohms	Voltage	Watt density W/in <sup>2</sup> (W/cm <sup>2</sup> )	Effective area in <sup>2</sup> (cm <sup>2</sup> )
HK5950	0.5 x 2.0	12.7 x 50.8	57.5	12	2.5 (0.39)	1.0 (6.45)
HK5951	1.0 x 1.0	25.4 x 25.4	57.5	12	2.5 (0.39)	1.0 (6.45)
HK5952	0.5 x 5.0	12.7 x 127	23.0	12	2.5 (0.39)	2.5 (16.13)
HK5953	1.0 x 3.0	25.4 x 76.2	19.2	12	2.5 (0.39)	3.0 (19.35)
HK5954	2.0 x 2.0	50.8 x 50.8	57.6	24	2.5 (0.39)	4.0 (25.81)
HK5955	3.0 x 3.0	76.2 x 76.2	25.6	24	2.5 (0.39)	9.0 (58.06)
HK5956	4.0 x 4.0	101.6 x 101.6	14.4	24	2.5 (0.39)	16.0(103.2)
HK5957	5.0 x 5.0	127 x 127	9.2	24	2.5 (0.39)	25.0 (161.29)

Specifications subject to change



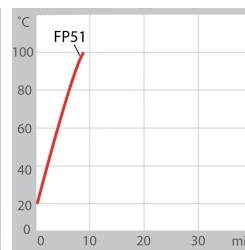
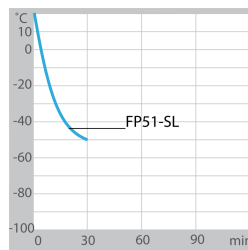
# B

## THERMOSTATIC BATH SPECIFICATIONS

## FP51-SL Ultra-Low Refrigerated-Heating Circulator

### Superior models for most demanding applications

JULABO Ultra-Low Refrigerated Circulators for heating and cooling are suitable for external temperature tasks. Powerful circulating pump systems and high heating and cooling capacities guarantee short heat-up and cool-down times. ACC 'Active Cooling Control' provides active cooling control across the whole temperature range. An energy saving feature with only minor loss of heat is provided by the proportional cooling capacity control in the 'FP' refrigeration units. The inevitable dust accumulation that occurs in refrigeration systems is solved by means of an easily removed venting grill, which allows for easy cleaning. The units are equipped with handles or castors for an easy transportation. All models have a drain tap on the front allowing the fluid to be drained easily. Additionally the instruments are equipped with an improved insulation to help avoid ice-formation, and have a visual liquid level display.



- Cool-down time (Ethanol)
- Heat-up time (thermal)

### Your advantages

- VFD COMFORT DISPLAY
- LCD DIALOG DISPLAY backlit for convenient interactive operation
- Keypad for setpoints, warning/safety values and menu functions
- ICC (Intelligent Cascade Control), self-optimizing temperature control
- TCF Temperature Control Features to optimize the control behaviour
- ATC3 3-Point-Calibration
- Pt100 External sensor connection for measurement and control
- SMART PUMP, electronically adjustable pump stages
- Early warning system for low liquid level (DBGM 203 06 059.8)
- Adjustable high temperature cut-out, visible via display
- RS232/RS485 interface for online communication
- Integrated programmer for 6 x 60 program steps
- Connections for solenoid valve and HSP booster pump
- Proportional cooling control
- Active Cooling Control
- Proportional cooling control

### Technical Data

Order No.	9352751
Model series	HighTech
Category	Ultra-Low Refrigerated-Heating Circulators
Working temperature range (°C)	-51 ... +200
Temperature stability (°C)	±0.05
Setting / display resolution	0.01 °C
Integrated programmer	6x60 steps

Temperature Display	VFD, LCD										
Heating capacity (kW)	3										
Cooling capacity (Medium Ethanol)	<table border="0"> <tr> <td>°C</td> <td>20</td> <td>0</td> <td>-20</td> <td>-40</td> </tr> <tr> <td>kW</td> <td>2</td> <td>1.5</td> <td>1</td> <td>0.26</td> </tr> </table>	°C	20	0	-20	-40	kW	2	1.5	1	0.26
°C	20	0	-20	-40							
kW	2	1.5	1	0.26							
Pump capacity flow rate (l/min)	22-26										
Pump capacity flow pressure (bar)	0.4-0.7										
Pump capacity flow suction (bar)	0.2-0.4										
Bath opening / bath depth (W x L / D cm)	18 x 12 / 20										
Pump connections	M16x1										
Barbed fittings diameter (inner dia. / mm)	8 / 12										
Filling volume liters	11										
Refrigerant stage 1	R507										
Filling volume refrigerant stage 1 (g)	1030										
Global Warming Potential for R507	3985										
Carbon dioxide equivalent stage 1 (t)	4.105										
External Pt100 sensor connection	integrated										
Digital interface	RS232, RS485 Optional: Profibus										
Ambient temperature	5...40 °C										
Dimensions W x L x H (cm)	46 x 55 x 89										
Weight (kg)	90										
Classification according to DIN12876-1	Classification III (FL)										
Included with each unit	2 each barbed fittings for tubing 8 and 12 mm inner dia. (pump connections M16x1 male).										
Cooling of compressor	Air										
Available voltage versions	230 V / 3 Ph. / 50 Hz 400 V / 3 Ph. / 50 Hz 208 V / 3 Ph. / 60 Hz										

## Characteristics

### Display



#### A perfect view

Ample, easy to read VFD Comfort display for simultaneous display of 3 values, warning functions, high temperature cut-off, pump stages (resolution 0.01 °C)



#### Additional plain text information

Comfortable LCD dialog display for interactive operation with plain text display



#### Pump stage and liquid level

Backlit indicator for selected pump stages and filling volume on Presto® PLUS, Magnum 91 & Forte HT

### Operation



#### Comfortable and detailed

Comfortable keypad with additional menu functions for pump stages, calibration, control parameters, programmer, warnings, etc.

### Temperature Control



#### For perfect results

'Intelligent Cascade Control', automatic & self optimizing adjustment of PID control parameters, temperature stability ±0.005 °C internal, <±0.05 °C external

**TCF Full control**  
 'Temperature Control Features' for individual optimization, access to all important control parameters, additional settings for band limit, limits, Co-Speedfactor etc.

**ATC<sup>3</sup> Highest measuring accuracy**  
 'Absolute Temperature Calibration' for manual compensation of a temperature difference, 3-point calibration

**Optimal program control**  
 For the execution of time and temperature dependant profiles, 6 temperature profiles with 60 steps max., with real time clock

**Automatic control of operating time**  
 Electronic countdown-timer function for timer-programmed unit shut-down, standby mode after programmed time expires

## Refrigeration Technology

**Energy saving cooling**  
 Proportional cooling control for automatic adjustment of cooling power or temporary switch-off of compressor as needed to save up to 90 % energy in comparison to unregulated cooling machines

**Consistent cooling capacity**  
 Easily removable venting grid for quick and easy cleaning

**ACC 100 % Cooling capacity**  
 'Active Cooling Control' for cooling available throughout the entire working temperature range, fast cool-down even at higher temperatures

**Condensation and ice protection**  
 A heated cover plate prevents condensation or ice build-up in the bath

## Warning & Safety Functions

**Early warning system for low liquid level**  
 Maximum safety for applications, optical and audible alarm, allows user to refill bath fluid before the unit shuts down

**Early warning system for high/low temperature limits**  
 Maximum safety for applications, optical and audible alarm, convertible to automated cut-off function

**Enhanced protective functions**  
 Maximum safety, adjustable high temperature cut-off or dry-running protection, additional display of setpoints permits easy and precise adjustments

**S3 For flammable bath fluids**  
 Classification III (FL) according to DIN 12876-1

## Technical Features

**SMART PUMP Clever pump system**  
 Reliable and consistent pump capacity, electronically adjustable pump stages

**Pt 100 Control from the external application**  
 External Pt100 sensor connection for precise measurement and control directly in the external application

**RS 232 RS 485 Connection compliant to standard**  
 RS232/RS485 dual-interface for serial data transmission according to EIA-485 industry standard (2-wire bus technology), upgradable with Profibus DP

# C

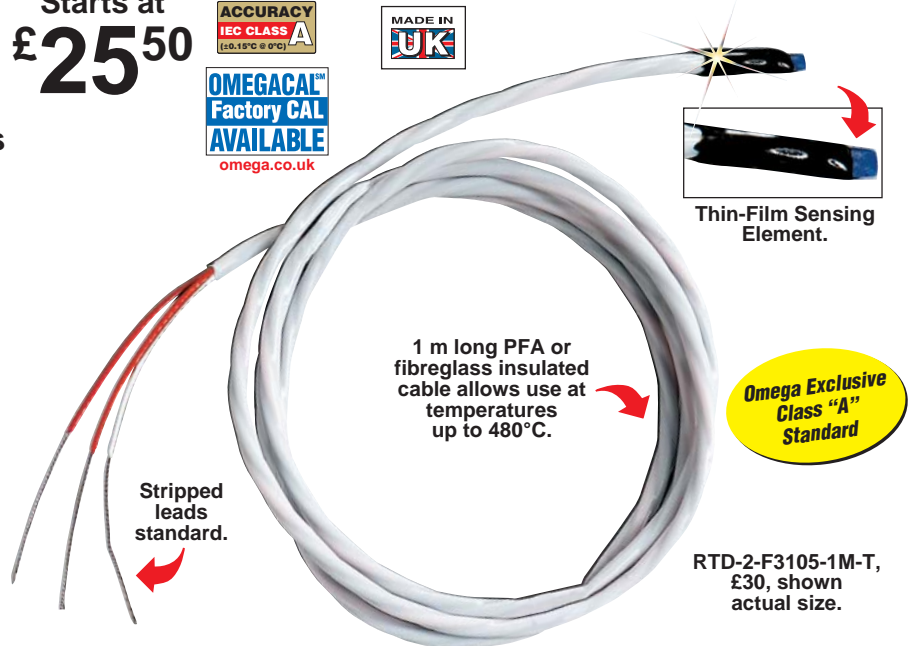
## **THERMOCOUPLES AND DATA ACQUISITION DEVICE**

# RTD Sensors—Fast Response Exposed RTD Element with Lead Wires

Starts at  
**£25<sup>50</sup>**



- ✓ Thermal Response (63%)  
Less Than 75 Milliseconds  
in Water Flowing at 1m/S
- ✓ High-Accuracy Class  
“A”, 100 Ω DIN Platinum  
Elements Standard
- ✓ Ultra Precise Accuracy  
1/3 and 1/10 DIN, and  
Economical Class “B”  
Also Available\*
- ✓ Operating Range Up  
to 480°C (900°F) Available
- ✓ 1 m Long 2-, 3-, or  
4-Wire 7/0.16 mm Cables  
for Connecting to Most  
Handheld Instruments



**MOST POPULAR MODELS HIGHLIGHTED!**

To Order (Specify Model Number)						Price		
Model Number	Element	Lead Wire	Potting Material	Maximum Temperature	Style 1 (2 wire)	Style 2 (3 wire)	Style 3 (4 wire)	
RTD-2-F3105-1M-T, shown actual size								
RTD-(*)-F3105-1M-T	F3105 (2 x 2 mm)	PFA	Epoxy	230°C	£25.50	£30.00	£33.00	
RTD-(*)-F3102-1M-T	F3102 (4 x 5 mm)	PFA	Epoxy	230°C	25.50	30.00	33.00	
RTD-2-F3102-1M-G provides larger measuring area (2x) than the F3105 (shown larger than actual size)								
RTD-(*)-F3105-1M-G	F3105 (2 x 2 mm)	Fibreglass	Ceramic	480°C	£25.50	£30.00	£33.00	
RTD-(*)-F3102-1M-G	F3102 (4 x 5 mm)	Fibreglass	Ceramic	480°C	25.50	30.00	33.00	
RTD-2-1PT100K2515-1M-T, shown larger than actual size								
RTD-(*)-1PT100K2515-1M-T	1PT100K2515	PFA	Epoxy	230°C	£25.50	£30.00	£33.00	
RTD-(*)-1PT100KN2528-1M-T	1PT100KN2528	PFA	Epoxy	230°C	25.50	30.00	33.00	

\*1/3B and 1/10B DIN accuracies only available with wire wound elements and 4-wire configurations.

**Note:** For longer leads, change “-1M” in model number to length desired and add £1.85/metre. Other RTD elements are also available with lead wires attached; consult Sales. Accuracies of 1/3 and 1/10 DIN are only available in 1PT100K2515 and 1PT100KN2528 wire-wound elements and require 4-wire construction. For 1/3 DIN, add £5.40; for 1/10 DIN, add £27. Terminations available: For “-LUG” add £3, for “-OTP” and “-MTP” 3-pin connectors add £4.70. For 4-pin mini DIN connector add “-MDIN4” to model number and £8. To order sensors with bare wires and connections for use to 600°C, replace “-T” or “-G” with “-B” in model number.

**Ordering Examples:** RTD-3-1PT100K2515-1M-T-1/3, 1PT100K2515 1/3 DIN accuracy element with 1 m of 4-conductor PFA insulated cable attached (epoxy potted), £33 + 5.40 = £38.40. RTD-3-F3102-2M-G, F3102 class “A” element with 2 m of 4-conductor fibreglass-insulated cable attached (ceramic potting), £33 + 1.85 = £34.85.



## Four Channel RTD Input Data Acquisition Module with USB or Ethernet Interface

PT-104A



PT-104A shown smaller than actual size.

- ✓ Measures Temperature (RTDs), Resistance and Voltage
- ✓ High Accuracy (0.01°C) and Resolution (0.001°C)
- ✓ Powered by USB Port or Power-Over-Ethernet (PoE)
- ✓ For Use with 2, 3 and 4-Wire Pt100 and Pt1000 RTD Sensors

The PT-104A is a four-channel, high-resolution temperature data acquisition module for use with PT100 and PT1000 RTD sensors. It can also be used to measure resistance (375  $\Omega$  and 10,000  $\Omega$  ranges) and voltage (115 mV or 2.5V ranges). In PT100/PT1000/resistance mode, the unit uses a four wire circuit. In voltage mode, the input connector can be treated as a differential input with ground, or two single-ended inputs. Both inputs must be 0V or above, though it does not matter which input has the higher voltage. For the 115 mV voltage range, the accuracy may vary by 2%, and the temperature coefficient will be 100 ppm/°C.

Although accurate temperature sensors are widely available, it has been difficult to take advantage of them due to errors caused by the measuring device. The PT-104A, however, is designed to be inherently accurate. Rather than relying on voltage references (which tend to be temperature sensitive) it uses reference resistors which are extremely stable (low temperature coefficient and drift). The exact value of each resistor is stored in an EEPROM to provide the ultimate in accuracy (yearly re-calibration is recommended). To achieve the 0.001°C resolution a highly-advanced ADC is used that can resolve to better than 1 part in 16 million.

### Temperature

The PT-104A measures temperature using platinum resistance temperature sensors (RTDs). Both common industry standards (PT100 and PT1000) are supported. The unit is compatible with 2, 3 and 4 wire sensors (4 wire PT100 sensors are recommended for accurate measurements).

### Resistance

When measuring resistance, the unit uses a four-wire circuit to give the greatest possible accuracy.

Two resistance ranges are available (0 to 375  $\Omega$  and 0 to 10,000  $\Omega$ ).

The unit is calibrated for 0 to 375  $\Omega$  so this range should be used for accurate measurements.

### Voltage

For voltage measurements, each input connector can be treated as a differential input with ground, or two single-ended inputs.

Both inputs must be zero volts or above, though it does not matter which input has the higher voltage. Two voltage ranges are available (0 to 115 mV and 0 to 2500 mV). For the most accurate measurements use the 0 to 2500 mV range.





## Remote Data Collection

The new USB/Ethernet interface allows the logger to be used in a variety of situations: USB-only, USB-powered with Ethernet data, and Ethernet data with Power-over-Ethernet (PoE). Using the Ethernet interface, the PT-104A can be located anywhere on a LAN or on the internet.

## Power over Ethernet (PoE)

The PT-104A can obtain its power from the Ethernet port as a Powered Device (PD) according to the PoE standard. To use this feature, you must connect the unit to Power Sourcing Equipment (PSE) such as a network switch, router or power injector that also supports the PoE standard. Any standard Ethernet cable up to 100 m (about 328') in length can be used.

## Software

The PT-104A is supplied with Windows Logging and Player Software. The software will automatically detect which sensor is connected and will display readings in the correct units. Also supplied is a software development kit (SDK). The SDK contains a range of software drivers and example code that you can use to write your own software or to use your PT-104A data logger with third party software. With the included Logging Software you can set the sampling interval from 1 second to several hours and set the maximum number of readings. You can also tell the PT-104A data acquisition module what do to when the temperature

readings have been taken—either: stop; repeat immediately (start again); scroll (oldest recordings disappear); or repeat after delay (where the delay is set by the user)

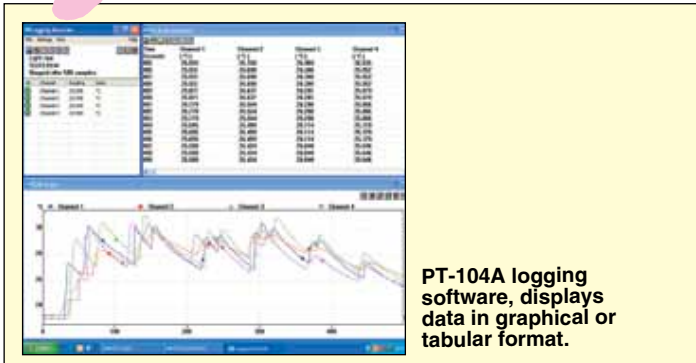
Multiple PT-104A modules can be used simultaneously with the logging software. Also, PT-104A modules can be mixed with TC-08 thermocouple input modules and used at the same time. Up to 20 units of any kind (PT-104A or TC-08) can be connected.

Using the PT-104A logging software, data can be viewed in a spreadsheet and/or in a graph as it is being recorded. Data collected from previous recordings can also be viewed using the Player.

## Specifications

PT-104A Platinum Resistance Data Logger			
Temperature	Resistance	Voltage	
Sensor	Pt100 <sup>1</sup> , Pt1000	N/A	N/A
Range	-200 to 800°C (-328 to 1472°F)	0 to 375 Ω <sup>1</sup> 0 to 10 kΩ	0 to 115 mV 0 to 2.5V <sup>1</sup>
Linearity	20 ppm	20 ppm	20 ppm
Accuracy @ 25°C	0.01°C <sup>1</sup>	20 ppm <sup>1</sup>	0.2% <sup>1</sup>
Temperature Coefficient	5 ppm/°C	5 ppm/°C	100 ppm/°C
RMS Noise (Using Filter)	0.01°C	10 ppm	10 ppm
Resolution	0.001°C	1 μΩ	0.156 μV
Conversion Time Per Channel		720 mS	
Number of Inputs		4	
Connectors		4-pin mini DIN	
Input Impedance		>>1 MΩ	
Overvoltage Protection		±30V	
Power	Powered by USB or Ethernet: USB 1.1: 5V ±10% @ <100 mA USB 2.0: 5V ±10% @ <200 mA Ethernet: 48V ±20% @ <40 mA (<2W)		
Environmental	20 to 30°C (68 to 86°F) for stated accuracy, 0 to 70°C (32 to 158°F) operating, 20 to 90% RH		
Software	Logging Software for 32-bit or 64-bit editions of Windows XP (SP2 or greater), Vista, 7. Software Development Kit containing drivers and example code for C, C++, Excel and LabView.		
Ethernet Port	Conforms to IEEE 802.3 10Base-T. Compatible with 10/100/1000Base-T networks. Conforms to IEEE 802.3af Power-over-Ethernet (PoE)		
USB Port	Conforms to USB 2.0 full-speed (12 Mbps)		
Computer Interface	USB or Ethernet		
Dimensions	36 H x 135 W x 184 mm D (1.42 x 5.31 x 7.24")		
Weight	500 g (1.1 lb)		

<sup>1</sup>Quoted accuracy is for options marked



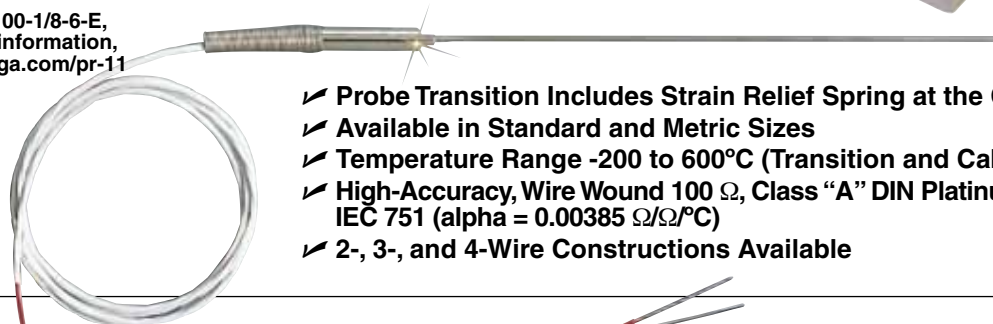
PT-104A logging software, displays data in graphical or tabular format.



PT-104A, shown smaller than actual size.

## Compatible RTD Probes

PR-11-2-100-1/8-6-E,  
for more information,  
visit [omega.com/pr-11](http://omega.com/pr-11)



- ✓ Probe Transition Includes Strain Relief Spring at the Cable Exit
- ✓ Available in Standard and Metric Sizes
- ✓ Temperature Range -200 to 600°C (Transition and Cable to 260°C Max)
- ✓ High-Accuracy, Wire Wound 100 Ω, Class "A" DIN Platinum Elements per IEC 751 (alpha = 0.00385 Ω/Ω°C)
- ✓ 2-, 3-, and 4-Wire Constructions Available

RTD-2-F3105-36-T,  
for more information,  
visit [omega.com/rtd-2-f3105](http://omega.com/rtd-2-f3105)



- ✓ Thermal Response (63%) Less Than 75 Milliseconds in Water Flowing at 3 Feet per Second
- ✓ High-Accuracy Class "A", 100 Ω DIN Platinum Elements Standard
- ✓ Ultra Precise Accuracy 1/2 and 1/10 DIN, and Economical Class "B" Also Available
- ✓ Operating Range Up to 480°C (900°F) Available
- ✓ 1 m (40") Long 2-, 3-, or 4-Wire #26 AWG Cables for Connecting to Most Handheld Instruments

SA1-RTD, for  
more information,  
visit [omega.com/sa1-rtd](http://omega.com/sa1-rtd)



- ✓ 100 Ω DIN Class A (±0.06 Ω or ±0.15°C at 0°C) Accuracy Standard
- ✓ Easy-Installation Silicone-Based, Self-Adhesive Backing Rated to 260°C (500°F)
- ✓ Sensor Can be Re-Applied
- ✓ 290°C (554°F) Short-Term Operation When Used as a "Cement-On" (OMEGABOND® Air Set Cements)
- ✓ Stripped 3-Wire or 4-Wire Leads Standard (Connectors Optional)
- ✓ Stocked in 1 m (40") Lengths; Also Available in 2 and 3 m (80 and 120") and Custom Length Lead Wires
- ✓ Other Resistances/Accuracies Available on Request

**To Order Visit [omega.com/pt-104a](http://omega.com/pt-104a) for Pricing and Details**

Model No.	Description
PT-104A	4-channel RTD input data acquisition module

Comes complete with USB cable, ethernet patch cable, 4 mating mini DIN screw terminal connectors, quick start guide, Windows software and complete operator's manual on CD.

Ordering Example: PT-104A, 4-channel RTD input data acquisition module.



# D

**CONNEX 3D PRINTER**



# Objet350 and Objet500 Connex3

## Multi-color, multi-material or high quality? Choose everything.

With the ability to 3D print the full range of Digital Materials including color, the Objet350 and Objet500 Connex3™ 3D Printers create parts with the precision, look and feel of real production parts using best-in-class versatility. Print parts with multiple properties, and choose from a wide range of material properties, from rubber to rigid, transparent to opaque, neutral to vibrant, and standard to bio-compatible. 3D print custom jigs, assembly fixtures and gauges and tooling with ultra-fine accuracy and smooth surfaces quickly and easily – no assembly required for parts with multiple materials. Connex3 delivers incredible efficiency with the power to serve diverse needs from one system. Objet Studio™ software makes it simple to build high-quality, accurate 3D models.



LEARN MORE ABOUT THE OBJET350 AND OBJET500 CONNEX3 AT [STRATASYS.COM](http://STRATASYS.COM)



# Objet350 and Objet500 Connex3

## Driven by powerful PolyJet™ technology

Proven PolyJet 3D Printing is famous for smooth surfaces, fine precision and diverse material properties. It works a bit like inkjet document printing, but instead of jetting drops of ink onto paper, the print head jets microscopic layers of liquid photopolymer onto a build tray and instantly cures them with UV light. The fine layers build up to create a prototype or production part.

Along with the selected model material, the 3D printer features two support material options: SUP705, removed with a WaterJet; and SUP706, which is easily removed and soluble for automated post-processing and increased geometric freedom to print complex and delicate features and small cavities.

With its astonishingly realistic aesthetics and ability to deliver special properties such as transparency, flexibility and even bio-compatibility, PolyJet 3D Printing offers a competitive edge in consumer products prototyping, precision tooling and specialized production parts.

## System Specifications

<b>Model Materials</b>	Rigid Opaque: VeroPureWhite™, VeroWhitePlus™, VeroBlackPlus™, VeroGray™, VeroBlue™, VeroCyan™, VeroMagenta™, VeroYellow™ Rubber-like: Agilus30™, TangoPlus™, TangoBlackPlus™, TangoBlack™, TangoGray™ Transparent: VeroClear™ and RGD720 Simulated Polypropylene: Rigur™ and Durus™ High Temperature Bio-compatible
<b>Digital Materials</b>	Digital ABS™ and Digital ABS2™ in ivory and green Hundreds of vibrant, repeatable colors in opaque and translucent Rubber-like blends in a range of Shore A values and color Simulated polypropylene materials with improved heat resistance
<b>Material Options</b>	Over 1,000
<b>Maximum Materials per Part</b>	82
<b>Support Material</b>	SUP705 (WaterJet removable) SUP706 (soluble)
<b>Maximum Build Size (XYZ)</b>	Objet350: 342 x 342 x 200 mm (13.4 x 13.4 x 7.9 in.) Objet500: 490 x 390 x 200 mm (19.3 x 15.4 x 7.9 in.)
<b>System Size and Weight</b>	1400 x 1260 x 1100 mm (55.1 x 49.6 x 43.4 in.); 430 kg (948 lbs.) <i>Material Cabinet:</i> 330 x 1170 x 640 mm (13 x 46.1 x 26.2 in.); 76 kg (168 lbs.)
<b>Resolution</b>	X-axis: 600 dpi; Y-axis: 600 dpi; Z-axis: 1600 dpi
<b>Accuracy</b>	20-85 microns for features below 50 mm; up to 200 microns for full model size
<b>Minimum Layer Thickness</b>	Horizontal build layers as fine as 16 microns (.0006 in.)
<b>Build Modes</b>	Digital Material: 30-micron (.001 in.) resolution High Quality: 16-micron (.0006 in.) resolution High Speed: 30-micron (.001 in.) resolution
<b>Software</b>	Objet Studio intuitive 3D printing software
<b>Workstation Compatibility</b>	Windows 7/ Windows 8
<b>Network Connectivity</b>	LAN - TCP/IP
<b>Operating Conditions</b>	Temperature 18-25°C (64-77°F); relative humidity 30-70% (non-condensing)
<b>Power Requirements</b>	110-240 VAC 50/60Hz; 1.5 kW single phase
<b>Regulatory Compliance</b>	CE, FCC

**stratasys**

STRATASYS.COM

ISO 9001:2008 Certified

©2016 Stratasys Ltd. All rights reserved. Stratasys, FDM, Stratasys logo, Objet, For a 3D World, Objet Studio, Eden, Eden260, Eden260V, Connex, Objet260 Connex3, Agilus30, TangoBlack, TangoGray, TangoPlus, TangoBlackPlus, VeroBlue, VeroBlack, VeroBlackPlus, VeroClear, VeroDent, VeroGray, VeroWhite, VeroPureWhite, VeroWhitePlus, VeroCyan, VeroMagenta, VeroYellow, Durus, Rigur, Digital Materials, Digital ABS and PolyJet are trademarks or registered trademarks of Stratasys Ltd. and/or its subsidiaries or affiliates and may be registered in certain jurisdictions. ULTEM is a registered trademark of SABIC or affiliates. Adobe and Photoshop are either registered trademarks or trademarks of Adobe Systems Incorporated in the United States and/or other countries. All other trademarks belong to their respective owners. PSS\_PJ\_Obj350Obj500Connex3\_A4\_1216a



info@seido-systems.com

BE +32 56 35 00 35 | NL +31 30 32 00 274

Showroom: Kortrijk & Eindhoven

### Rigid Opaque Materials

#### VeroGray RGD850, VeroBlackPlus RGD875, VeroWhitePlus RGD835

	ASTM	Units	Metric	Units	Imperial
Tensile strength	D-638-03	MPa	50-65	psi	7250-9450
Elongation at break	D-638-05	%	10-25	%	10-25
Modulus of elasticity	D-638-04	MPa	2000-3000	psi	290,000-435,000
Flexural Strength	D-790-03	MPa	75-110	psi	11000-16000
Flexural Modulus	D-790-04	MPa	2200-3200	psi	320,000-465,000
HDT, °C @ 0.45MPa	D-648-06	°C	45-50	°F	113-122
HDT, °C @ 1.82MPa	D-648-07	°C	45-50	°F	113-122
Izod Notched Impact	D-256-06	J/m	20-30	ft lb/inch	0.375-0.562
Water Absorption	D-570-98 24hr	%	1.1-1.5	%	1.1-1.5
Tg	DMA, E <sub>o</sub>	°C	52-54	°F	126-129
Shore Hardness [D]	Scale D	Scale D	83-86	Scale D	83-86
Rockwell Hardness	Scale M	Scale M	73-76	Scale M	73-76
Polymerized density	ASTM D792	g/cm3	1.17-1.18		
Ash content VeroGray, VeroWhitePlus	USP281	%	0.23-0.26	%	0.23-0.26
Ash content VeroBlackPlus	USP281	%	0.01-0.02	%	0.01-0.02

#### VeroBlue RGD840

	ASTM	Units	Metric	Units	Imperial
Tensile strength	D-638-03	MPa	50-60	psi	7250-8700
Elongation at break	D-638-05	%	15-25	%	15-25
Modulus of elasticity	D-638-04	MPa	2000-3000	psi	290,000-435,000
Flexural Strength	D-790-03	MPa	60-70	psi	8700-10200
Flexural Modulus	D-790-04	MPa	1900-2500	psi	265,000-365,000
HDT, °C @ 0.45MPa	D-648-06	°C	45-50	°F	113-122
HDT, °C @ 1.82MPa	D-648-07	°C	45-50	°F	113-122
Izod Notched Impact	D-256-06	J/m	20-30	ft lb/inch	0.375-0.562
Water Absorption	D-570-98 24hr	%	1.5-2.2	%	1.5-2.2
Tg	DMA, E <sub>o</sub>	°C	48-50	°F	118-122
Shore Hardness [D]	Scale D	Scale D	83-86	Scale D	83-86
Rockwell Hardness	Scale M	Scale M	73-76	Scale M	73-76
Polymerized density	ASTM D792	g/cm3	1.18-1.19		
Ash content	USP281	%	0.21-0.22	%	0.21-0.22

### Polypropylene-like Materials

#### DurusWhite RGD430

	ASTM	Units	Metric	Units	Imperial
Tensile strength	D-638-03	MPa	20-30	psi	2900-4350
Elongation at break	D-638-05	%	40-50	%	40-50
Modulus of elasticity	D-638-04	MPa	1000-1200	psi	145,000-175,000
Flexural Strength	D-790-03	MPa	30-40	psi	4350-5800
Flexural Modulus	D-790-04	MPa	1200-1600	psi	175,000-230,000
HDT, °C @ 0.45MPa	D-648-06	°C	37-42	°F	99-108
HDT, °C @ 1.82MPa	D-648-07	°C	32-34	°F	90-93
Izod Notched Impact	D-256-06	J/m	40-50	ft lb/inch	0.749-0.937
Water Absorption	D-570-98 24hr	%	1.5-1.9	%	1.5-1.9
Tg	DMA, E <sub>o</sub>	°C	35-37	°F	95-99
Shore Hardness [D]	Scale D	Scale D	74-78	Scale D	74-78
Rockwell Hardness	Scale M	Scale M	no data	Scale M	no data
Polymerized density	ASTM D792	g/cm3	1.15-1.17		
Ash content	USP281	%	0.10-0.12	%	0.10-0.12

### Rubber-like Materials

#### TangoBlackPlus FLX980 and TangoPlus FLX930

	ASTM	Units	Metric	Units	Imperial
Tensile strength	D-412	MPa	0.8-1.5	psi	115-220
Elongation at break	D-412	%	170-220	%	170-220
Compressive set	D-395	%	4-5	%	4-5
Shore Hardness [A]	D-2240	Scale A	26-28	Scale A	26-28
Tensile Tear resistance	D-624	Kg/cm	2-4	Lb/in	18-22
Polymerized density	ASTM D792	g/cm3	1.12-1.13		

#### TangoBlack FLX973

	ASTM	Units	Metric	Units	Imperial
Tensile strength	D-412	MPa	1.8-2.4	psi	115-350
Elongation at break	D-412	%	45-55	%	45-55
Compressive set	D-395	%	0.5-1.5	%	0.5-1.5
Shore Hardness [A]	D-2240	Scale A	60-62	Scale A	60-62
Tensile Tear resistance	D-624	Kg/cm	3-5	Lb/in	18-24
Polymerized density	ASTM D792	g/cm3	1.14-1.15		

#### TangoGray FLX950

	ASTM	Units	Metric	Units	Imperial
Tensile strength	D-412	MPa	3-5	psi	435-725
Elongation at break	D-412	%	45-55	%	45-55
Compressive set	D-395	%	0.5-1.5	%	0.5-1.5
Shore Hardness [A]	D-2240	Scale A	73-77	Scale A	73-77
Tensile Tear resistance	D-624	Kg/cm	8-12	Lb/in	50-60
Polymerized density	ASTM D792	g/cm3	1.16-1.17		



All data provided herein, which is related to consumables, was collected from specific specimens and tests conditions and is provided for information only. Characteristics may vary if different specimens and test conditions are applied. Unless expressly provided in writing, no warranties are made and warranties of merchantability or fitness for a particular purpose are expressly disclaimed.

[www.stratays.com](http://www.stratays.com) [info@stratays.com](mailto:info@stratays.com)

# E

## ERRORBARS IN HEAT TRANSFER EXPERIMENTS

### E.1. ERRORBARS IN THE NU-RA CALCULATIONS

#### E.1.1. DIFFERENT CONDUCTIVE MATERIALS

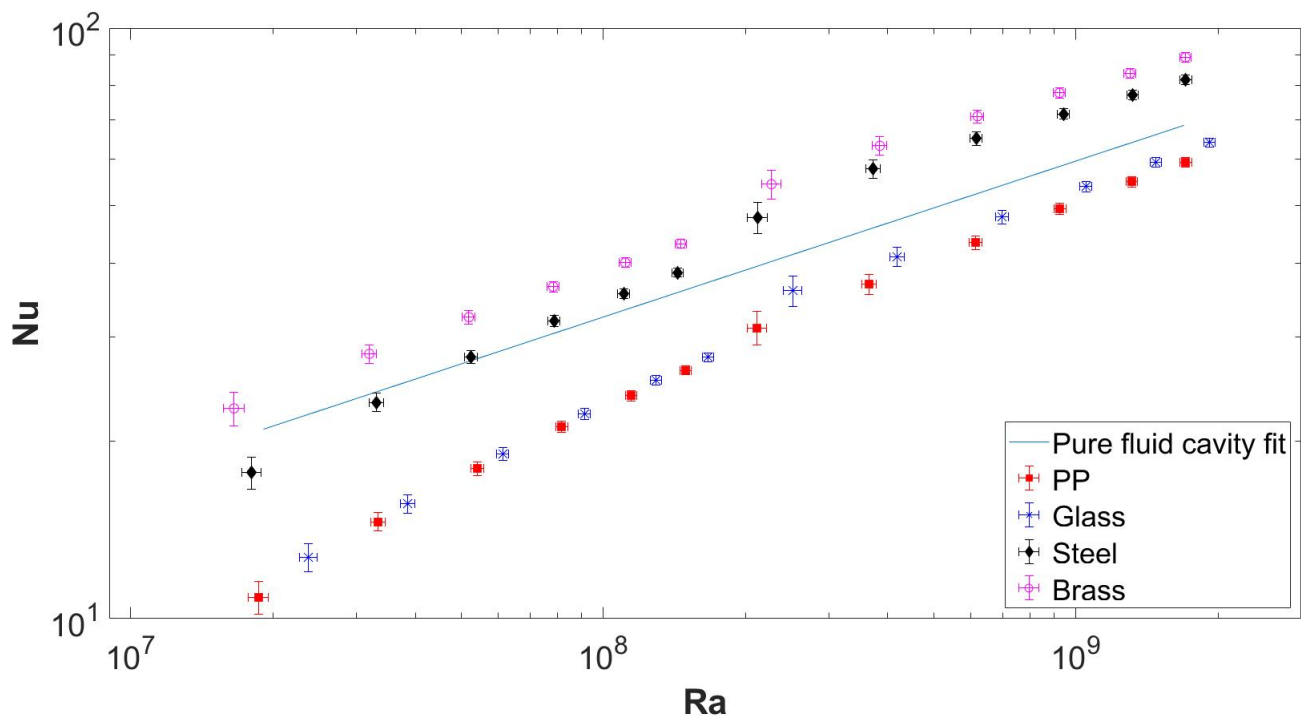


**Figure E.1:** Effect of different conductive materials on the heat transfer inside the side-heated cubicle enclosure. The sphere diameter is 15.3mm and a BCT configuration was used. In this figure both the horizontal and vertical error-bars are included.

### E.1.2. DIFFERENT PACKING CONFIGURATIONS

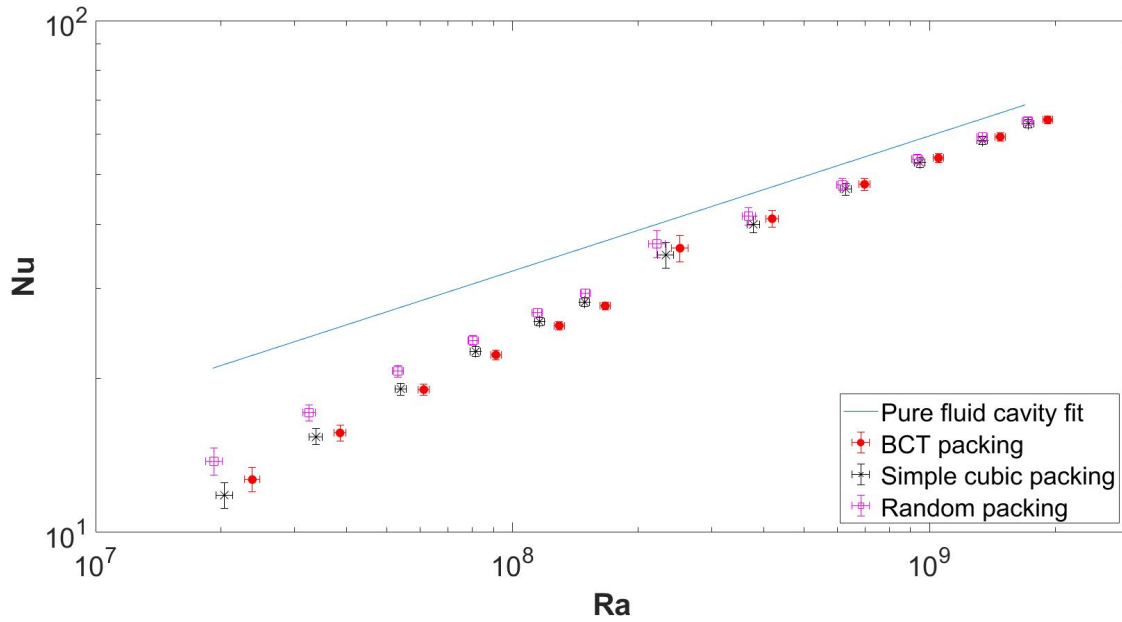


**Figure E.2:** Effect of different packing configurations on the heat transfer. Glass balls with a diameter of 15.3 mm were used for these experiments. In this figure both the horizontal and vertical error-bars are included.

### E.1.3. DIFFERENT SIZED SPHERES

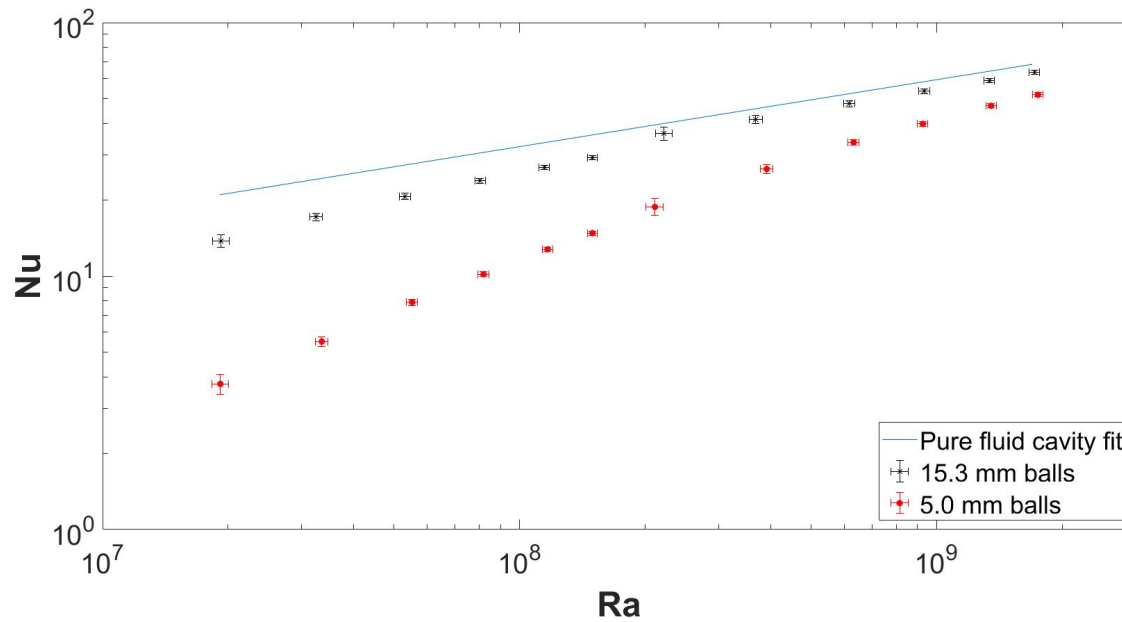


**Figure E.3:** Effect of different sized spheres on the heat transfer. The balls were stacked in a random configuration in these experiments. In this figure both the horizontal and vertical error-bars are included.

## E.1.4. 3D STRUCTURE

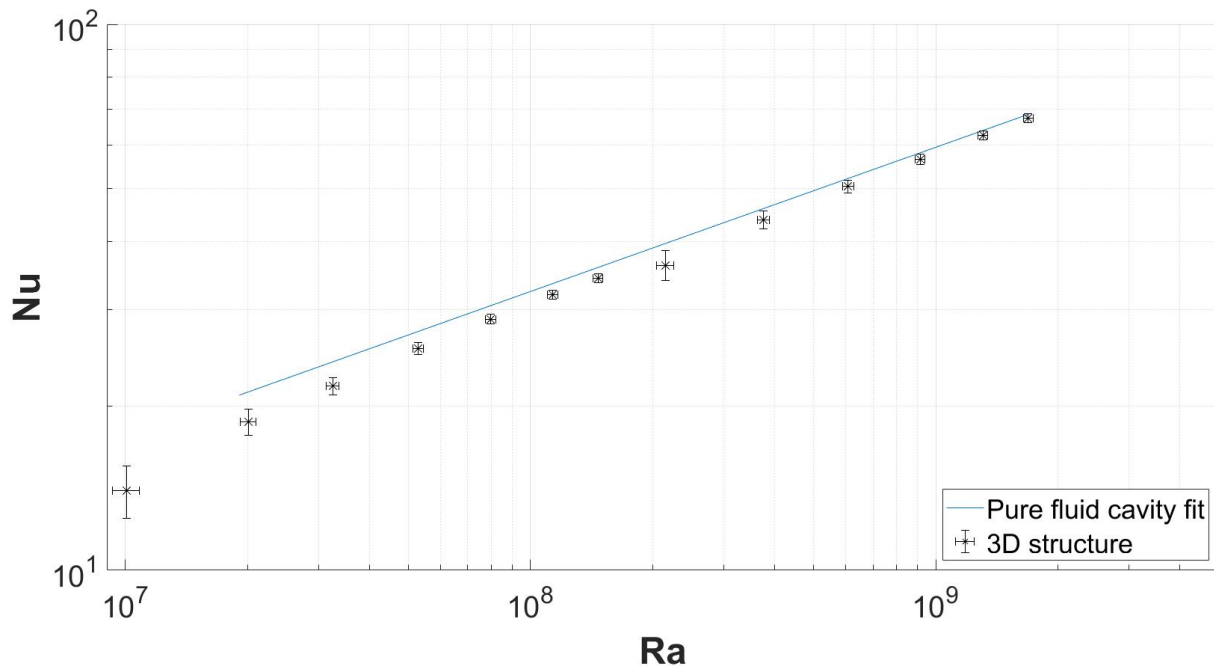


**Figure E.4:** Effect of the 3D-structure on the heat transfer. The 3D-structure was positioned in the middle of the cell, a distance  $\sigma \approx 7.9\text{mm}$  away from the left and right solid boundaries. In this figure both the horizontal and vertical error-bars are included.



# F

## VELOCITY PROFILES

### F.1. VERTICAL VELOCITY PROFILES

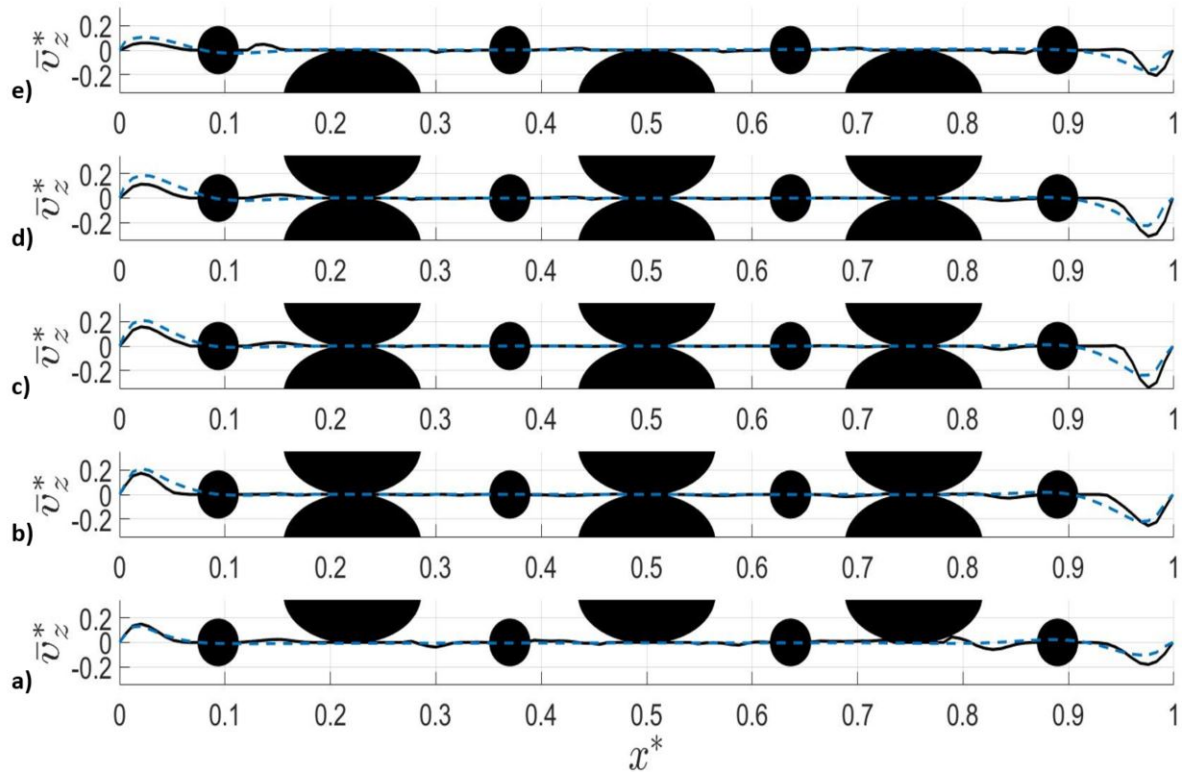


**Figure F.1:** Effect of coarse-grained porous media on the mean vertical velocity component  $\bar{v}_z^*$  profiles at different horizontal lines inside a cubic enclosure at  $Ra = 7.9 \times 10^6$ . The blue dashed lines represent the normalized velocity profiles in the pure fluid enclosure while the black lines represent the normalized velocity profiles in the BCT packed enclosure.

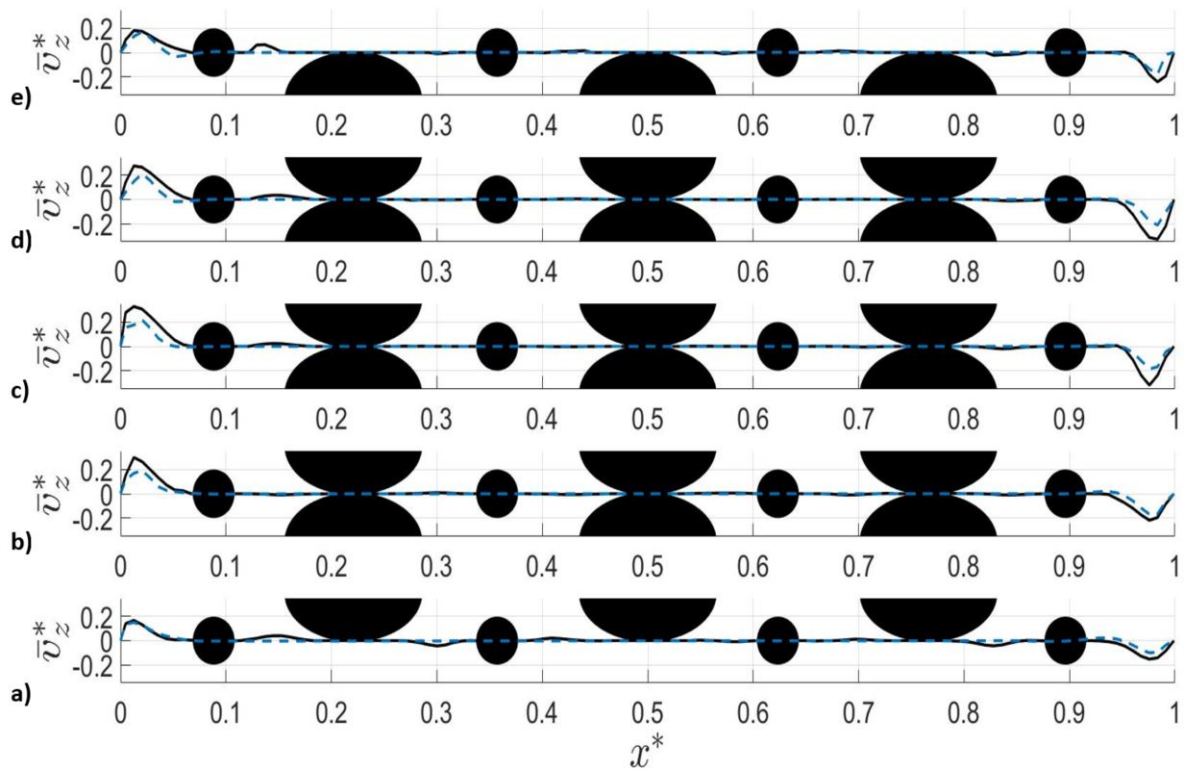


**Figure F2:** Effect of coarse-grained porous media on the mean vertical velocity component  $\bar{v}_z^*$  profiles at three different horizontal lines inside a cubic enclosure at  $Ra = 1.5 \times 10^8$ . The blue dashed lines represent the normalized velocity profiles in the pure fluid cubic enclosure while the black lines represent the normalized velocity profiles in the BCT packed enclosure.